

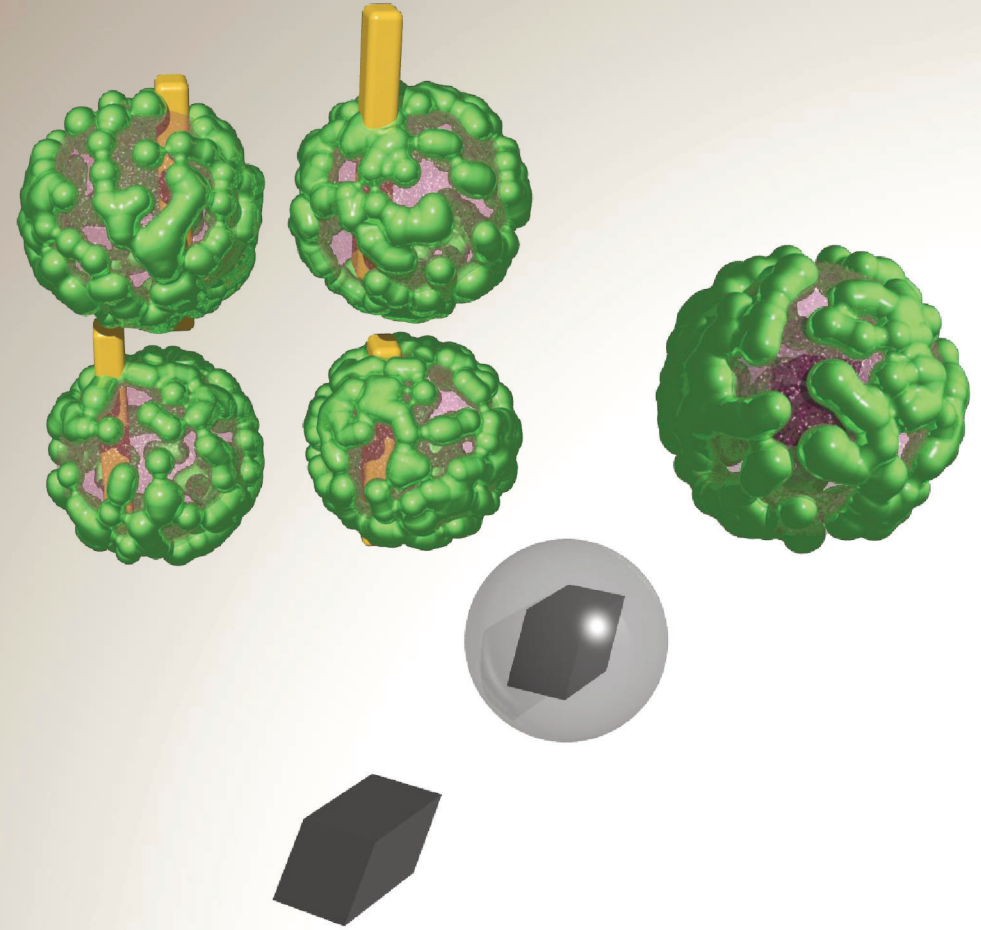
Stephan Hinrichs

Synthesis and characterization of anisotropic iron oxides  
and their incorporation into a thermoresponsive matrix

# Synthesis and characterization of anisotropic iron oxides and their incorporation into a thermoresponsive matrix

Dissertation

Stephan Hinrichs



Stephan Hinrichs

# Synthesis and characterization of anisotropic iron oxides and their incorporation into a thermoresponsive matrix

## Dissertation

In conformity with the requirements for the degree of  
Doctor rerum naturalium (Dr. rer. nat.)  
Submitted to the University of Hamburg

Faculty of Mathematics, Informatics, and Natural Sciences

Department of Chemistry

Submitted by  
Stephan Hinrichs

Hamburg, 2020



|                          |   |
|--------------------------|---|
| Supervisors:             | Dr. Birgit Hankiewicz<br>Prof. Dr. Volker Abetz |
| 1 <sup>st</sup> Referee: | Dr. Birgit Hankiewicz                           |
| 2 <sup>nd</sup> Referee: | JProf. Dr. Simone Mascotto                      |
| Date of Submission:      | 10.9.2020                                       |
| Date of Disputation:     | 11.12.2020                                      |
| Date of print:           | 15.12.2020                                      |



*This work was prepared under supervision of Dr. Birgit Hankiewicz at the Institute of Physical Chemistry (Department of Chemistry, Faculty of Mathematics, Informatics, and Natural Sciences) of the University of Hamburg. The dissertation began the 1<sup>st</sup> December 2016 and the work was submitted on 10<sup>th</sup> September 2020. The work was financed on a regular in-house contract from the 1<sup>st</sup> December 2016 until the 1<sup>st</sup> April 2017 when I changed onto a doctoral scholarship granted by the University of Hamburg that ran for one initial year before being prolonged until the 15<sup>th</sup> of November 2018, when the contract was changed to a regular in-house contract again.*



# Abstract

In this work I present the synthesis and characterization of anisotropic, multiresponsive hydrogels followed by an in-depth study of the interactions between magnetic iron oxide particles and their surrounding polymer-solvent matrix. The magnetic particles were synthesized with anisotropic shapes to make use of the magnetic form anisotropy and to study their orientation in a magnetic field. Subsequently, the magnetic particles act as cores for a thermoresponsive network made of crosslinked poly-*N*-isopropylacrylamide (PNIPAM). The network is either covalently bound to the particles by anchoring to a silica shell surrounding the particles, or by physical adsorption when the particles are mixed with the PNIPAM network. All gels and particles were prepared in an aqueous medium to increase their inherent biocompatibility.

The magnetic cores consist of iron oxides, namely magnetite and goethite. Magnetite has excellent magnetic properties but is challenging to prepare in an anisotropic shape in aqueous medium. To achieve anisotropy, the particles were mostly synthesized in a hydrothermal reactor in presence of different surfactants. We found the optimal synthesis conditions when we combined a precursor-based approach, using akaganeite as the precursor, with dopamine as a shape guiding agent. This yielded a phase-pure, polydisperse product containing cubic particles mixed with elongated particles. The elongated particles possess an aspect ratio of 1.5 with a long 16 nm and a short 11 nm axis. The magnetization of these particles was with 273 kA/m at 56% of the bulk magnetization and the particles showed superparamagnetic behavior at room temperature. This synthetic route offers a product with the desired magnetic properties while also being straightforward and easily reproducible.

To investigate the influence of strong anisotropy we used acicular goethite particles. These particles are antiferromagnetic but have the peculiar property of aligning parallel to weak magnetic fields and perpendicular to strong fields. Instead of the aging procedure described in most literature concerning goethite, we deployed a new and fast hydrothermal method to create goethite rods in three length categories. Short rods of about 210 nm, intermediate rods of about 270 nm and long rods that range from 300 nm up to 1  $\mu\text{m}$ . We furthermore show that the field strength required for the orientation switch is tunable by adjusting the surface-area of the particles and explain this by a micromagnetic model.



The particles were surrounded by a silica shell to extend their colloidal stability and to use silane chemistry to bind the particles covalently to the matrix. Using a two-phase approach, we synthesized a silica shell with a tunable shell thickness between 6 and 30 nm.

As the matrix material we chose PNIPAM because of its inherent lower critical solution temperature (LCST) around 32 °C, close to the human body temperature, and because of its chemical stability and straightforward synthesis. The synthesis was done in two different approaches, both using a free radical emulsion polymerization. One with a grafting-through approach to create a core shell system, which could be crosslinked into a macrogel. For a second approach, PNIPAM was synthesized together with glutaraldehyde (GA) to form a macrogel into which the particles were added during or after the synthesis and mixed by stirring.

We investigated the mechanical properties of the created multiresponsive composites, and how they are influenced by the presence of a magnetic field, by dynamic mechanical analysis (DMA) using a rheometer. Additionally, we investigated the ability of the particles to orientate in a magnetic field with or without a matrix. For this we varied the crosslinking density and tuned the microgel bead size between 212 nm and 442 nm. We found that elongated particles (size  $\sim 210$  nm  $\times$  30 nm) can be effectively stopped in their orientation by microgels with large beads. The thermoresponsive nature of the hydrogel leads to rapid shrinking to about 100 nm when the LCST of 32 °C is approached which also enables particle orientation which was blocked below the LCST. The shrinking is fully reversible, visible in a restored large hydrodynamic radius and in a refrozen particle orientation. We show that the particles can influence the matrix in a magnetic field by changing its rigidity and that the matrix can influence the particles by modulating their orientational behavior upon changes in temperature.

## Zusammenfassung

Im Rahmen dieser Arbeit wurden anisotrope multiresponsive Hydrogele hergestellt, um die Wechselwirkungen zwischen magnetischen Partikeln und der sie umgebenden Matrix zu untersuchen. Die magnetischen Partikel wurden in anisotropen Formen hergestellt, um sich so die magnetische Formanisotropie zunutze zu machen und die Orientierung der Partikel in einem Magnetfeld zu untersuchen. Die magnetischen Partikel sollen als Ankerpunkte eines thermoresponsiven Netzwerks fungieren. Das Netzwerk besteht hierbei aus quervernetztem Poly-*N*-isopropylacrylamid (PNIPAM) welches entweder kovalent über eine die Partikel umgebende Silikat-Schicht an den Partikeln verankert ist oder durch physikalische Adsorption an den Partikeln haftet. Die magnetischen Kerne wurden aus Eisenoxiden, genauer aus Magnetit und Goethit, hergestellt. Alle Reaktionen fanden im wässrigen Medium statt um die Biokompatibilität der Produkte zu erhöhen.

Magnetit wurde ausgewählt, da es exzellente magnetische Eigenschaften besitzt; die Herausforderung bestand in der anisotropen Formgebung im wässrigen Medium. Um anisotropes Wachstum zu realisieren, wurden die Partikel in einem hydrothermalen Reaktor hergestellt, wobei verschiedene oberflächenaktive Substanzen zugesetzt wurden. Im Laufe der Experimente fanden wir heraus, dass optimale Resultate erzielt werden, wenn ein Präkursor-basierter Ansatz gewählt wurde. Hierbei wurde Akaganeit als Ausgangsmaterial eingesetzt. Die Partikelform wurde durch Zugabe von Dopamin eingestellt. Unter diesen Bedingungen gelang es, ein phasenreines, polydisperses Produkt zu erhalten, dass sowohl kubische Partikel als auch leicht elongierte Partikel mit einem Aspekt-Verhältnis von 1.5 enthält, wobei die lange Achse der leicht anisotropen Partikel 16 nm und die kurze Achse 11 nm lang ist. Die gemessene Sättigungsmagnetisierung lag bei 273 kA/m was *ca.* 56% der Bulk-magnetisierung entspricht. Die Partikel zeigten in den Messungen bei Raumtemperatur superparamagnetisches Verhalten. Mit dieser Syntheseroute konnten wir ein Produkt mit den gewünschten Eigenschaften darstellen, wobei die Synthese gleichzeitig unkompliziert ist und gut reproduzierbare Ergebnisse liefert.

Um zusätzlich eine stark anisotrope Probe zu erhalten, wurden nadelförmige Goethit Partikel synthetisiert. Diese Partikel sind inhärent antiferromagnetisch, besitzen aber die interessante Eigenschaft ihre Orientierung je nach der Stärke eines angelegten Magnetfeldes zu verändern. Bei schwachen Feldern orientieren

sich die Partikel parallel zum Feld, bei starken Feldern orientieren sie sich orthogonal zum Feld. Anstelle der in der Literatur häufig verwendeten Alterungsmethode verwendeten wir auch hier einen hydrothermalen Ansatz, wodurch es uns gelang Goethit Stäbchen in drei Größenbereichen in kurzer Zeit herzustellen. Es wurden kurze Stäbchen mit einer Länge von ca. 210 nm, mittellange Stäbchen mit einer Länge von ca. 270 nm und schließlich lange Stäbchen mit einer Länge beginnend bei 300 nm bis hin zu 1  $\mu\text{m}$  hergestellt. Wir konnten weiterhin zeigen, dass die benötigte Feldstärke, um die Orientierung der Stäbchen zu ändern, abhängig von der Oberfläche der Partikel ist. Je mehr Oberfläche die Partikel besitzen, desto höhere Feldstärken werden benötigt, um die Orientierung zu ändern. Wir konnten diese Beobachtungen sehr gut mit einem mikromagnetischen Modell in Einklang bringen.

In einem weiteren Schritt nach der Partikelsynthese konnten die Partikel mit einer Silikat-Schicht umgeben werden, um ihre kolloidale Langzeitstabilität zu verbessern und um die gut zugängliche Silanchemie zu nutzen, um die Partikel kovalent an die Matrix zu binden. Indem wir uns einen Zwei-Phasen Ansatz zunutze machten, konnten wir eine Silikat Hülle mit einstellbarer Schichtdicke zwischen 6 und 30 nm synthetisieren.

Als Matrixmaterial wählten wir PNIPAM, denn es besitzt eine körpernahe untere kritische Lösungstemperatur (LCST) um die 32 °C. Zusätzlich ist PNIPAM und insbesondere seine LCST sehr stabil gegenüber seiner chemischen Umgebung und es lässt sich einfach synthetisieren. Die Synthese wurde mit zwei verschiedenen Verfahren durchgeführt, beide verlaufen nach einem frei radikalischen Emulsionspolymerisations-Mechanismus. Die erste benutzt einen *grafting-through* Ansatz der ein quervernetzbares Kern-Schale System erzeugt, während der zweite Ansatz PNIPAM direkt in Präsenz von Glutaraldehyd (GA) polymerisiert, um direkt ein Makrogel zu erzeugen, in das die Partikel anschließend eingebracht werden können.

Wir haben die mechanischen Eigenschaften dieser multiresponsiven Komposite und ihre Änderungen bei Anlegen eines Magnetfeldes mit Hilfe von rheologischen Messungen untersucht. Zusätzlich haben wir die Fähigkeit der Partikel untersucht, sich im magnetischen Feld innerhalb der Matrix zu orientieren. Dabei wurden sowohl Messungen mit umgebender Matrix als auch ohne durchgeführt. Um die Auswirkungen der Matrix zu testen, wurde die Quervernetzungsdichte und die Größe der Mikrogelkugeln variiert, wobei Größen zwischen 212 nm und 442 nm eingestellt wurden. Wir konnten beobachten, dass kurze Stäbchen (Größe  $\sim 210 \text{ nm} \times 30 \text{ nm}$ ) effektiv in ihrer Orientierung gestoppt werden konnten, wenn die Mikrogel-Kugeln groß gewählt wurden. Durch die thermoresponsiven

Eigenschaften des Hydrogels konnten wir es bei Temperaturerhöhung über 32 °C auf ca. 100 nm zusammenschrumpfen lassen, was dazu führte, dass die Partikel sich wieder orientieren konnten. Dieser Temperaturübergang ist vollständig umkehrbar, was wir sowohl durch den wiederhergestellten hydrodynamischen Radius als auch an einer wieder eingefrorenen Partikelorientierung nachweisen konnten. Wir zeigen hier, dass die Partikel bei Anlegen eines Magnetfeldes die Matrix beeinflussen können, indem sie die Steifigkeit der Matrix ändern und gleichzeitig andersherum die Matrix die Partikel beeinflusst, indem sie ihre Orientierungsfähigkeit moduliert, wenn sie auf einen Temperatur Stimulus reagiert.

## Index of Abbreviations

|        |   |
|--------|---|
| AA     | <u>A</u> llyl <u>a</u> mine   |
| AC     | <u>A</u> lternating <u>C</u> urrent                                   |
| BIS    | N,N-Methylene- <u>b</u> is-acrylamide                                 |
| CTAB   | <u>C</u> etyltri <u>m</u> ethylammonium <u>B</u> romide               |
| DLS    | <u>D</u> ynamic <u>L</u> ight <u>S</u> cattering                      |
| GA     | <u>G</u> lutaraldehyde  |
| HCP    | <u>H</u> exagonally <u>C</u> lose <u>P</u> acked                      |
| KPS    | Potassium <u>P</u> eroxydisulfate                                     |
| NIPAM  | <u>N</u> -Isopropylacryl <u>a</u> mide                                |
| PEG    | <u>P</u> olyethylene <u>G</u> lycole                                  |
| PNIPAM | <u>P</u> oly- <u>N</u> -Isopropylacryl <u>a</u> mide                  |
| PVP    | <u>P</u> olyvinylpyrrolidone  |
| SDS    | <u>S</u> odium <u>D</u> odecyl <u>S</u> ulfate                        |
| TEM    | <u>T</u> ransmission <u>E</u> lectron <u>M</u> icroscopy              |
| TEOS   | <u>T</u> etraethyl <u>O</u> rt <u>h</u> osilicate                     |
| TPM    | <u>T</u> ri-(methoxy Silyl)propyl <u>M</u> ethacrylate                |
| SAXS   | <u>S</u> mall <u>A</u> ngle <u>X</u> -Ray <u>S</u> cattering          |
| USAXS  | <u>U</u> ltra-small <u>A</u> ngle <u>X</u> -ray <u>S</u> cattering    |
| VSM    | <u>V</u> ibrating <u>S</u> ample <u>M</u> agnetometer                 |
| XRD    | <u>X</u> -Ray <u>D</u> iffraction                                     |
| XPCS   | <u>X</u> -ray <u>P</u> hoton <u>C</u> orrelation <u>S</u> pectroscopy |

## Publications

1. Hinrichs, S.; Nun, N.; Fischer, B.  
Synthesis and characterization of anisotropic magnetic hydrogels.  
*Journal of Magnetism and Magnetic Materials* **2017**, *431*, 237–240,  
doi:10.1016/j.jmmm.2016.10.016
2. Nun, N.; Hinrichs, S.; Schroer, M.A.; Sheyfer, D.; Grübel, G.; Fischer, B.  
Tuning the Size of Thermoresponsive Poly(N-Isopropyl Acrylamide)  
Grafted Silica Microgels.  
*Gels* **2017**, *3*, 34, doi:10.3390/gels3030034.
3. Witt, M.U.; Hinrichs, S.; Möller, N.; Backes, S.; Fischer, B.; von Klitzing, R.  
Distribution of CoFe<sub>2</sub>O<sub>4</sub> Nanoparticles Inside PNIPAM-Based Microgels of  
Different Cross-linker Distributions.  
*Journal of Physical Chemistry B* **2019**, *123*, 2405–2413,  
doi:10.1021/acs.jpcc.8b09236.
4. Lucht, N.; Hinrichs, S.; Großmann, L.; Pelz, C.; Felgenhauer, E.; Clasen, E.; Hankiewicz, B.  
Synthesis of magnetic ferrogels: A tool-box approach for finely tuned  
magnetic and temperature dependent properties  
Physical Science Reviews – submitted.
5. Hinrichs, S.; Großmann, L.; Clasen, E.; Grotjan, H.; Meyer, A.; Hankiewicz, B.  
High aspect ratio goethite nanorods: Investigation of size effects  
In submission

## Conference contributions

### **Oral contributions:**

International Conference on Magnetic Fluids ICMF 14, 2017

Hinrichs, S.; Lucht, N.; Nun, N.; Reinwardt, S.; Fischer, B.

Synthesis and characterization of anisotropic magnetic hydrogels

4.7. – 8.7.2017, Ekaterinburg

16<sup>th</sup> German Ferrofluid Workshop 2017,

Hinrichs, S.; Lucht, N.; Fischer, B.

Anisotropic magnetite particles and their incorporation into thermoresponsive hydrogels

17.7. – 19.7.2017, Dresden

Annual meeting of the SPP1681 in Benediktbeuern 2017,

Hinrichs, S.; Lucht, N.; Fischer, B.

Anisotropic magnetite particles and their incorporation into thermoresponsive hydrogels

27.9. – 29.9.2017, Benediktbeuern

Annual meeting of the SPP1681 in Benediktbeuern 2018,

Hinrichs, S.; Felgenhauer E.; Großmann L.; Meyer, A.; Hankiewicz, B.

Orientation of high aspect ratio goethite nanorods inside of thermoresponsive hydrogel in the presence of a magnetic field

26.9. – 28.9.2018 Benediktbeuern

**Poster contributions:**

Annual meeting of the SPP1681 in Benediktbeuern 2017,

Hinrichs, S.; Lucht, N.; Fischer, B.

Anisotropic magnetite particles and their incorporation into thermoresponsive hydrogels

27.9. – 29.9.2017, Benediktbeuern

12<sup>th</sup> International Conference on the scientific and clinical application of magnetic carriers, Magmeet 2018

Hinrichs, S.; Schwenk, M.; Hankiewicz, B.

Synthesis and characterization of anisotropic magnetic nanoparticles for incorporation into thermoresponsive hydrogels

22.5. – 26.5.2018, Copenhagen

Annual meeting of the SPP1681 in Benediktbeuern 2018,

Hinrichs, S.; Felgenhauer E.; Großmann L.; Meyer, A.; Hankiewicz, B.

Orientation of high aspect ratio goethite nanorods inside of thermoresponsive hydrogel in the presence of a magnetic field

26.9. – 28.9.2018, Benediktbeuern

15<sup>th</sup> International conference on Magnetic Fluids, 2019

Hinrichs, S.; Großmann, L.; Grotian, H.; Meyer, A.; Hankiewicz, B.

Synthesis and characterization of high aspect ratio iron oxide nanorods with switchable orientation in a magnetic field

8.7. – 12.7.2019, Paris

Annual meeting of the SPP1681 in Benediktbeuern 2019,

Hinrichs, S.; Großmann, L.; Grotian, H.; Meyer, A.; Hankiewicz, B.

Synthesis and characterization of high aspect ratio iron oxide nanorods with switchable orientation in a magnetic field

25.9. – 27.9.2019, Benediktbeuern

Apart from international conferences there were also countless subgroup meetings of the SPP1681, each entailing a poster or an oral contribution, which will not be mentioned here.



## Table of Contents

|       |  |    |
|-------|--|----|
| 1     | Introduction and task .....                                  | 1  |
| 2     | Theory .....   | 5  |
| 2.1   | Magnetic cores.....  | 6  |
| 2.1.1 | Iron oxides.....   | 6  |
| 2.1.2 | Magnetism.....   | 14 |
| 2.1.3 | Orientational phenomena .....                                | 28 |
| 2.2   | Multiresponsive materials.....                               | 30 |
| 2.2.1 | Thermoresponsiveness .....                                   | 30 |
| 2.2.2 | Magneto responsiveness.....                                  | 33 |
| 2.3   | Hydrogels.....   | 34 |
| 2.3.1 | From microgels to macrogels.....                             | 34 |
| 2.4   | The bridge connecting core and shell .....                   | 36 |
| 2.4.1 | Silica shell .....   | 36 |
| 2.5   | Synthesis.....   | 41 |
| 2.5.1 | Nanoparticle synthesis in general.....                       | 41 |
| 2.5.2 | Aqueous reactions in batch .....                             | 46 |
| 2.5.3 | Reaction with a precursor.....                               | 47 |
| 2.5.4 | PNIPAM-Gel synthesis .....                                   | 48 |
| 3     | Characterization methods.....                                | 50 |
| 3.1.1 | TEM .....  | 50 |
| 3.1.2 | XRD .....  | 52 |
| 3.1.3 | VSM .....  | 53 |
| 3.1.4 | DLS .....  | 54 |
| 3.1.5 | Rheology .....   | 56 |
| 3.1.6 | SAXS/XPCS.....   | 59 |
| 4     | Results and Discussion.....                                  | 64 |
| 4.1   | Magnetic cores: Magnetite, the ferrimagnetic powerhouse..... | 64 |
| 4.1.1 | Magnetite in batch reactions .....                           | 64 |
| 4.1.2 | Precursor based magnetite synthesis.....                     | 69 |
| 4.1.3 | Magnetite microwave treatment.....                           | 75 |
| 4.2   | Magnetic cores: Goethite, the anisotropic anti compass ..... | 77 |

|       |  |     |
|-------|--|-----|
| 4.2.1 | Goethite synthesis by aging .....  | 77  |
| 4.2.2 | Goethite synthesis by precursor based hydrothermal reactions.....              | 78  |
| 4.2.3 | Goethite orientation .....   | 81  |
| 4.3   | Silica shell: A stabilizing shell and the bridge to covalently bound gels..... | 88  |
| 4.3.1 | Stöber's adapted method.....   | 88  |
| 4.3.2 | Bi-phase method .....  | 90  |
| 4.4   | PNIPAM hydrogels, more than a simple matrix.....                               | 92  |
| 4.4.1 | Covalently bound magneto hydrogels .....                                       | 92  |
| 4.4.2 | Loosely connected macro-hydrogel.....  | 100 |
| 4.5   | Particle orientation and dynamics of particles trapped in a hydrogel .....     | 110 |
| 4.5.1 | Particle orientation within the gel network.....                               | 110 |
| 4.5.2 | Particle dynamics within the gel network.....                                  | 115 |
| 5     | Conclusion and Outlook .....   | 119 |
| 6     | Experimental section.....  | 123 |
| 6.1   | Akaganeite.....  | 123 |
| 6.2   | Hematite .....   | 125 |
| 6.3   | Goethite.....  | 126 |
| 6.3.1 | Aging reactions .....  | 126 |
| 6.3.2 | Precursor based hydrothermal reactions .....                                   | 126 |
| 6.4   | Magnetite.....   | 128 |
| 6.4.1 | Batch reactions.....   | 128 |
| 6.4.2 | Precursor based reactions.....   | 131 |
| 6.4.3 | Microwave assisted synthesis .....   | 133 |
| 6.5   | Gel synthesis .....  | 134 |
| 6.5.1 | Covalent.....  | 134 |
| 6.5.2 | Loosely connected gel .....  | 135 |
| 6.6   | Silica shell synthesis .....   | 137 |
| 6.6.1 | Stöber .....   | 137 |
| 6.6.2 | Bi-phase synthesis.....  | 137 |
| 7     | Safety and Disposal .....  | 138 |
| 8     | References.....  | 142 |
| 9     | Danksagung .....   | 155 |
|       | Declaration of Academic Integrity .....  | 160 |



# 1 Introduction and task

The goal of this work was to create an anisotropic multiresponsive hydrogel. This phrase is already an amalgamation of three buzzwords, all quite popular in current research. The term “hydrogel” alone was present in more than 375.000 articles in the past 10 years with about 8 million citations while the number is growing steadily with each passing year.[1] The term “multiresponsive” was used even more (775k publications with 15 million citations) and “anisotropic” takes the cake with 1.4 million publications (30 million citations) which is of course not surprising given the wide applicability of the terms “multi responsive” and “anisotropic”. The matter gets interesting when all these buzzwords are combined, and the number of articles decreases to only 11.000 (236k citations); quite a low number given the still broad applicability of the term.

The question emerges as to what exactly defines a multiresponsive hydrogel and which part of it is anisotropic? A hydrogel is defined as a polymeric network, which is highly swollen with water while it does not dissolve in water. The polymer network itself is in most cases responsible for the stimuli responsive properties.[2–4] There are polymers responsive to many kinds of stimuli like temperature,[5,6] pH,[7,8] or CO<sub>2</sub>[4]. In this work we aimed at using the innate temperature-responsiveness of a polymer matrix as well as introducing magnetic properties into the hydrogel matrix.

One goal for the creation of the composite was the creation of anisotropic magnetic nanoparticles under aqueous conditions. The magnetic material of choice was the group of iron oxides, because of their advantageous magnetic properties and biocompatibility.[9–12] The magnetic properties of iron oxides and generally all magnetic materials are connected to the particle shape by the magnetic form anisotropy.[13] It was observed that for example the coercivity field strength is increased for an acicular particle shape compared to spherical particles.[14] However, this was shown on a composite of magnetite and maghemite, so the results needed to be replicated for pure phase materials. The easiest way to get anisotropic iron oxide particles is to focus on those iron oxides that grow naturally into anisotropic shapes like akaganeite or goethite. Especially akaganeite has proven to work very well as a precursor to synthesize all kinds of iron oxides with very good control over the phase of the product and thus its magnetic properties.[15,16]

The problem is that these materials are not ferri- or ferromagnetic, they possess no strong magnetic moment. However, this does not mean to imply that the magnetic properties of these materials are not interesting, on the contrary, there have been detailed studies about the peculiar properties of goethite.[17–20] The synthesis and characterization of goethite nanorods was studied in detail in this work and their interplay with the hydrogel matrix was investigated by X-ray photon correlation spectroscopy (XPCS) measurements. We could confirm the observation that goethite switches its orientation from parallel to an applied field to perpendicular to the field when the field strength is increased. We further showed that the field strength threshold for reorientation is dependent on the size of the particles. This behavior is explained by utilizing a micromagnetic theory.[18]

Since magnetite shows the highest net magnetic moment among the iron oxides, creating anisotropic magnetite particles was one of the main goals in this work. Since magnetite grows in the inverse spinel crystal configuration it has a cubic symmetry and grows (thermodynamically driven) into an isotropic shape. There have been many approaches to block crystal faces with surfactants to suppress their growth and thus direct the growth into desired directions, leading to anisotropic shapes. There is for example the approach of using long polyethylene glycol (PEG) chains that stick to certain faces and leave others open to form magnetite nanowires.[21–26] Others used smaller molecules like the amphiphilic cetyltrimethylammonium bromide (CTAB)[27] or dopamine which binds very well with its catechol group.[28,29] Another approach is the synthesis of the particles directly in a magnetic field, which uses the controlled aggregation of small seed particles to create anisotropic particles.[24,30–37] Most of these experimental approaches were tested in this work, with mixed results. One major obstacle in the synthesis of nanoparticles in general is that the product is rarely uniform and relies very strongly on the synthesis conditions and the handling afterwards.[38] We found that a lot of the results published in literature were hard to reproduce, which seems to be an ongoing topic in chemistry in general.[39] However, in the end we found a method to produce phase pure, weakly anisotropic particles with good magnetic properties in a reproducible fashion.

The next step was combining the magnetic cores with a hydrogel, to create a multi-responsive composite. As the material for the hydrogel we chose PNIPAM. This material was and is treated as the “gold-standard” for thermoresponsive polymers, because of its temperature response around 32 °C, close to the human body temperature, and because this response is relatively independent of the chemical environment.[5] At 32 °C, pure PNIPAM changes from hydrophilic

properties and good solubility to hydrophobic properties and precipitation out of an aqueous solvent. This behavior is called a phase transition and the minimum temperature of this specific transition is the lower critical solution temperature (LCST). The polymer was synthesized as microgel particles by free radical emulsion polymerization. The stability against precipitation above the LCST was guaranteed by leftover sulfate groups from the peroxodisulfate initiator. To form a crosslinked network, it was copolymerized with *N,N*-methylene-bis-acrylamide (BIS) or GA. We chose two different synthetic strategies to incorporate the nanoparticles. The first was to bind the particles directly to the hydrogel by covalent interactions.[40,41] The second approach was to bind the particles mostly by physical adsorption and to incorporate them by simply mixing the particles with the hydrogel.[42]

For the covalently bound approach we needed a bridge between the nanoparticles and the matrix. This was realized by coating the nanoparticles with a silica shell, which has several advantages. The particles have prolonged stability in different media, are protected from oxidation,[43,44] and the silane surface is easy to functionalize. The silica coating reaction step followed either the Stöber protocol in ethanol,[45] or an approach in water,[44] both yielding similar results. The silica shell would also function as a chemically inert coating for biomedical applications, should the nanoparticles be used without the hydrogel matrix.[46]

After the particles are stabilized by silica, the shell is functionalized with 3-(methoxy silyl) propyl methacrylate (TPM) so the radical polymerization can incorporate the acrylate group into the backbone of the polymer. This way the shell is tightly connected to the hydrogel. After most of the polymerization is finished, allylamine (AA) is added to provide an amine function on the surface of the emerging microgel. This can be used to transform the microgel into a macrogel through the addition of GA, which links two amine functions, and hence also different microgel particles, by a peptide bond.

In the second approach the macrogel is directly formed by the copolymerization of *N*-isopropylacrylamide (NIPAM) with GA. In a free radical emulsion polymerization at 70 °C the network is formed, and the magnetic properties can be added by mixing in magnetic particles.

These two systems both have their advantages and disadvantages. The covalently bound gel enables direct particle-matrix interactions, but the process yields low particle loads in the final product. The loosely connected system allows for a high particle load, but if the particles are not perfectly stable, they will precipitate. If the particles are on the other hand perfectly stable, it is unclear whether there will be strong interactions between particle and matrix.

The main interaction between particles and matrix studied in this work was the orientation of particles in a magnetic field. We studied the orientation of goethite with and without a matrix in an ultra-small angle x-ray scattering (USAXS) setup at a synchrotron as well as at an inhouse SAXS setup. To gain insights into the restraints the matrix puts on particle orientation, the particle dimensions as well as the matrix parameters were changed.

## 2 Theory

This chapter deals with the theoretical basis for the research done over the course of this work. The rough outline will follow the course of the synthesis of the magnetic hydrogel. The base of the hydrogel is the magnetic particle, the magnetic properties of the hydrogel are ultimately derived from the properties of every single particle in the hydrogel network. Thus, a big part of the research time was spent creating adequate model systems for magnetic, anisotropic particles. The particles had to have sufficient magnetic properties to be measured even at low concentrations in the diluted gel state. The focus was thus on magnetite, for its high magnetization and later goethite, because of its interesting orientational behavior.[18,19] Following the magnetic part of the system, the theory behind the thermoresponsiveness of the two PNIPAM systems and the details of the hydrogel material class will be explained. A short chapter is dedicated to the bridge between hydrogel and magnetic cores, the silica shell. The last part of the theory will explain the synthesis conditions and why they were chosen in order to achieve the chosen parameters.



## 2.1 Magnetic cores

The magnetic particles are the anchor points for the polymer network as well as the single source of magnetic properties for the composite. This chapter will detail the materials of choice: iron oxides, as well as their magnetic properties and their origins. Later, the general theory of magnetism will be explained as well as its application in the nanometer regime. This will be expanded with a little glimpse into micromagnetic theory to explain some orientational phenomena observed during this work.

### 2.1.1 Iron oxides

Iron oxides appear in many forms, to date there are 16 known forms of iron oxides and oxyhydroxides.[47] They play important roles in a lot of disciplines be it environmental or industrial chemistry. They can be used because of their own particular properties, as starting materials for other processes or even as catalysts for other reactions.[48] The following short introductions will try to cover the basics for each iron oxide that was used in this work.

### 2.1.1.1 Akaganeite

Akaganeite was the universal precursor in our synthesis protocols, mainly because it allows an easy and controlled transition to other magnetic iron oxides like magnetite and goethite. It is an iron-oxide hydroxide ( $\beta\text{-FeO}(\text{OH}, \text{Cl})$ ) so iron is present in its  $\text{Fe}^{3+}$  oxidation state. The hydroxide and chloride ions in the formula are interchangeable. The crystal structure grows in the monoclinic space group  $I2/m$ , it forms a tunnel structure with the hydroxide or chloride anions in the center.[49] The iron atoms are found in two nonequivalent octahedral sites in the monoclinic structure. The anions in the akaganeite structure are arranged in a body centered cubic structure, reducing the density of akaganeite when compared to other iron oxide hydroxides.[50,51]

In nature the crystals are formed when an excess of chloride is found in the environment. When too many hydroxide ions are in solution with akaganeite they swap out the chloride in the tunnel structure and the transformation to other iron oxides becomes unreliable.[50] Akaganeite forms small cigar shaped crystals, it is a naturally anisotropic material, so it is interesting for our purposes if the shape

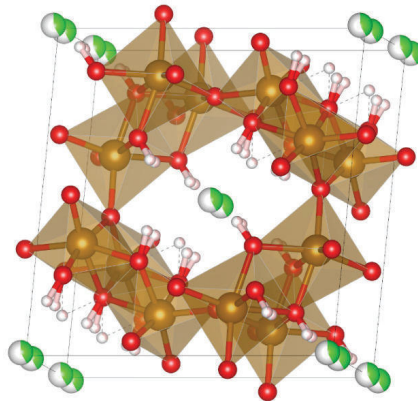


Figure 1: The akaganeite crystal structure, with chloride ions in the tunnel (green/white), oxygen at the octahedra corners (red), hydrogen at the hydroxide groups (white) and iron in the octahedra centers (gold).[51]

can be preserved across the transformation reaction.

Due to its tunnel structure akaganeite has applications as an ion exchanger, as a catalyst and as an adsorbent.[52–55] In chemistry, its main role now is that of a gateway precursor to the other iron oxides. It can be readily transformed to

magnetite in the presence of hydrazine[15,28] or other reducing agents.[9,56] Even the metastable phase of  $\alpha\text{-Fe}_2\text{O}_3$  was recently accomplished by first coating the precursors with a silica shell followed by heat treatment.[57]

#### 2.1.1.2 Hematite

Hematite ( $\alpha\text{-Fe}_2\text{O}_3$ ) is the main iron structure mined as iron ore, the main feedstock of iron for the steel industry. This is because it is the most stable and abundant oxidation product of iron.[50] It crystalizes in the corundum structure, there are hexagonally close packed (hcp) layers of oxygen atoms stacked along the [001] direction. In each hexagonal ring of oxygen atoms there is an iron atom at the center, meaning for every two atoms of oxygen in the plane there is one iron atom. The material is made up of pairs of  $\text{Fe}(\text{O})_6$ -octahedra. The octahedra share edges and faces and the face shared octahedra form a  $\text{Fe-O}_3\text{-Fe}$  triplet structure, which is responsible for some magnetic properties of hematite (Figure 2).

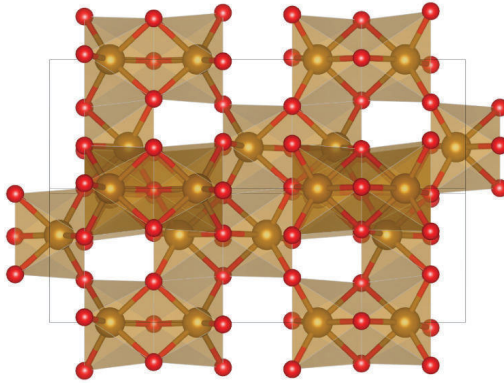


Figure 2: Hematite crystal structure, with oxygen atoms depicted in red and iron atoms depicted in gold. The triplet structure is nicely visible in the top-left of the structure.[58]

At room temperature hematite is weakly ferromagnetic, but it undergoes a reversible transition to an antiferromagnetic state below 260 K.[50] According to Coey, there are differences between the interactions of octahedra that share a corner and the interactions of octahedra that share an edge or a face.[59] This

difference leads to a canting of the antiferromagnetic sublattices of  $0.1^\circ$ , which gives rise to the weak ferromagnetic moment at room temperature. This ferromagnetic moment of less than  $10^4$  Bohr-magnetons is not strong enough to cause particles to agglomerate due to interparticle interactions.[60] This is without an applied magnetic field; when the field is applied, the negative anisotropy of the magnetic susceptibility makes the particles act in an antiferromagnetic fashion. As a consequence, the particles will orient perpendicular to the field director, already at field strengths in the low mT range.[60]

Apart from the interesting magnetic properties, hematite is also very versatile in terms of morphologies that are synthetically accessible. For nanoparticles there are different reports about hematite nano cubes ,[61–63] nano rods,[62,64] nano spindles [42,60,65] amidst more complicated shapes .[62,66] Given how easy it is to obtain and how versatile it is in terms of morphology and magnetic properties, hematite makes for a very interesting candidate for a model system.

#### 2.1.1.3 Goethite

While hematite is the most common iron oxide, goethite ( $\alpha$ -FeOOH) is certainly the most common iron oxyhydroxide. The goethite crystal structure is made up of double chains of Fe(III)O<sub>4</sub>OH<sub>2</sub> octahedra that share edges.[59] These double chains run parallel to the [100] direction and are linked by corner sharing to the neighboring chain (Figure 3).

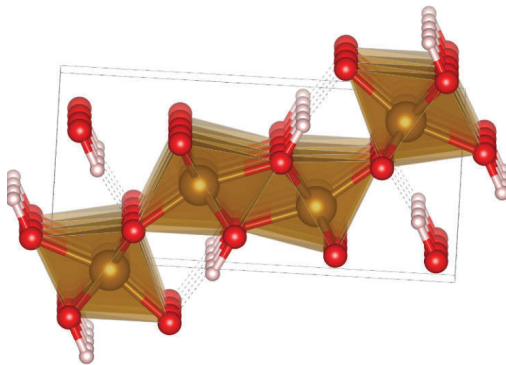


Figure 3: Goethite crystal structure. For better understanding of the crystal growth, four unit-cells were plotted in the  $b$  crystal direction. In the image, iron atoms are golden, oxygen is depicted in red and hydrogen in white.[67]

Goethite crystals grow into acicular shapes, which means they form long thin needles. These needles can range in length from tens of nanometers to microns and their distribution is often quite polydisperse.[50]

The magnetic properties of goethite are based on the double chains growing along the a-axis, one of the short axes of the particles. Both octahedra develop their own magnetic moment, which is oriented along the b-axis, the long axis of the particles, which runs antiparallel along both parts of the double chain, so the overall magnetic moments are balanced, the net magnetization is zero. This results in antiferromagnetic behavior.

On top of this antiferromagnetic behavior in bulk, Lemaire and coworkers discovered in 2002 that suspensions of goethite form a lyotropic nematic phase that aligns in a magnetic field.[68] It aligns in a way that it orients parallel to a magnetic field at low field strengths and switches its orientation perpendicular to the field when subjected to larger field strengths. They determined the switching field strength to be at 350 mT for their sample. The nematic phase formed a single domain already at very low field strengths of about 20 mT that is oriented parallel to the magnetic field. When the field is increased to about 250 mT they observed reorientational instabilities, some particles oriented perpendicular to the field. At 350 mT there is only one orientation that runs perpendicular to the magnetic field and this orientation increases with the field.

Lemaire *et al.* attributed this behavior to the intrinsic properties of nanomaterials that quite often differ from their bulk counterparts. Coey *et al.* observed a spin flop transition of 20 T in nanometric goethite particles, an unusual high value.[69] They determined that this high value is caused by a small ferromagnetic moment of  $0.004 \mu_B$  along the b-axis in their nanoparticles. This was attributed to a “statistical imbalance in the number of up- and down-chains present in the small cross section of the crystalline domains”,[69] in other words to uncompensated surface spins. These surface spins are now used to explain the orientational transition from parallel to perpendicular orientation. This behavior will be described in the section about magnetic ordering phenomena (section 2.1.3) when the general magnetic formulas are introduced.

#### 2.1.1.4 Magnetite

Magnetite ( $\text{Fe}_3\text{O}_4$ ) is a ferrimagnetic crystal and contains Fe(II) and Fe(III) in a 1:2 ratio. Magnetite is responsible for the magnetism of some rocks and ores and was likely the first natural magnet noticed by humankind.[50] It has found widespread use and is even synthesized by some natural organisms to serve as a navigational aid in earth's geomagnetic field.[70] Magnetite was one of the first minerals being characterized by x-ray diffraction by William Lawrence Bragg in 1915.[71] The crystals grow into the inverse spinel formation. The unit cell is a face centered cubic cell with 32  $\text{O}^{2-}$  Ions that are cubically close packed along the  $[111]$  direction. The iron atoms are divided between octahedral sites and tetrahedral sites. The octahedral sites are shared between the Fe(III) and Fe(II) atoms while the tetrahedral sites are entirely occupied by Fe(III) atoms (Figure 4). Magnetite is often non-stoichiometric, which means that some Fe(III) occupied sites are either empty or replaced by other divalent ions; this has distinct influence on the magnetic properties.

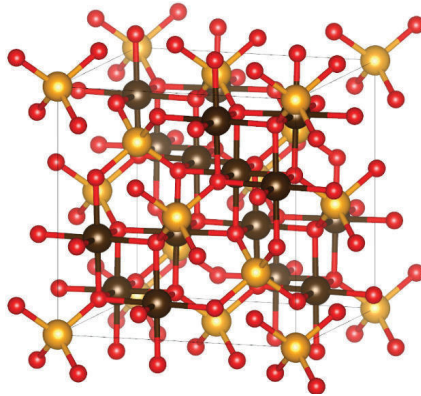


Figure 4: The crystal structure of magnetite. Iron species in tetrahedral sites are depicted in gold, octahedral sites are depicted in dark brown. Oxygen is depicted in red. The octahedral sites are shared between Fe(II) and Fe(III) ions.

As formerly mentioned, magnetite is naturally ferrimagnetic at room temperature, the magnetic properties are based on the two different cation sites (octahedral (B) and tetrahedral (A)) that are occupied by ions of varying valency. The spins

in the different sites are antiparallel due to the super exchange between the sites and the angle of their  $\text{Fe}_\text{A}\text{-O-Fe}_\text{B}$  linkage of  $126^\circ$ . Also, the magnitude of these spins is not equal, due to the different valence of the ions and their number, which gives rise to a net magnetic moment, resulting in ferrimagnetism. The easy axis, is along the [111] cube diagonals.[50] The critical radius below which magnetite particles become superparamagnetic lies around  $290 - 360 \text{ \AA}$  in diameter.[72] When the particle size and the size distribution are the same for different samples, different morphologies of magnetite show different magnetic properties. Namely the coercive field strength shows substantial differences that are in the order of spheres < cubes < octahedra, caused by the increased number of magnetic axes along this series of shapes.[73] This is an example for the influence of form anisotropy on the magnetic properties, which we were also trying to influence in this work.

### 2.1.1.5 Maghemite

Maghemite ( $\gamma\text{-Fe}_2\text{O}_3$ ) is isostructural to magnetite, but with more cation deficient sites. Almost the entire amount of Fe(II) species is in the higher oxidation state Fe(III) compared to magnetite, which reduces the magnetic moment of maghemite. Some of the oxidized Fe(II) species leave behind vacancies in the octahedral sites, which can in turn warp the crystal lattice of maghemite (Figure 5).[47] Maghemite often occurs as a side product in the synthesis of magnetite and since its crystal structure is so similar, it is virtually impossible to differentiate the two by x-ray diffraction (XRD) exclusively. Usually the magnetic properties, especially the hyper fine field splitting that is measured by Mössbauer spectroscopy, are used to distinguish the two phases.[74] In almost all syntheses of magnetite, traces of maghemite are present as impurities.

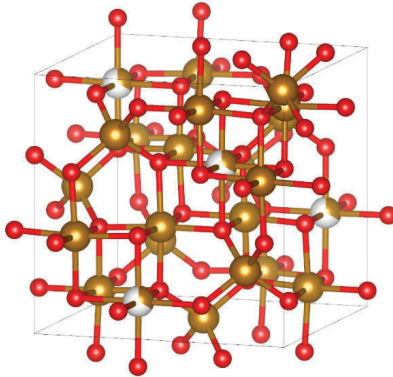


Figure 5: Crystal structure of maghemite. The iron species Fe(III) is depicted in gold, oxygen in red. Four cations are depicted as partly filled spheres, these show potentially vacant Fe sites.

The magnetic properties of maghemite are, like magnetite, based on two Fe-sublattices caused by the difference in the tetrahedral and octahedral sites. The ferrimagnetic effect of maghemite is smaller than the one for magnetite because there is no difference in valency of the ions at the different lattice sites.



### 2.1.2 Magnetism

To understand why the different iron oxides behave differently when subjected to a magnetic field and to understand which effect gives them their unique magnetic properties, we need to dive deeper into the subject of magnetism. The following chapter will give a short introduction into the formalism behind magnetism, into the different kinds of magnetism that were already touched briefly in the iron oxide chapter and lastly introduce a micromagnetic model to describe the changes that occur when we move the particle size into the nano-realm. In the following I will use **bold** letters to denote vectors.

Following Maxwell's laws, a moving electric charge produces a magnetic field. This magnetic field has a field strength  $\mathbf{H}$  with the unit A/m. The field is made of force lines that move magnetic objects along their path, the field lines. This magnetic field interacts with other objects and in turn induces a magnetization  $\mathbf{M}$ . The magnetization is used either in magnetization per mass or per volume, because the definition of the magnetization is "*the inner magnetization field  $\mathbf{M}$  equals the field  $\mathbf{B}/\mu_0$  generated by the bound charges and currents inside*".[75] In other words the magnetization is the sum of all magnetic moments  $\boldsymbol{\mu}$  in a given volume. The unit of the magnetization is A/m per volume or Am<sup>2</sup>/kg for mass magnetization, respectively. The field  $\mathbf{B}$  in the definition of the magnetization is the magnetic flux density.  $\mu_0$  is the permeability constant in vacuum. If we consider a field  $\mathbf{H}$  as a sum of field lines in a given volume, then  $\mathbf{B}$  is the density of those field lines. The unit of  $\mathbf{B}$  is T. The relationship of  $\mathbf{B}$ ,  $\mathbf{H}$  and  $\mathbf{M}$  is:

$$\mathbf{B} = \mu_0(\mathbf{H} + \mathbf{M}). \quad (1)$$

The effectiveness of the induction of a magnetic field is called the magnetic susceptibility  $\chi$ . The relationship between  $\mathbf{H}$ ,  $\mathbf{M}$  and  $\chi$  is as follows:

$$\chi = \frac{M}{H} \quad (2)$$

The susceptibility is dimensionless and it is specific for different materials. The susceptibility is directly tied to the permeability which is often written as  $\mu$ . The permeability is a measure for the resistance that a material offers against the formation of a magnetic field. The relationship of the permeability to  $\chi$  and  $\mathbf{B}$  is:

$$\mathbf{B} = \mu_0(1 + \chi)\mathbf{H} \quad (3)$$

The term  $(1 + \chi)$  is called the relative permeability  $\mu_r$  and is specific for each material.  $\mu_0$  and  $\mu_r$  can be combined and written only as  $\mu$  which is just the permeability. With these variables it is possible to describe most magnetic phenomena.

There are essentially three types of magnetism: these are diamagnetism, paramagnetism and collective forms of magnetism, which are antiferromagnetism, ferrimagnetism and ferromagnetism. All these forms occur in iron oxides and thus need to be understood to describe the properties of the different iron oxide species. Before I describe the different forms of magnetism, it is important to understand the building blocks of magnetic materials: the magnetic moments.

### 2.1.2.1 Magnetic moments

The magnetic moments are based on the electrons inside magnetic materials, more precisely on the motion of these electrons, since, as described above, a moving charge produces a magnetic field. There are two types of electron movement: the movement of the electron in its atomic orbital, the so-called orbital motion, and the spin of an electron. The momentum of the orbital motion is based on the principles of an electric charge moving in a closed loop. The area of the loop is the size of an atomic orbital and the current is the velocity of the electron. As the most basic orbital I assume the hydrogen 1s orbital and the equation for the orbital momentum is as follows:[13]

$$\mu(\text{orbit}) = eh/4\pi m \quad (4)$$

Here  $e$  is the charge of an electron,  $h$  is the Planck constant and  $m$  is the mass of the electron. The spin of an electron is not a movement in the classical sense but can be approximated by the electron spinning about its own axis, which gives it a defined magnetic moment and an angular momentum.[13] It was proven both experimentally and theoretically, that the equation for the spin momentum of the electron equals exactly the orbital momentum of the electron in the first Bohr orbital described in equation (4). This fundamental quantity was thus given the name *Bohr magneton* and the symbol  $\mu_B$  and it has the value of  $9.27 \cdot 10^{-24} \text{ Am}^2$ . This value is often used to quantify values of single particle magnetic moments.

### 2.1.2.2 Diamagnetism

Diamagnetism is the most abundant form of magnetism, yet it is seldom the dominant force. It is caused by the orbital movement of the electrons. When these moving electrons are subjected to an external magnetic field the induced field is directed in opposition to the external field, thus a diamagnetic body in a magnetic field will show a tendency to leave the field. Diamagnetism is prevalent in atom systems with closed shells, because in other systems uncompensated magnetic dipoles caused by free electron spins will overshadow the small diamagnetic effect. With closed shells the two spins in an orbital will cancel each other out. The strength of diamagnetism is dependent on the size of the orbitals so on the atomic number.

### 2.1.2.3 Paramagnetism

When there are electrons with an uncompensated spin in a system, these electrons react to an external field. This answer to the field is called paramagnetism. The free magnetic moments will align to any outside magnetic field, but once the field is switched off or falls in power under the thermal energy  $k_B T$ , the moments will fluctuate, excited by thermal energy. This process causes a paramagnetic material to increase its magnetization linearly with an applied external field and to also decrease linearly. The alignment of the magnetic moments to an external field  $\mathbf{H}$  is not a simple rotation into the direction of the magnetic field, but instead a precession of magnetic moments around the axis of the applied field. This happens because each atomic magnetic moment also possesses an angular momentum which is based on its orbital momentum and its spin. The frequency of the angular movement around the external field is called the Larmor frequency.

Although very interesting and useful, I will omit the quantum theory behind paramagnetism in this work. All magnetic measurements are explainable by the orientation of magnetic moments and we do not need to dive too deep into the topic of how these magnetic moments are made up to understand the effects.

### 2.1.2.4 Collective magnetism

The collective types of magnetism are ferromagnetism, ferrimagnetism and antiferromagnetism. All three of these types have effects several orders of magnitude stronger than the paramagnetic or diamagnetic types. The first person to give a valid theory on ferromagnetism was Pierre Weiss in 1906.[76] He postulated some kind of molecular field that helps the magnetic field in magnetizing a substance. His observations together with the observations of Pierre Curie gave birth to the Curie-Weiss-Law:[77]

$$\chi = \frac{C}{T - \Theta} \quad (5)$$

with:

$$C = \frac{\mu_0 \mu^2 n}{3k_B}. \quad (6)$$

Here  $C$  is the Curie-constant which contains the atomic magnetic moment  $\mu$ ,  $n$  which consists of the number of particles  $N$  divided by the volume  $V$  as well as Boltzmann's constant  $k_B$ . The last piece of the Curie-Weiss-Law is  $\Theta$  which is directly related to the molecular field introduced by Weiss.[13] The molecular field is defined by:

$$\Theta \propto H_m = \gamma M. \quad (7)$$

Here  $H_m$  is the molecular field and  $\gamma$  is the molecular field coefficient. The molecular field is the driving force behind the spontaneous magnetization of a ferromagnet.[13] It was postulated by Pierre Weiss and describes the interaction between magnetic moments. The molecular field is no real field, but it helps to think of it as a force that aligns the magnetic moments. This can in a more accurate way be described by the exchange interaction between neighboring spins in a quantum mechanical way. This was not known at Weiss's times, but later shown by Heisenberg.[78] Equation (5) describes the behavior of the susceptibility at different temperatures. When the temperature is elevated across a certain temperature – which is called the Curie-temperature  $T_C$ , when ferro- or ferrimagnets are concerned, or the Néel-temperature  $T_N$ , when antiferromagnets are concerned – the material behaves like that of a paramagnet.  $\Theta$  can take both positive values in the case of a ferromagnet and negative values in case of an

antiferromagnet. The molecular field either helps the alignment ( $T_C$ ) or hinders it ( $T_N$ ). If we look at the equation, we can see that there is a steep decline in susceptibility when the critical temperature is crossed, which means that the collective orientation of the magnetic moments in the material is breaking up. This is caused by the thermal energy that induces random orientation in the magnetic moments. Below the Curie temperature the spins spontaneously align parallel to each other in a ferromagnet, a process called spontaneous magnetization. This also happens when no field is present and was attributed to the molecular field by Weiss. Each spin is only influenced by its nearest neighbors but since these neighbors in turn influence other spins, a long-range order is established in a ferromagnet. The interaction between a spin and its neighbors is called the exchange interaction. This exchange interaction cannot be understood in a classical way, it happens only in the dimensions of single electrons and protons, a realm where the classical physical laws seldom hold true. Therefore, we need a quantum mechanical explanation for this force. When two electrons are extremely close to another and have the same velocity, they can only have the same energy if their spins are antiparallel to each other, this is the Pauli exclusion principle.[13] Since the electrons still have their electrostatic potential, the Coulomb interaction, this energy needs to be modified by spin orientations, the exchange interaction is therefore like the Coulomb interaction electrostatic in origin. When these two electrons occupy the same energy level, they become indistinguishable, so they can exchange places. When calculating the energy of a system with two atoms that each have these indistinguishable electrons, the term for the total energy must include this exchange possibility, thus an exchange interaction. The exchange energy can be written as:

$$E_{\text{ex}} = -2J_{\text{ex}}S_iS_j = -2JS_iS_j\cos\phi \quad (8)$$

Here  $J_{\text{ex}}$  is the exchange integral between two electrons and  $S_i$  and  $S_j$  are the spin angular momentum terms for each atom.  $\phi$  is the angle between the adjacent spins. When the exchange integral is positive the energy is at a minimum when the spins are parallel to each other so that the cosine term is 1, it is at a maximum when the spins are antiparallel so that  $\cos(\phi) = -1$ . For ferromagnetism to occur the exchange integral needs to be positive. Equation (8) is simplified and only applies to two atoms, when there are many atoms involved as in a particle system, the problem becomes immensely complicated.[13] The most important electrons for transition metal elements, such as iron, are the electrons of the 3d shell. Their

distance and interaction are the main determining factors for the magnetic properties of an atom. In Figure 6 the exchange energy is plotted versus the interatomic distance compared to the radius of the 3d electron shell. It is visible that the exchange interaction is positive, hence ferromagnetic, up to a point where the electrons are so close together that the exchange energy becomes negative and the interaction becomes antiferromagnetic. The exchange energy can also be used to explain the different curie temperatures for the elements, since stronger interactions need more thermal energy to be broken up and forced into random orientation.

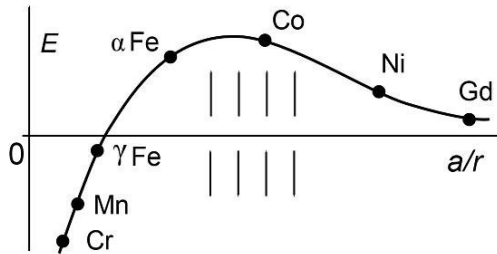


Figure 6: Bethe-Slater-curve for the transition metal elements.  $E$  is the exchange energy,  $a$  is the interatomic distance and  $r$  is the radius of the 3d electron shell.[79]

There are some things about ferromagnetism that cannot be explained satisfactory by the theories mentioned here, for example the exact values for some atomic magnetic moments. There are other theories that in turn explain these values but have other limits and holes in their explanation. This is not the place to give a detailed summary on the theory behind ferromagnetism, especially since no real ferromagnets were synthesized during this work. However, I did synthesize ferrimagnets in the form of magnetite and antiferromagnets in the form of goethite so a short introduction into these types of magnetism will be given.

### 2.1.2.5 Antiferromagnetism

Antiferromagnets have, like paramagnets, a small positive susceptibility at temperatures greater than absolute zero. However, their variation with temperature is completely different from the one observed for paramagnets. At 0 K, the magnetic moments in a paramagnet are aligned exactly antiparallel and the susceptibility is zero. The result is a net diamagnetic moment since all unpaired spins cancel each other out. The exchange interaction is again responsible for this behavior, but while it takes positive values in ferromagnets it is negative for antiferromagnets. The result is a splitting of the ionic structure into two ferromagnetic sublattices, which oppose each other. So, the moments are aligned in an ABAB fashion, where one moment A points up and one moment B points down. When the temperature is increased above zero the susceptibility increases until the Néel-temperature is reached, at which point it decreases in the same manner as a paramagnet. The increased susceptibility can be explained by the thermal energy working against the eagerness of antiferromagnetic materials to align antiparallel. When the temperature is increased the susceptibility also increases because the thermal energy breaks some moments out of their sublattice and flips their spins so a net magnetic moment might be induced by an applied field. Antiferromagnetism is often found in ionic compounds like oxides or chlorides. In these materials the atoms are not direct neighbors but there is an interaction between them anyway. In this case the interaction is mediated by the ligand via a super exchange process.[80] This process is dependent on the angle that is spanned between the magnetic ions and the ligand in the center. If this angle is for example at about  $90^\circ$  then the interaction is ferromagnetic and if the angle is  $180^\circ$  it is antiferromagnetic. The super exchange process is an interaction between the d-orbitals of the magnetic ions and the p-orbital of the bridging ion.[81] The electrons from the d-orbitals can hop to the p-orbital and interact there similar to the interaction of neighboring atoms.

Antiferromagnetism is of great importance to this work, because a big part of my thesis was spent working on goethite, an antiferromagnetic material.

### 2.1.2.6 Ferrimagnetism

Ferrimagnetic materials act like ferromagnets but have the magnetic substructure of antiferromagnets. These two are compatible because there are two different magnetic species present in ferrimagnets. These build their own sublattices that are ordered antiparallel to each other, analogous to the arrangement in antiferromagnets. The difference is that one of the magnetic species produces a stronger net magnetic moment than the other species resulting in a unidirectional net magnetic moment. The exchange between the different species in the different sites in the crystal lattice happens as described before by the super exchange mechanism. The most notable iron oxide species of ferrites are magnetite and maghemite, both have been synthesized in this work.

### 2.1.2.7 Magnetic anisotropy

Since one of the main topics of this work was the anisotropy of magnetic particles, their magnetic anisotropy cannot be left unmentioned. There are two main forms of magnetic anisotropy that play a role in this work. These are the magneto crystalline anisotropy and the form anisotropy. The magneto crystalline anisotropy is intrinsic to a material and based on the crystal structure. The form anisotropy is induced into the material by the synthesis conditions, it is only influenced by the morphology of the crystal.

The magneto crystalline anisotropy is responsible for the existence of an easy axis in magnetic materials. The easy axis is the direction of the spontaneous magnetization from a demagnetized state. The easy axis is the axis with the highest symmetry in the crystal lattice, for a cubic crystal, like magnetite, the easy axis is the  $[111]$  direction. When a crystal is magnetized along another axis the field strength needed to saturate the material is quite a lot higher than for the easy direction. To understand why this happens we need to first have a look at magnetic domains.

When the magnetic properties of a magnetic material are measured without prior influence of a magnetic field, one will measure no net magnetic moment. This is odd since we learned that the exchange interaction directs neighboring magnetic moments into parallel/antiparallel alignment and thus magnetizes the sample. This behavior was also observed by Pierre Weiss in 1906 and he postulated that a magnetic material is divided into domains. Each domain is magnetized to saturation, but neighboring domains are ordered in a way to cancel



each other out, so the material has no net magnetization. This process takes place because the field, which is produced by a magnetic material, takes up energy. This energy is called the magneto static energy. Since field lines always follow the shortest way from a north pole to a south pole, a material with one domain has a long way from north to south. With two domains that are oriented antiparallel the way to the next south pole can be reduced significantly (Figure 7A). So, by splitting into domains the material reduces the energy that is lost to produce the magnetic field outside of the material. The boundary between two domains is called a domain wall. The creation of a domain wall in turn takes up energy because the exchange interaction must be overcome. The size of a domain is a balance between the magneto static energy and the energy needed to create a domain wall, so the average domain size is proportional to the ratio between the two. The inner workings of domain walls, their movement and the physics involved will not be discussed here, as most particles discussed in this work are single domain particles.

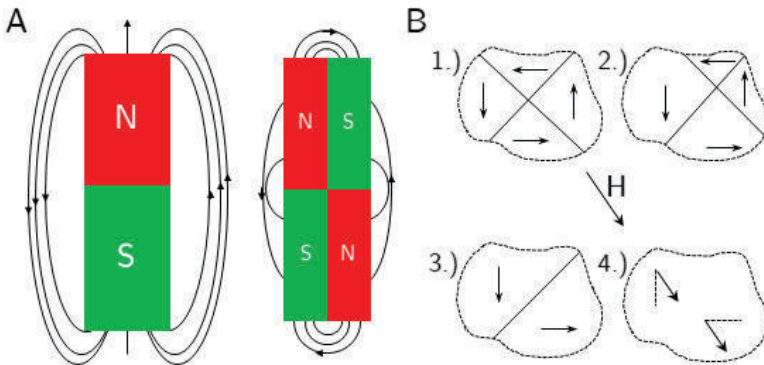


Figure 7: Schematic for the division of a magnetic material into domains. (A) The reduction of the magneto static energy with the reduction of the domain size. (B) The movement of domain walls in an applied magnetic field that is off the easy axis.

At first the domains oriented most favorable to the magnetic field grow, by moving its domain walls, which reduces the size of the less favorable oriented domains. When the field strength is further increased there are only two domains left, each with the same favorable orientation to the field. Now the only way the

magnetization can be further increased is by rotating the magnetic moments in each domain out of their easy axis into the direction of the magnetic field (Figure 7B). This is not as efficient as moving a domain wall because instead of flipping single spins the direction of every single magnetic moment needs to be reoriented into the direction of the applied field. The energy required to turn the magnetic moments away from the easy axis is termed the crystal anisotropy energy. The origin of the magneto crystalline anisotropy lies in the coupling between spins and orbits. The orbits are generally coupled to the crystal lattice by very strong interactions, so the only way to reorient the spins is to “uncouple” them from the orbit.

A measurement of the magnetization process in the form of an  $M/H$  curve is shown in Figure 8. The different phases of magnetization described before (Figure 7B) are highlighted in color. The initial magnetization happens by domain wall movement, so the energy requirements are quite low, leading to a very steep curve, here shown in blue. When the final two domains are formed, the further magnetization happens by turning the magnetic moments into the direction of the external field. This requires more energy, so the slope flattens, depicted in green. The next phase of the magnetization is the saturation, when all magnetic moments are aligned with the field, this region is shown in red. The last phase or feature of the magnetization curve is the region at and around  $H = 0$ , where we can see the remanent magnetization and the coercivity, depicted in yellow. Since the sample in observation here contained only very small particles, there is no visible remanence and the coercivity is quite small, here shown in yellow. For larger samples, the curve divides in the blue area and forms a hysteresis.

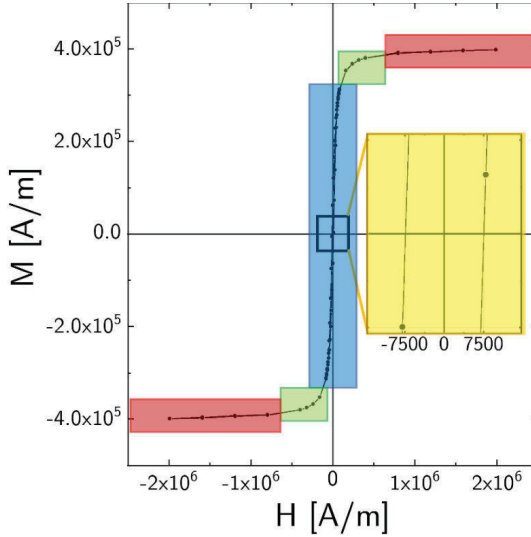


Figure 8: Magnetization curve displayed in a  $M/H$  diagram. The colored regions are visualizations of the different areas of a magnetization curve. Yellow inlay: Region of coercivity. Blue: Region of domain wall movement. Green: Realignment of magnetization. Red: Saturation region. The regions are chosen arbitrarily and just for visualization purposes.

Apart from the intrinsic magneto crystalline anisotropy there are also the extrinsic anisotropies, the one most relevant to this work the form anisotropy. This anisotropy is based on the different magnetizabilities for axes of different lengths. A particle with one long and one short axis without pre-oriented crystal grains, so no magneto crystalline anisotropy, will be easier to magnetize along its long axis compared to its short axis.

To understand this behavior, we need to have a look at the demagnetizing field which makes the difference between long and short axis. The demagnetizing field is created when a material is magnetized, and the magnetizing field is removed. The  $B$ -field stays as expected and forms the outer magnetic field going from the north to the south pole of the magnet. But in addition to the  $B$ -field there is also an  $H$ -field going from north to south *on the inside* of the magnet which reduces the effective magnetization. This field is called the demagnetizing field. This field is stronger at the poles than in the middle of the magnet. Another good

explanation for the shape anisotropy is the density of the magnetic poles on the surface of a particle. In small particles the magnetization is uniform across all magnetic moments but the poles on the surface are uncoupled. By distributing the magnetic poles on the surface along the long axis a smaller area compared to distribution along the short axis is covered by the poles, which reduces the energy. A good visualization is given in Figure 9.

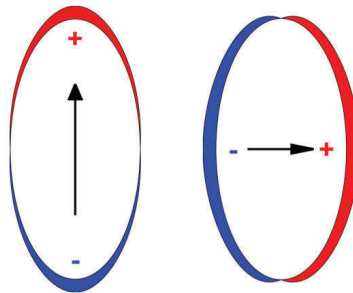


Figure 9: Illustration of the distribution of magnetic charges on the surface of a single-domain magnetic particle. The arrow indicates the direction of magnetization. The thickness of the colored region displays the density of the magnetic poles.[82]

#### 2.1.2.8 Size effects

Most of the aforementioned effects are mainly relevant for materials in their bulk form. When the particles size nears the nanometer realm, most physical effects need to be revisited. When the size of a magnetite particle nears 50 nm the energy required to form a domain wall is larger than the energy lost by magneto static effects. The result is a particle with only a single domain. This single domain particle is always magnetized to saturation, as all moments are aligned in the same direction. This does not mean that it is always at a constant magnetization when measured, because the magnetization direction is not necessarily in field direction, but a very small field is sufficient to realign the moments into field direction and to reach saturation. However, this is only the case when the anisotropy of the particle is low. The field required to reach saturation increases proportional to the anisotropy.

Up to the limit where the surface of the particles plays an important role for the properties of the particles, the saturation magnetization is independent of the particle size. However, the coercivity is strongly dependent on the particle size.

When we near the single domain range from the multidomain particle size, an increase in coercivity is noted. This is based on the increasing scarceness of domain walls that can easily be moved to reorient magnetic moments. When we reach the single domain size threshold the coercivity reaches its maximum. The only way to change the orientation of the magnetic moments is by spin rotation. When the size is further decreased, the coercivity also decreases, because of thermal effects. Finally, at a particle size below  $\sim 36$  nm for magnetite, the coercivity reaches zero, at this point the particles are called superparamagnetic.[72] Superparamagnetism occurs because the exchange interactions are not strong enough to prevail against the disorder introduced by the thermal energy, the sample is demagnetized as soon as an external magnetic field is absent. The magnetization curve is similar to that of a paramagnet, in the way that there is neither a coercivity nor a remanence. The striking difference is the large change in magnetization when even a small field is applied, that is why it is called *super*paramagnetism. This behavior is also visible in Figure 8, here shown on spherical magnetite particles with a size of about  $22 \pm 8$  nm. The upper limit for particle size is strongly dependent on the synthesis conditions but there are sources that place it between 29 and 36 nm for magnetite.[72]

### 2.1.2.9 Micromagnetism

Micromagnetism is used as a theoretical model to predict the behavior of particles in a sub-micrometer scale. The particles are treated not as an ensemble of singular magnetic moments but as a mostly continuous bulk, albeit a very small one. The goal is to integrate quantum mechanical models like the exchange interaction with a classical continuous field description of the magnetization.[83] This theory allows the description of magnetization dynamics on the micron scale. Depending on the properties of a magnetic material the total energy of the system is made up of different contributions. All of them are displayed here:

$$E = E_{\text{exch}} + E_{\text{anis}} + E_{\text{Z}} + E_{\text{demag}} (+E_{\text{various}}) \quad (9)$$

Here  $E_{\text{exch}}$  is the exchange energy,  $E_{\text{anis}}$  is the anisotropy energy,  $E_{\text{Z}}$  is the Zeeman energy,  $E_{\text{demag}}$  is the energy of a demagnetizing field and finally  $E_{\text{various}}$  is the contribution of other effects that apply only for some materials. In this formula  $E_{\text{various}}$  can be replaced by different energy terms, for example magneto-elastic energy or interlayer-exchange energy but we will not be needing these terms to

understand the effects observed in this work. Most of these energies were discussed earlier except for the Zeeman energy, so I will only make additions that come into play in the microscopic dimensions. For the exchange energy there is the general expression of:

$$E_{exch} = A \int ((\nabla m_x)^2 + (\nabla m_y)^2 + (\nabla m_z)^2) dV. \quad (10)$$

Here  $A$  is the exchange constant that is derived from the crystal structure and is material specific. The rest of the expression is minimized when the magnetization is uniform across the sample. The anisotropy energy  $E_{anis}$ , is the energy that aligns the magnetization to the easy axes of a crystal:

$$E_{anis} = \int_{\Omega} [K_{c1} (m_1^2 m_2^2 + m_2^2 m_3^2 + m_3^2 m_1^2) + K_{c2} m_1^2 m_2^2 m_3^2] dx \quad (11)$$

This equation is applicable for a crystal structure with cubic symmetry.  $K_{c1}$  and  $K_{c2}$  are the anisotropy constants. The sign of the anisotropy constants decides whether the material behaves ferro- or antiferromagnetic. The integration happens over the entire magnetic volume  $\Omega$ .

The Zeeman energy  $E_Z$  describes the influence of an external magnetic field on the energy of a magnetic material:

$$E_Z = -\mu_0 \int_V M H_{ext} dV. \quad (12)$$

Here  $M$  is again the magnetization and  $H_{ext}$  is the applied external field that acts on the entire volume  $V$ .

The demagnetization energy  $E_{demag}$  accounts for the dipole-dipole interaction of a magnetic system. Here it acts like the macroscopic magneto static energy often also called the stray field energy:

$$E_{demag} = -\frac{\mu_0}{2} \int_V M H_{demag} dV \quad (13)$$

The energy is minimized when the number of magnetic poles on the surface is minimized. This can lead to the formation of a curl-like formation, where the magnetic moments are aligned parallel to all surfaces. This way the net magnetization without an applied field is again 0. In the case of one domain particles this configuration is of course impossible, here this energy term cannot

be minimized and is compensated by minima in the other terms, so the total energy is minimized.

The last term can be displaced by other terms depending on the system. The energy can for example be influenced by elastic distortions of the crystal lattice, then it is magneto-elastic energy or magnetostriction. If the material in focus is made up of different layers, there is interlayer exchange interaction and possibly also antisymmetric exchange interaction. In our case we observe mostly one-domain to superparamagnetic particles with a single phase, so only the first four terms of the total energy will be treated.

### 2.1.3 Orientational phenomena

Using a micromagnetic model we can understand that the orientation of particles in a magnetic field is always based on the competition between the different terms of the free magnetic energy. Let us consider the case of a spherical one-domain ferromagnetic particle that is subjected to an external magnetic field. In the one-domain case all magnetic moments point along an easy axis in the case of no applied field, so the magnetization is uniform across the sample and the term for the exchange energy is easily minimized. The anisotropy energy binds the magnetic moments to the crystal lattice. The anisotropy constants in a ferromagnetic material are positive so the magnetic moments in the sample are aligned parallel, so this term is responsible for the remanent magnetization. The demagnetization energy for this case was already discussed in the previous paragraph, the demagnetization energy of a one domain ferromagnetic particle cannot be minimized since the moments are bound strongly by the anisotropy and exchange energy and these compensate the demagnetizing field.

The Zeeman energy or the energy of the external magnetic field remains. Since this is the only term changing with an applied field and the particles change their orientation this term must be responsible for the orientation. The moments are oriented internally in the direction of the magnetization  $M$  and the external field  $H_{\text{ext}}$  is exerting an energetic pull in the direction of the field. Now the particles have two options to minimize the Zeeman energy: One is that the whole particle rotates until the magnetization is parallel to the applied field, the other is that the particle does not rotate but all magnetic moments perform a spin flip into the direction of the field. These types of motion are termed Brownian or Néel relaxation, respectively.[84,85] In the case of a ferromagnet we assume that the magnetic moments are bound quite strongly by the crystal anisotropy so the

favored option would be the Brownian relaxation of particle rotation. But what if the particles are deposited into a matrix and are unable to rotate? Then the dominating process is the Néelian relaxation and the crystal anisotropy energy needs to be overcome to orientate the magnetization. Both relaxation processes happen under energetic losses which can be used to generate heat in hyperthermia applications.[46]

Spherical particles do not orient in a magnetic field but rather rotate to follow the field, which is not visible by optical methods. If the particle is anisotropic the orientation of the particle in the field is easily visible. As outlined in the magnetic anisotropy section 2.1.2.7 the magnetization in an object with one elongated axis is bound to the long axis by the demagnetization energy.

When we are not dealing with ferromagnets but with antiferromagnets, things get a little bit more complicated. The resulting energy contributions will be outlined here on the thesis relevant case of goethite. The model was applied to the system by Lemaire *et al.*[68] in the first work about the magnetic properties of the goethite system. The relevant energies are essentially the energy that is brought in by the external field in form of the Zeeman energy, in the form of the field and the induced magnetization, and the interaction of the field with the particle dipole, so with the anisotropy energy:

$$E_m(\theta) = -\mu B \cos\theta - \frac{\Delta\chi V}{2\mu_0} B^2 \cos^2\theta \quad (14)$$

Here  $\theta$  is the angle between the applied field ( $\mu B$ ) and the magnetic moments of the goethite rod.  $\Delta\chi$  is the difference between parallel and perpendicular susceptibility, *i.e.*  $\Delta\chi = \chi_{\parallel} - \chi_{\perp}$ ; this value is negative in the case of an antiferromagnet. Since the susceptibility and the volume  $V$  of the particle are very small the second term is also small for low fields. The first term governs the total energy for low fields, and this is also the energy that is minimized when the angle between particles and field is 0, so the particles orient parallel to the field. The second part of the equation depends quadratic on the applied field, so it grows faster at higher fields than the first term. The second term is minimized when the orientation to the field is perpendicular because of the quadratic cosine term. This means the goethite particles shift their orientation at a certain field threshold. There is also a region in between where the energy prefers a finite angle to the field, in an experiment the orientation appears isotropic in this region.



## 2.2 Multiresponsive materials

Multi responsive materials are defined as materials that change their properties when subjected to more than one stimulus. There is a wide range of stimuli that can be applied, in our case the system responds to pH, temperature and a magnetic field. The responsiveness to pH and temperature is based on the chosen polymer system PNIPAM and the magnetic responsiveness is based on the magnetic cores. The following chapter will first describe the physio chemical basis for thermoresponsiveness in general and particularly for PNIPAM. In the end I will shortly describe the connection between the hydrogel and the magnetic particles.

### 2.2.1 Thermoresponsiveness

From the definition on Wikipedia: “*Thermoresponsive polymers are polymers that exhibit a drastic and discontinuous change of their physical properties with temperature.*”[2] The physical properties concern mostly the solubility in a given solvent but in general any physical property could be changed. The change is discontinuous which means the change happens abruptly and non-linear at a given temperature. For polymers, the term thermoresponsive mostly means that the polymers display a miscibility gap in its phase-diagram. They are soluble above or below their transition temperature and precipitate when that temperature is crossed. When the change happens upon an increase in temperature the point is called the lower critical solution temperature (LCST) and correspondingly upper critical solution temperature (UCST) when the polymer is soluble only above that temperature. The responsiveness is accomplished by having a balance of hydrophilic and hydrophobic groups in the polymer. When the balance is changed by changing the content of either group the transition temperature can be tuned.[6] The mechanism of property change is a phase separation because the suddenly insoluble solvent phase is pushed out of the polymer system, which is measurable in a sudden change of volume by different methods like for example dynamic light scattering (DLS).

The physics behind the solution and precipitation of polymers is best understood by the Gibbs energy of the system:

$$\Delta G_{\text{mix}} = \Delta H_{\text{mix}} - T\Delta S_{\text{mix}} \quad (15)$$

When the Gibbs energy  $\Delta G_{\text{mix}}$  is negative, the process, in this case the solvation of a polymer, happens voluntarily, otherwise energy must be brought into the system. The energy is mostly introduced by heating the mixture, and thus increasing the entropy  $T\Delta S_{\text{mix}}$  term. The interactions and their energy contribution introduced into the system when the polymer mixes with the solvent are displayed by the enthalpy of mixing  $\Delta H_{\text{mix}}$ . The interactions between polymers is also what brings about the LCST. When the temperature is increased, the polymer chains increase their kinetic energy and thus move about, bringing interacting groups closer together thus introducing their interactions. Generally, more movement increases the disarray in a system and thus the entropic proportion, but in this case polymer-polymer interactions are introduced as well which lower the entropy term, so the Gibbs energy becomes net positive, leading to demixing and thus precipitation of the polymer. A more detailed explanation will be given on the example of PNIPAM.

### 2.2.1.1 The Allstar: PNIPAM

PNIPAM is probably the most studied thermoresponsive polymer and was the “gold-standard” of thermoresponsive polymers for many years.[86] This is owed not only to its LCST of 32 °C that is close to the human body temperature, but also to the relative insensitivity of the LCST to the chemical environment of the polymer. Slight changes in the pH or concentration of the polymer will not shift the transition temperature significantly, while other polymers change their behavior quite drastically, e.g. by a vanishing LCST upon protonation. The structure of PNIPAM is shown in Figure 10A.

PNIPAM contains both a hydrophobic group, the *N*-isopropyl group, and a hydrophilic group, the acrylamide. The hydrophobic backbone and the hydrophilic amide group have different effects on the surrounding water molecules. The hydrophobic backbone has an ordering effect on the water molecules because they cannot form hydrogen bonds with it and must order around its excluded volume, this results in a positive entropy of mixing. The hydrophilic group forms hydrogen bonds with the surrounding water molecules, which increase the enthalpy of mixing. The coil-to-globule collapse that happens at the LCST is an endothermic effect because originally the polar acrylamide group prefers connections to the aqueous solvent because of the formed hydrogen bonds rather than intramolecular bonds.[87] During the process the degrees of freedom of the water molecules are increased, because it does not have to form

hydrogen bonds to the rigid polymer and the free volume it can occupy increases due to the collapse of the polymer chain.

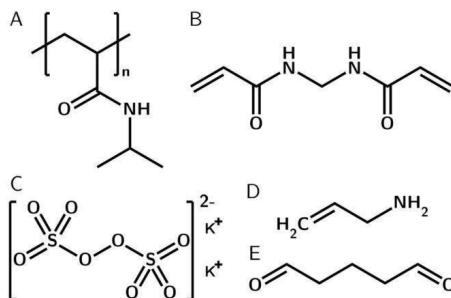


Figure 10: Chemical structures of the educts in the NIPAM polymerization. (A) PNIPAM-polymer (B) N,N-Methylene-bis-acrylamide (BIS) (C) Potassiumperoxodisulfate (KPS) (D) Allylamine (AA) (E) Glutaraldehyde (GA)

So below the LCST the system is dominated by the enthalpy created by hydrogen bonds and above the LCST the entropy gained by granting the water molecules more freedom causes the collapse of the PNIPAM chain.

Since the PNIPAM presented in this work is part of a hydrogel it needs to be crosslinked and is thus copolymerized with BIS (Figure 10B). Since BIS possesses more polar groups than PNIPAM the LCST is shifted too slightly higher values, in experiments this is mostly visible in a slightly smeared transition region. The same can be said about the addition of AA (Figure 10D) to the polymer, since the amine groups also increase the solubility in water. The initiator KPS (Figure 10C) fulfills a double role in the hydrogel system. Besides starting the radical polymerization, the strongly charged remaining sulfate groups provide a charge stabilization that prevents precipitation above the LCST.

### 2.2.2 Magneto responsiveness

Any material that responds to the introduction of a magnetic field with an answer that is dependent on the strength of the magnetic field can be called magneto responsive. The answer to the magnetic field is dependent on the material and the applied magnetic field. For example there is a whole research field focused on the heating of nanoparticles by an alternating current (AC) magnetic field.[46,88,89] Here, the nanoparticles heat up because the magnetic moments try to follow the magnetic field which changes direction at the frequency of the AC field. This movement of the magnetic moments causes internal and external friction in the particle and the surrounding matrix, so the particle heats up. This can be utilized to trigger a temperature transition in a thermoresponsive matrix.[90]

Another answer to an applied magnetic field is the movement of particles along field lines. This happens mostly in gradient fields, where the particles try to move to the region with the highest applied field. This can be utilized for example in magnetic separation.[10,91] Here the particles are again trapped in a matrix, this matrix can be tailored to specifically target contaminants like heavy metals in polluted water. Once the contaminants are trapped the composite can be simply attracted by a magnet, the release of the contaminants is triggered, and many materials can easily be regenerated after the procedure for further use. A similar method is also utilized for cell separation, where magnetic particles are functionalized to specifically target the desired cells, so they can be subsequently separated.[10]

The last effect I want to mention here is the magneto-rheological effect. This effect is utilized in magnetorheological fluids, where micrometer sized magnetic particles are dispersed in a carrier liquid, usually a viscous oil. The fluid rapidly changes its viscosity when a magnetic field is applied, and the viscosity can be accurately controlled by varying the field strength.[92] The effect is caused by the magnetic particles which can move freely by Brownian motion in the liquid. Once a magnetic field is applied the particles align parallel to a magnetic field. When the field is applied perpendicular to the flow of the liquid, the particles experience the competition of the shear forces which rotate the particles in flow direction and the magnetic forces which rotate the particles back to parallel orientation. This increases the viscosity of the fluid. Another important effect is that magnetic particles will form chains by following the field lines of the magnetic field. These chains are more rigid than the isolated particles so as long as the field persists, the viscosity of the liquid is increased.

## 2.3 Hydrogels

A hydrogel is a network of polymer chains that is swollen with water but does not dissolve in water. The polymer chains are crosslinked together to improve the structural integrity of the hydrogel and this composite allows for a very high water content of more than 90 %. In the presented case the crosslinking is done by BIS or GA (Figure 10B,E). Hydrogels closely resemble organic tissue so they find applications in medicine and bioengineering.[93,94] In this chapter I will briefly outline the intricacies of micro and macrogels and their key properties.

### 2.3.1 From microgels to macrogels

Where interconnected networks are concerned one needs to differentiate between micro- and macrogels. A microgel consists of disperse intra-molecularly connected polymeric particles that are uniformly dispersed in a good solvent medium.[95] A macrogel is a large interconnected structure that does not need but can be dispersed in a solvent medium. In this work we present both micro and macrogels with two different synthetic models. The first starts at magnetic particles and the microgel is grafted around these particles, anchored by covalent bonds. The second starts with the synthesis of a macrogel which is later mixed with magnetic particles.

In the covalently bound case, we first synthesized microgel beads by polymerizing NIPAM together with BIS. The outer shell of the microgel was subsequently functionalized with AA to enable the transition into a macrogel. The macrogel system was established by crosslinking the AA functional groups with GA.

#### 2.3.1.1 Covalently bound system

To create a system where the particles are covalently bound to the matrix, we started by surrounding the magnetic particles with a silica shell. This was done to prolong their colloidal stability and to make use of the easily accessible silane chemistry. The silica synthesis is a polycondensation and will be treated in its own section (section 2.4.1). On the surface of these core shell particles we added a methacrylate function by adding TPM to the system. In the following polymerization the growing PNIPAM chains can incorporate the methacrylate double bond into their backbone and are thus covalently bound to the magnetic particle. The polymerization is done as a free radical emulsion polymerization that

is initiated by KPS. To stabilize the emulsion, sodium dodecyl sulfate (SDS) is added to the solution. The details and background of the polymerization will be given in their own section (section 2.5.4). In the late stages of the polymerization AA is added to the system which provides its terminal amine groups for crosslinking of the microgel beads. The crosslinking happens only after the reaction is finished and subjected to thorough washing to remove leftover monomer or TPM. The sample is concentrated to increase the probability of two amine functions being in close vicinity. The crosslinking happens using GA. GA provides two terminal aldehyde groups which selectively crosslink amine groups. Not only the amine groups on the outer shell originating from the allylamine are able to be crosslinked but also the secondary amine groups on the inside of the microgel. The inner secondary amine groups were utilized in the second system presented in this work that is in the following described as a loosely connected system. For the covalently bound system we assume that mostly the amine groups on the allylamine will be crosslinked, because these are more exposed to the outside.

#### 2.3.1.2 Loosely connected system

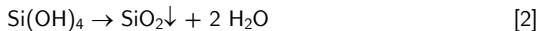
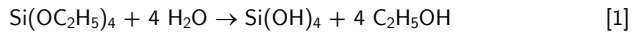
In the second approach, the synthesis of the magnetic particles and the synthesis of the hydrogel are separated. The particles are synthesized as usual, stabilized in aqueous solution and later mixed with the hydrogel, while the hydrogel is synthesized without any particles present. The hydrogel is a composition of PNIPAM crosslinked by GA polymerized again in a free radical emulsion polymerization with KPS as the initiator. The polymerization happens at a temperature above the LCST of PNIPAM, so upon reaching sufficient molecular weight to form a random coil the PNIPAM molecules collapse and are stabilized by SDS and the sulfate groups left over from the initiator. This way there are mostly PNIPAM microgel beads crosslinked by GA in a similar fashion to the covalently bound gel. Since there are no particles present in this reaction the concentration of the reactants can be increased without the risk of agglomeration. The gels created with this method are usually more concentrated than their covalently bound counterparts. The particles can be simply added to the hydrogel and get mixed within the matrix by stirring or shaking. Since there are no specific interactions between the particles and the gel (unless the particles are functionalized by binding ligands) the particles can leave and enter the gel at random in the swollen state. The distribution of particles inside this matrix was one of the main research interests of this work.

## 2.4 The bridge connecting core and shell

To connect the magnetic core with the thermoresponsive PNIPAM shell the particles need a functionality that can bind to both polymer and particle. We close this connection by coating the particles with a silica shell that fulfills multiple purposes: It renders the particle more stable against agglomeration, makes them chemically mostly inert and makes them easy to functionalize by silane chemistry. This chapter will give a short overview over the different reactions we employed to synthesize the silica shells and their theory. The end of the chapter will treat different stabilization techniques for nanoparticles.

### 2.4.1 Silica shell

The silica shell is made of silicon dioxide ( $\text{SiO}_2$ ). The shell is formed by a polycondensation, the most prominent synthesis was designed by Stöber and coworkers in 1968.[45] The condensation happens in ethanol and is base catalyzed by ammonia. As the monomer for the silica formation, tetra ethyl orthosilicate (TEOS) is used. This reaction was later picked up and tailored to different particle systems by Graf *et al.*[43] Here, poly-vinylpyrrolidone (PVP) was used to stabilize the particles prior to the silica coating. Particles grown with this technique will be less polydisperse the thicker the silica shell becomes, because the growth happens on a molecular level.[43] The growth in any reaction using tetra alkoxyasilanes happens as follows:[96]



In the first reaction step the alkoxyasilane is hydrolyzed to its silicon hydroxide form. The second step is the polycondensation step where the  $\text{SiO}_2$  species is formed. The whole process is catalyzed by ammonia which also gives the silica particles grown by this method a negative surface charge. The speed determining step of this reaction is the hydrolyzation of monomers. The particle growth happens by addition of small building blocks, like dimers, trimers, or oligomers. It was shown that the final size of the particles is dependent on the number of nuclei formed early in the reaction and their colloidal stability.[96] This means that a small number of particles at the start will produce big particles and a large

number leads to small particles. The colloidal stability is dependent on the amount of ammonia and water in the system because the concentration of both will influence the concentration of  $\text{NH}_4^+$  and  $\text{OH}^-$  which ultimately determines the thickness of the stabilizing double layer. At the surface of the growing silane particles there exists a potential that leads to the aggregation of small silica species to further growth. This potential is diminished the further the particle grows until colloidal stability is reached. When this growth mechanism is continued over some time the polydispersity of the whole ensemble reduces following a  $1/R$  law, where  $R$  is the particle radius.

Apart from the Stöber process, we also employed a second reaction procedure that relied on water as a solvent instead of alcohol, with the intention of skipping the phase transfer step from water into ethanol. This method is based on a paper by Zou *et al.* [44] For this method, the magnetic particles are stabilized in aqueous medium and well dispersed. Hydrazine and ammonia are then added to the reaction as catalyst and base. Lastly TEOS is added to the mixture to start the polycondensation that forms the silica shell. Since TEOS is hardly soluble in water it forms small droplets in water, a second phase, therefore this method was termed the bi-phase method. The hydrolysis of TEOS should occur only at the interface between the water and the TEOS phase, so the reaction is quite well controlled. Hydrolyzed TEOS should only nucleate at the surface of iron particles so heterogeneous nucleation is needed. This is achieved by keeping the concentration of  $\text{SiO}_2$  low. Higher concentrations lead to homogeneous nucleation due to supersaturation and to the formation of free silica particles. When the reaction continues the TEOS droplet size is reduced, therefore reduces its surface area and slows the reaction down. Further continuing the reaction leads to the disappearance of the droplets and thus stops the silica shell growth. When new TEOS is added new droplets are formed and the growth can be resumed, leading to finely tunable shell thicknesses.

Hydrazine is added to this reaction to act as a catalyst. The dispersibility of the  $\text{Fe}_3\text{O}_4$  particles is increased due to formed negative surface charges and the surface oxidation of magnetite in air is suppressed.

The reaction is carried out at relatively high temperatures of 90 °C to speed up the reaction and to eliminate unwanted alcohol in the system.



### 2.4.1.1 Stabilization techniques

A silica shell synthesis is deemed successful when there are no free silica particles and there is only one particle per shell that is evenly covered by silica. The most challenging part in achieving this is getting exactly one particle inside the shell instead of a small cluster. Success depends on effective stabilization prior to the silica shell synthesis. Depending on the preferred method for silica synthesis the particles need to be first soluble/dispersible in water or ethanol at high pH.

Generally, stabilization is achieved by one of two methods: Charge stabilization or steric stabilization. For steric stabilization there are several polymers that are regularly employed that are often simply adsorbed to the surface of the nanoparticles by an anchoring group. Polymers in common use which are also employed in this work include various PEG variants (Figure 11A), PVP (Figure 11B). There are also more biologically close polymers like dextran or chitosan.[97,98] Most uncharged polymers stabilize by steric repulsion which means their excluded volume does not allow other polymer-stabilized particles into the vicinity of the nanoparticles so they cannot agglomerate. A short overview of the stabilizers employed in this work will be given at the end of this chapter.

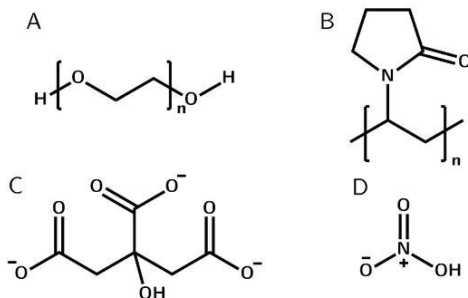


Figure 11: Structure formula of the used stabilizers. (A) PEG (B) PVP (C) Citrate (D) Nitric acid.

Charge stabilization means that molecules with a positively or negatively charged functional group are adsorbed or bound to the surface of the nanoparticle. This can happen by using acidic groups like carboxyl groups in the case of citrate

or by using strong acids or bases to charge the surface of the nanoparticles directly. The charged moieties will create an electrochemical double layer that repels other ions that are similarly charged, preventing agglomeration.

PEG (Figure 11A) is a widely used polymer due to its biocompatibility and easy accessibility. It is commonly used in cosmetics to warp the texture of pastes.[99] Also as a stabilizer for nanoparticles it has a “stealth” effect on nanoparticles that makes it possible to prevent the particles from being attacked by the body’s immune system by essentially hiding the particles in an inconspicuous shell.[100] It is often conjugated with other polymers to form a block copolymer, mostly because of its excellent solubility in water and biocompatibility.[101] In this work it found more application as a structure guiding agent than as a stabilizing agent, because of the extensive literature on PEG guided nanorod synthesis.[22,23,102]

The second polymer used in this work is PVP (Figure 11B). This polymer is also very well soluble in water as well as in alcohols. The polymer is available in different lengths that are suitable to coat different nanoparticle sizes.[43] It attaches well to the iron oxide surface and allows the deposition of  $\text{SiO}_2$  to form a silica shell, making it ideal for our purposes. PVP is nonionic, meaning its stabilizing properties are solely based on steric repulsion, so the amount of PVP adsorbed on a surface is quite important for the stability.

The group of charge stabilizers is led by citrate as it is the molecule we used the most to stabilize nanoparticles (Figure 11C). Citrate has three carboxylate groups which perform well in anchoring the molecule to the particle or to stabilize the complex by their negative charge. Depending on the pH, a different number of carboxylate groups will be coordinated to the nanoparticle. Also the carboxylate groups provide anchoring points for further functionalization if that is desired.[103]

Most charge stabilization is done by depositing charges at the surface of nanoparticles. This process is called peptization and done by simply mixing nanoparticles with an electrolyte. The choice of the counter anions to the peptizing agent is very important, as heavily polarizing agents lead to flocculation while a low ionic strength favors peptization. The actual stabilizing agents in this case are the  $\text{H}_3\text{O}^+$  and  $\text{OH}^-$  moieties on the surface of the nanoparticles. These are also the reason why nanoparticles stabilized in this way are only stable in either acidic or alkaline media, because at a pH of 5 to 9 the charges are neutralized and the particles flocculate. The peptizing agent of choice in this work was mostly nitric acid (Figure 11D), so the counter ions are  $\text{NO}_3^-$  anions. The surface of the particles is charged positively during the etching process, which creates an electrostatic field which affects the ions in the surrounding liquid,

pulling the oppositely charged  $\text{NO}_3^-$  anions to the surface until they form a dense monolayer of ions, the stern layer. The stern layer screens the particles from interactions with other ions in solution and effectively also from other particles. Outside of the stern layer forms a less dense layer of differently charged ions, that are attracted by the coulomb force of the charged particle surface. This layer is called the diffuse layer and its outside is the slipping plane, meaning ions on the outside of the slipping plane notice only a strongly reduced potential from the core itself. This potential is also called the  $\zeta$ -potential and is often used as a measurement for the colloidal stability of particles. The stern layer and the diffusive layer together form the electrical double layer around particles. The size of the double layer is influenced by the ionic strength of the surrounding solution, if the ionic strength is high the double layer is compressed, until particles agglomerate at very high ionic strengths. The size of the double layer can be “regenerated” or re-expanded by washing with deionized water, as this reduces the ionic strength.

Since the surface of the particles is etched by the strong acid, the acid needs to be removed by washing with deionized water to preserve the desired particle size and to expand the electrical double layer.

## 2.5 Synthesis

In this chapter I will discuss the theoretical details behind the synthesis of nanoparticles, their silica shell, and the hydrogel. This will cover the general model for the growth of nanoparticles as well as the basics of magnetic particle synthesis and its methods. The silica shell was touched in detail before and I will only cover the details of the synthesis. For the hydrogel I will discuss the details of a free radical emulsion polymerization and why we used each additive. The scope of this work only includes reactions in an aqueous medium to keep the particles as biocompatible as possible, therefore methods in organic media, although well established, will be touched only briefly.

### 2.5.1 Nanoparticle synthesis in general

Synthesizing nanoparticles is a special challenge when compared to the synthesis of bulk materials, because small variations in the product can have great influence on the properties of the product. Take for example the surface of particles: In bulk it does not play a role, but for nanoparticles, the surface is one of the main features of their properties. Because already small variations play a huge role, therefore the reproducibility is an issue that needs to be addressed.[38]

#### 2.5.1.1 LaMer

The model devised by LaMer is the default model when the growth of nanoparticles is described, since almost all reactions more or less follow this scheme.[104] The core graphic of the LaMer model is displayed in Figure 12. The model is divided into three phases, here labeled by the roman numerals. The three phases are divided into the monomer production stage (I), the nucleation stage (II), and the particle growth stage (III). The stages are mainly dependent on the concentration of the monomers, which is put on the y-axis. In the first stage monomers are produced, by reduction of iron salts in this case. As the reduction progresses, more and more monomer is formed until the saturation concentration is reached and crossed but no particles nucleate in phase I because the system is metastable. This means that the system is thermodynamically instable but kinetically stable. The thermodynamic instability is of course explained by crossing the saturation concentration, the kinetic stability on the other hand can be explained by the high surface energy of very small particles. This surface energy

needs to be balanced by the energy gained by crystallizing; the difference is an activation energy. The equation is shown here:

$$\Delta G = -\frac{4}{3}\pi r^3 |\Delta G_v| + 4\pi^2 \gamma \quad (16)$$

The first term is the energy gained when a monomer binds to a cluster or another monomer to form one and is therefore negative and lowers the Gibbs energy  $\Delta G$ . The second term is the opposite: the increase in free surface energy ( $\gamma$ ) when a particle is formed. The effective energy is plotted in Figure 12A in black. The plot shows that a critical radius  $r_c$  exists that needs to be overcome to favor the particle growth over dissolution.

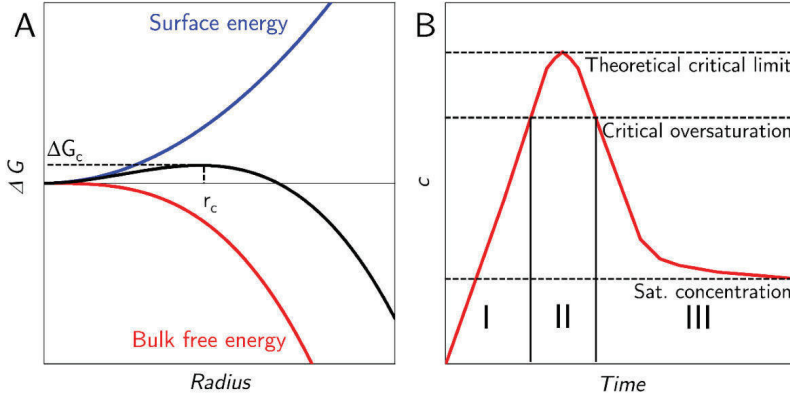


Figure 12: Schematic of the critical radius and LaMer model (A) The critical radius derived from the connection of surface and bulk free energy. (B) The LaMer model with the three phases of monomer saturation (I) nucleation (II) and particle growth (III).[104]

Because of the activation energy of the particle growth  $\Delta G_c$  the nucleation starts only when the system reaches a critical oversaturation. Here the system enters phase II of the particle growth, the nucleation stage. The monomers nucleate into clusters at a very rapid pace that is directly linked to their concentration. There is a theoretical critical limit where the concentration is so high that the nucleation speed reaches infinity, which means instant nucleation, an ideal state for particle growth. When the monomers nucleate, they are removed from the stock of the monomer concentration, so this concentration declines until

there is no longer a critical oversaturation and the nucleation stops. To reach a narrow size distribution the second phase needs to be kept as short as possible, so all clusters enter the third (growth) phase, at the same time. This is usually accomplished by rapidly increasing the monomer concentration and then terminating the monomer production. This can be achieved for example by injection of monomer into very hot solvent.[105] Here, cold monomer is injected into the solvent which is at 300 °C, which leads to rapid nucleation that is quickly stopped due to the temperature drop. This way the concentration of monomers is kept at a high level. A less radical approach at lower temperatures in aqueous solvent is the dropwise addition of a precursor solution to a 90 °C aqueous solution, which results in a slightly broader distribution due to the smaller difference in temperatures.[44]

The particle size distribution gets only monodisperse when the particles nucleate homogeneously, meaning when only one species of monomer comes together to form a cluster. When there is more than one species or a secondary material to nucleate upon, the nucleation is called heterogeneous nucleation. Heterogeneous nucleation follows a different kinetic that is again dependent on the surface energy of the secondary material. A third type of nucleation is the secondary nucleation. This occurs for example in a seeded growth reaction where seeds are added that monomers grow onto. When a monodisperse product is desired, as is usually the case, only one type of nucleation should be allowed and the others suppressed as good as possible, by working with high purity reagents and under carefully controlled conditions.

During the third stage, the nuclei grow by different mechanisms. The first and often desired process is the attachment of monomer, here the reaction speed is solely diffusion controlled and the final particle size is quite narrow. The second process is the aggregation of nuclei to form bigger particles. This process is usually suppressed by stabilizing the growing nuclei against aggregation because it would lead to a broadening of the size distribution and possibly to crystal defects at the aggregation site. The third process involved in the particle growth is Ostwald ripening. Here small particles dissolve again into monomers to be added to big particles. This leads again to a broadening of the size distribution and to a decrease in particle concentration.[105] The driving force of Ostwald ripening is the different solubility of large particles compared to small particles.

As with the different nucleation processes, it is beneficial to the size distribution to suppress all growth processes apart from the diffusion-controlled addition of monomer. This is usually achieved by adding surfactants to the reaction, which prevent aggregation and improve the solubility of large particles.

In another theory, the growth of nanoparticles is entirely dependent on their colloidal stability.[106] Here it is argued that even very small clusters of just a few atoms are already stable at most synthesis temperatures ( $<200\text{ }^{\circ}\text{C}$ ) in water, so the critical radius is almost at the metal atom radius. But at the same time the solubility of metal atoms in the aqueous solvent is almost zero, so the particles are not colloiddally stable. Then the growth happens solely by aggregation of small clusters and monomers instead of only monomer diffusion and attachment. The particles grow until they reach a size that is colloiddally stable. The essence of this model is that contrary to other models the particles do not have to bridge an energy barrier before they can start to grow, but rather always grow until they are colloiddally stable and cannot cross the aggregation energy barrier.

### 2.5.1.2 Hydrothermal synthesis

The term hydrothermal synthesis unites all procedures that use high-temperature and aqueous solutions at high vapor pressures to crystallize substances. Originally meant only for crystal synthesis, the term is now used for all reactions taking place in a pressurized reactor with an aqueous solvent. The method in general depends on the solubility of minerals in hot water under high pressure. The synthesis is done in a sealed autoclave where all educts are supplied with water. The method is promising for the synthesis of magnetic structures since it allows for high precision in the crystal structure which directly influences the magnetic properties. The advantages of hydrothermal reactions are described in the literature as high product purity and homogeneity, having narrow particle size distributions, lower energy requirements, fast reaction times among other things relevant to hardly soluble species.[107,108] The advantages are based on the ability of the system to heat the solvent past its boiling point, while keeping it liquid by adding pressure. The major drawback of the hydrothermal technique is that the reaction happens inside an opaque reactor and the conditions inside the reactor are hard to observe during the reaction. There are methods for sample extraction under pressure and even reactors made from glass, but these methods still do not provide the same results as sample extraction during a conventional reaction. Due to this, most hydrothermal reactions still require a time intensive trial and error process. The possibility to pressurize the reactor with an inert gas is also helpful when synthesizing particles sensitive to air oxidation like magnetite. Due to the good control over the synthesis conditions the reactions are easily scalable to other reactor volumes.

The combined advantages of the hydrothermal method made this the preferred method for nanoparticle crystallization for this work and for many coming after this.

#### 2.5.1.3 How to achieve anisotropy? Intrinsic or extrinsic pathways

Apart from the size of nanoparticles and their colloidal stability, the most important aspect is the final shape of the product. As explained in the magnetism section the shape of a magnetic particle gives rise to its own anisotropy and thus influences the magnetic properties significantly (Section 2.1.2.7).

Some iron oxide phases will always prefer to form anisotropic particles, like goethite for example. For these iron oxides, harsh conditions need to be applied to form anything that is not anisotropic.[109] The reason for this lies in their crystal lattice and the connected growth process, where addition of building blocks is only possible on distinct crystal faces, like for example the growth in the (020) direction for goethite.[110]

Other iron oxides like magnetite have a cubic symmetry in their crystal lattice, so growth happens on more than one crystal face, leading to more isotropic particles. Achieving anisotropy in this case requires the use of surfactants or soft templates to limit the growth along some crystal faces while leaving others open for growth. In the following paragraph I will give a few examples for different surfactants.

An example for an amphiphilic surfactant is CTAB. Although not very well soluble in water due to its long nonpolar tail, it is often used as a surfactant, because the cationic ammonium group binds well to nanoparticles and the particles are easy to transfer into other solvents after the synthesis.[27,106,111] It was applied with great success to the synthesis of hematite and akaganeite particles and influenced their form from cubes to rods.[27] In this work it was shown that CTAB hinders growth by attaching to growing facets, but a specific binding face was not determined.

Different sources report the use of PEG as a soft template to direct the structure of magnetite towards large nanorods or wires.[21,23,25,102,112] Here, different molecular weights of PEG were used because of their long chain structures that adhere to preferred facets. It is assumed that PEG binds to the iron oxide particles by chemical interactions between the surface of the particles and the oxygen atoms of PEG.[26] It was described that PEG mainly passivated the side surfaces of the particle while leaving the ends largely uncovered. After that, the free ends can grow to form nanowires. It was claimed that longer chain



lengths also lead to longer particles and different groups report the use of PEG as a soft template to direct the structure of magnetite towards large nanorods or wires.[21,23,25,102,112] Here, different molecular weights of PEG were used because of their long chain structures that adhere to preferred facets. It is assumed that PEG binds to the iron oxide particles by chemical interactions between the surface of the particles and the oxygen atoms of PEG.[26]

Dopamine is also reported as a good surfactant for iron oxide because its catechol group spaces the hydroxide groups similarly to the  $\text{Fe(III)}^+$  sites on a growing iron oxide face, resulting in a strong affinity of the group to iron.[28,29,113]

Apart from using surfactants there is also a number of articles reporting the synthesis of anisotropic magnetite particles by synthesis in a magnetic field.[24,32,33,35,114] Mostly the synthesis is done while a permanent magnet is put into close vicinity of the reaction vessel, so the particles grow along the field lines. The growth is reported to happen by guided aggregation. The reactions range from simple coprecipitations to reactions in a hydrothermal reactor and do not involve surfactants, so guided growth is achieved by the magnetic field alone.

A major obstacle of using this reaction pathway is the limited thermal stability of most permanent magnets. The standard permanent magnet for example is made of a neodymium, iron, boron alloy ( $\text{Nd}_2\text{Fe}_{14}\text{B}$ ) and loses parts of its magnetization at temperatures as low as 80 °C, which makes it unsuitable for hydrothermal applications.

### 2.5.2 Aqueous reactions in batch

In most reactions that happen in aqueous solution in one reaction step iron salts were mixed with a strong base like NaOH at room temperature, followed by the reaction at elevated temperature with or without a hydrothermal reactor.[30,115–117]

The iron salts are often Iron(II) and Iron(III) chlorides, but sulfates and nitrates are also used.[116,117] The most important part about these iron salts is the stoichiometry that needs to match the stoichiometry of the product. In the case of magnetite, the ratio of iron(II) to iron(III) needs to be 1:2, often with an excess of the iron(III) species. Although the stoichiometry is important, in many protocols only one iron salt is used and then partly oxidized/reduced by the applied base to reach the required ratio.

The probably most employed reaction, most likely because it is also the simplest one, is the coprecipitation method.[11,118,119] Here a simple acidic solution of iron(II) and iron(III) is taken and a strong base is added so the particles, which form the iron oxide, precipitate in aqueous solution, ending their growth process. The particles produced by this method range in size from 5 nm up to about 100 nm.[120] The properties of these particles are strongly influenced by the reaction conditions. To give some examples: the ratio of the reactants, the speed of alkali addition or the speed of the iron addition vice versa, the pH during particle growth, the temperature and the reaction time all influence the properties and sometimes even the phase of the final product.[118,121,122]

The method of oxidative aging was introduced by Sugimoto and Matijević[123] and later followed by Vereda *et al.*[117] At first an amorphous ferric hydroxide phase is precipitated and then aged at 90 °C in the presence of nitrate ions. Again, the properties of the final product are strongly dependent on the synthesis conditions, like pH and anion/cation choices. By this method it is possible to synthesize small, spherical, monodisperse particles with a diameter of around 20 nm but also large micrometer sized spheres and cubes around 50 nm.

There is the hydrothermal method, which was discussed in the previous chapter (2.5.1.2). While in this method the reactants are mixed before the addition to the reactor and start to react, the main reaction happens at high temperatures, so it is still considered a batch reaction.

Similar to the hydrothermal method is the synthesis in a microwave oven.[124,125] The method offers the advantage of fast volumetric heating and very fast reaction rates. The solvent is directly heated by microwaves which induce vibrations in the water molecules themselves to heat the solution.

### 2.5.3 Reaction with a precursor

Commonly the word precursor refers to any educts used in synthesis, but in this chapter, I will only treat reactions where the precursor consists of particles that are transformed into iron oxide particles. Since most people prefer a one-pot synthesis over a two-step process, the literature for precursor-based syntheses is not as extensive as for batch processes. The process of transforming one iron oxide into another is nevertheless very common and happens during many iron oxide syntheses.[118] The matter now is only to isolate the precursor iron oxide phase and to quantitatively transform it to the target phase. The precursor of choice here is akaganeite, because its crystal structure and properties make the further

transformation rather easy.[15,28,118] It was shown that akaganeite is consumed continuously during its transformation so it is safe to assume that the growth process happens by dissolution and recrystallization.[126] As mentioned in the section about akaganeite, the chloride ions can easily be exchanged for hydroxide ions, which leads to easier dissolution of akaganeite into iron hydroxides. These iron hydroxides can be reduced or oxidized by adjusting the pH and by the choice of reductants/oxidants, allowing excess to the different iron oxide phases.

This reaction pathway allows for good control over the size and properties of the final iron oxide product but is also heavily reliant of the quality of the supplied precursor. To ensure the same conditions for all growing particles the precursor particles should be monodisperse and phase pure. Surfactants present during the precursor synthesis need to be considered and eventually removed before the precursors can be further treated. The most straightforward process for impurity removal would be simple dialysis against purified water, but since the tunnel structure of akaganeite is volatile towards hydroxide ions, this approach was later abandoned. To keep the precursor-based reactions reproducible it was of great importance to use the same precursor batch, at least for comparable reactions.

#### 2.5.4 PNIPAM-Gel synthesis

The synthesis of covalently bound PNIPAM gels was done according to an approach by Karg *et al.*[41] Here, silica particles are combined with a thermoresponsive matrix with the help of TPM as a coupling agent. The first step is the synthesis of the silica particles, in our case we created silica coated nanoparticles. The surface of these particles is then treated with TPM, turning their surface hydrophobic, but also providing an anchor group for the PNIPAM polymerization in the next step. The next step is a free radical emulsion polymerization. The radical starter is the widely used thermal initiator KPS. KPS serves the double purpose of initiating the reaction and stabilizing the produced micro/macrogel by depositing strongly charged sulfate anions. Upon being exposed to heat KPS splits into two sulfate radical anions, which then abstracts a proton from the acrylamide group of a NIPAM monomer and creates a radical that starts the polymerization. The temperature required to split KPS is around 70-100 °C but it can be reduced to 60 °C by adding a redox system to the synthesis, in this case sodium sulfite and ammonium iron nitrate.[127,128] As soon as PNIPAM reaches a sufficient chain length of just a few monomers it becomes insoluble in water at the reaction temperature and forms micelles, but due to the

sulfate groups left from the initiator it does not precipitate. These micelles are additionally stabilized using SDS as an emulsifier. The reaction proceeds in the micelles until all monomer is used up or until all chains inside of a micelle are terminated. Termination can happen by two growing chains meeting, by the meeting of a growing chain with a sulfate radical or by disproportionation.

Apart from NIPAM, BIS is added into the system to crosslink the growing PNIPAM chains to form a three-dimensional network. This leads to the formation of a microgel. When the reaction is almost finished, we add AA into the system to provide an outer amine function to the microgel beads. This amine function allows us further crosslinking at a later stage by adding GA. When GA is added the microgel beads get crosslinked together to form a single big network, which is then called a macrogel (see section 2.3.1).[129]

In the loosely bound system the synthesis is carried out after a protocol derived from the dissertation of Annemarie Nack.[42] NIPAM and GA are mixed together with SDS at 80 °C to directly form a macrogel. The reaction is very similar to the covalently bound system, but in this case instead of crosslinking primary amine groups by glutaraldehyde and forming an imide bond, a network is formed by crosslinking the secondary amine groups and forming amides. The imide bond is permanently in an equilibrium state, where it can reopen in reaction with water and temperature and form a new imide bond in another place. The amide bond is more stable and forms a permanent network.

Using this method, the nanoparticles are added later, simply by mixing them into the system and relying on physical adsorption to bind the particles to the gel.

### 3 Characterization methods

#### 3.1.1 TEM

To characterize the shape of the synthesized particles we used a combination of scattering and imaging techniques. Since the important features of our samples lie in the range between  $\sim 5$  and  $\sim 200$  nm, we chose the imaging technique of transmission electron microscopy (TEM). The imaging technique is based on a focused electron beam that is accelerated and focused on a thin sample. The wavelength of electrons and thus their maximum resolution is based on their velocity and thus on the acceleration that the TEM can provide. Starting from the top of a typical TEM the electrons are generated by the electron source, typically a thermic emitter, in our case a  $\text{LaB}_6$  crystal, that is heated to about 303 K and coupled with a Wehnelt cylinder. The crystal emits electrons that are accelerated by the anode with an acceleration voltage of 200 – 300 kV (in our case 120 keV on a Thermo Fisher Scientific Tecnai® G2 spirit twin machine). On top of the anode is the Wehnelt cylinder which is biased with a negative voltage relative to the emitter. This creates a repulsive electrostatic field which allows only electrons from the crystal tip to be emitted and functions to focus the emitted electrons.

Once the electrons reach their final voltage, and thus speed, the electron beam is condensed and focused by the condenser lens system together with the objective lenses (Figure 13). The electron beam should be parallel when it hits the sample, so no phase information is lost. The electrons then interact with the sample which provides the information later visible in the image. When the electrons hit an atom core they get scattered or absorbed, when they do not, they get transmitted. There are different ways contrast is created in a TEM image. There is mass thickness contrast and material contrast. The first is created because of the differences in the thickness of the material, so less electrons get transmitted and the second is present because of the different sizes of the atom cores. Heavier atoms give more contrast, because they scatter the electrons more strongly. The third kind of contrast is created by diffraction. Here the electrons undergo Bragg scattering, where the electrons are scattered on the crystal lattice and undergo coherent or incoherent scattering. There is also phase contrast, where the change in phase upon interaction with the sample is measured, but this can only be utilized in high resolution (HR)-TEM, so it will not be discussed here.

The apertures in the beam path are used to block unwanted electrons, for example electrons that are far from the optical axis. Apart from that they control the X-ray generation or improve the vacuum performance. The vacuum performance is especially important, because the whole TEM needs to be under high vacuum to prevent the electrons from scattering on air molecules. The condenser aperture is located directly above the sample and is used to avoid illumination beside the observed area. The objective aperture can be used to increase the contrast of the image while sacrificing intensity.

After the electrons interacted with the sample there is a set of further lenses and apertures that enhance the image until structures of a few nanometers are visible in good resolution with the naked eye on a fluorescence screen.

If instead of the image plane the electron beam is focused on the back focal plane of the microscope a diffraction pattern is created. This happens because the electrons are diffracted on the crystal lattice and this produces a pattern of spots, for single crystalline samples, or rings, for polycrystals. The position of the image features is dependent on the lattice spacing after Bragg's equation and on the orientation of the sample in the beam. This gives information about the crystal lattice of the specimen in focus. By using a selected area aperture even single particles can be selected for diffraction. This is mostly employed when there are different particle species in one sample.

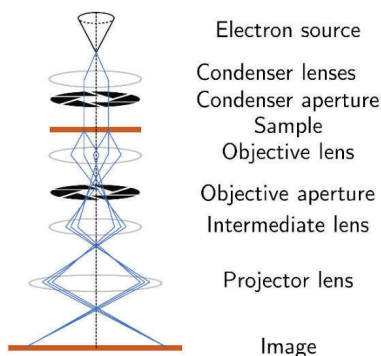


Figure 13: Schematic of a TEM in bright field image mode. The blue lines represent the illumination path, none of the mentioned parts is displayed in scale.

In some TEM models it is also possible to obtain a 3D image of the sample by tilting the sample holder in small steps and taking images of this tilt-series. The result is called TEM-tomography and was utilized to analyze the position of particles inside of a gel-matrix in this work.

For room temperature sample preparation prior to a TEM measurement we used copper 200 mesh grids, which were coated in house by a carbon film through physical vapor deposition. The coated grid was placed into a tweezer, so the grid was not in contact to any surface. Then the sample solution was diluted until only a trace of color is visible and  $\sim 5 \mu\text{L}$  of the solution were dropped onto the grid by an a single-channel mechanical pipette. The sample grid was protected by a petri dish from acquiring dust and dried for about 15 minutes.

For hydrogel samples it was important that the conditions in the TEM were as close to the conditions in a liquid sample as possible. Therefore, it was necessary to perform cryo-TEM measurements. The sample was vitrified in a Thermo Fisher Scientific Vitrobot<sup>®</sup> using liquid ethane at about 83 K. Through vitrification the water molecules have no time to crystallize upon freezing and form an amorphous solid that does not damage the sample.[130] After vitrification the sample is kept in liquid nitrogen until it is transferred into the cryo-TEM. The transfer is another sensible process, because even very short exposure to air moisture can lead to the formation of transfer ice crystals on the grid.

The particle size was evaluated by measuring the length and width of 100 particles in each sample using the freeware software ImageJ.[131]

### 3.1.2 XRD

X-ray diffraction (XRD) is a powerful tool to determine the crystal structure of a material. The sample is radiated by X-rays from different incident angles so the whole crystal space can be illuminated. The incident angle is connected to the lattice spacing of the sample by Bragg's equation:

$$n\lambda = 2d\sin(\theta) \tag{17}$$

Here  $n$  is the diffraction order,  $\lambda$  is the incident wavelength of the X-ray (mostly  $1.54 \text{ \AA}$  for Cu- $\alpha$  sources),  $d$  is the lattice spacing and  $\theta$  is the angle between the incident beam and the normal of the crystal plane. The angle is multiplied by two because incident and exiting beam are regarded here. All angles that do not fit Bragg's law are suppressed by deconstructive interference and do not show in the

diffraction pattern. An exception is the diffraction on very small particles (<200 nm), here the number of crystal planes is not large enough to fully suppress signals not exactly fitting Bragg's law. The result is a broadening of the signal and this can be interpreted to learn the size of the crystal planes inside the sample. The relating equation is the Scherrer-equation:

$$d = \frac{K\lambda}{FWHM_{hkl}\cos(\theta)} \quad (18)$$

Here  $d$  is the crystallite size,  $K$  is the crystallite shape factor (for spherical samples 1),  $FWHM_{hkl}$  is the full width at the half maximum of the regarded peak in radians and  $\theta$  is the double incidence angle.[132]

With these methods, the space group and crystallite size of a material can be accurately determined.

X-ray diffraction was done on a Philips X'Pert PRO MPD machine. For the evaluation of the crystal phases present, we used the software Highscore X'pert PRO by PanAnalytical. For sample preparation, after washing to neutral pH, ca. 100  $\mu$ L of the particle dispersion was deposited on a [511] single crystal silicon waver and dried in air.

### 3.1.3 VSM

To measure the magnetic properties of our samples a vibrating sample magnetometer (VSM) was used. For this method, the sample is tightly secured on a sample holder and vibrated inside of an outer magnetic field. The magnetic field of the sample interacts with the applied field and induces a current that can be measured by pick-up coils that are placed around the sample. The nonmagnetic sample holder is connected to a mechanical vibrator which guarantees a steady vibration. The vibrator is in turn equipped with a reference magnet that is not in an outer magnetic field (apart from earth's magnetic field) and vibrates in the same frequency as the sample. The reference magnet is inside of another set of pick-up coils so the signal from the agitation can be kept at a constant level. The sample pick-up coils are connected to a lock-in amplifier that only detects signals at the agitation frequency so the whole system is very stable against outside influence. The measurement can only give meaningful values if it is calibrated with a sample of a known magnetization, mostly nickel is used, because it reaches saturation at small field strengths and is very stable over a long period of time.[133]



The sample was prepared mostly as a powder. About 10 mg were carefully transferred into a quartz cup sample holder, which was fixed securely on a glass holder by using Teflon<sup>®</sup> tape. The glass holder can then be inserted into the matching sample holder on the VSM. For liquid samples like hydrogels about 80  $\mu\text{L}$  of the sample was put into an Ultem<sup>®</sup> cup. Ultem<sup>®</sup> is an amorphous polyimide. The cup was sealed and glued to a sample holder with a stamp connection by double-sided tape. For the measurement in water the diamagnetism of water needs to be compensated. Therefore, a reference measurement gets later subtracted from the measured curve.

The measurements we carried out on an EZ-9 VSM from MicroSense. The samples were magnetized over the full range between positive and negative 2.5 T. The field strength step could be adjusted at will. 100 mT were chosen for the rough measurement in the saturation region, while 50 mT and finally 10 mT steps were chosen around zero field to see a possible hysteresis.

### 3.1.4 DLS

Dynamic light scattering (DLS) was mainly used to determine the hydrodynamic radius of microgel beads and sometimes to determine the size of particles in colloidal suspensions. This is done by illuminating the sample with a monochromatic light source, typically a laser. The particles interact with this electromagnetic wave and become dipole oscillators that emit their own electromagnetic wave. When the particles are bigger than  $1/20$  of the incident light, so with a standard source of a 532 nm laser, bigger than 26 nm, they possess more than one dipole and the emitted waves have a phase difference, thus the emitted waves interfere with each other. The interference is dependent on the angle at which the detector measures, so by measuring at different angles one can gain structural information (for example the form factor or the radius of gyration) of the sample. The measurement of the averaged intensity of each angle to obtain a mean intensity at different angles is called static light scattering.[134]

In solution, particles are generally able to move around by diffusion. If the particles now move while illuminated by the laser, the interference pattern measured at a specific angle will change in dependence on the speed of diffusion. The speed of diffusion, or diffusion coefficient  $D$ , is in turn connected to the size of spherical particles by the Stokes-Einstein-Equation:

$$D = \frac{k_{\text{B}}T}{f} = \frac{k_{\text{B}}T}{6\pi\eta R_{\text{H}}} \quad (19)$$

Here  $k_B T$  thermal energy,  $f$  is a term for the friction between particles and medium  $\eta$  is the dynamic viscosity of the medium and  $R_H$  is the radius of the particle together with its hydration shell, the hydrodynamic radius. The measurement of  $D$  generally happens by evaluating correlation functions. To obtain the correlation function, the intensity at a given time is measured and multiplied by the intensity after a time interval  $\tau$  by a hardware correlator. This way a normalized scattered intensity autocorrelation function ( $g_2$ ) can be obtained:

$$g_2(q, \tau) = \frac{\langle I(q, t) I(q, t + \tau) \rangle}{\langle I(q, t)^2 \rangle} \quad (20)$$

with  $q$  as the scattering vector:

$$q = \frac{4\pi n_0}{\lambda} \sin\left(\frac{\theta}{2}\right) \quad (21)$$

Here  $\lambda$  is the laser wavelength,  $n_0$  is the refractive index of the sample and  $\theta$  is the angle of the detector relative to the sample. It should also be mentioned that here the field auto correlation function  $g_1$  is connected to  $g_2$  by the Siegert relation:

$$g_2(q, \tau) = 1 + g_1(q, \tau)^2 \quad (22)$$

$g_1$  is usually plotted semi logarithmically to ease the data analysis. This way a monodisperse sample has a single decay while a bimodal sample has two decays and so on. If the particles are not perfectly monodisperse (real samples never are)  $g_1$  is fitted by a cumulant method to obtain  $D$  and a value for the polydispersity. For the cumulant method,  $g_1$  is expanded in a series expansion:

$$\ln(g_1(q, \tau)) = -\kappa_1 \tau + \frac{1}{2!} \kappa_2 \tau^2 \dots \quad (23)$$

Here  $\kappa_1 = \langle D \rangle q^2$  contains the average diffusion coefficient  $\langle D \rangle$  and  $\kappa_2 = (\langle D^2 \rangle - \langle D \rangle^2) q^4$  provides a measure for the polydispersity. This way an average size distribution of the particles in solution can be obtained from DLS.

It should also be mentioned that  $R_H$  can only be determined if the sample is very dilute, because when the particles interact, this changes their mobility and thus the diffusion coefficient. In addition, multiple scattering leads to false results since a second scattering process decreases the correlation of the sample and thus shifts the measured hydrodynamic radius towards lower values.

### 3.1.5 Rheology

Rheology, or the flowing properties of materials, means looking at the answer of a system to a localized stress and then inferring its molecular makeup. For example, we put a fixed deformation to a hydrogel and by watching how fast or slow it reacts we draw conclusions on the strength of the crosslinks inside the material. The field of rheology, or dynamic mechanical analysis (DMA), is incredibly vast so only a small fraction of it will be covered here to understand the types of experiments we did. To grasp what happens in these tests we need to clarify some basic variables and concepts first. An often-used model is the two-plates model (Figure 14). Here the upper plate moves and shears the liquid with a speed  $v$ . The following equations only hold when there is no-slip on the plates and the flow is laminar.

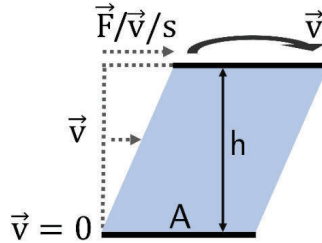


Figure 14: Schematic of a rheology setup; liquid sample between two plates. The different flowing speeds of the liquid are indicated by the dotted arrows, the curved arrow was added to indicate that the movement is caused by rotation of the upper plate, while the lower plate stays immobile.

The upper plate exerts a shear stress  $\tau$  on the sample whose magnitude depends on the area of the plate  $A$  and the force of the movement  $F$ :

$$\tau = \frac{F}{A} \quad (24)$$

To describe the periodicity of the experiment another common term is the shear rate, which is the change in stirring speed over time (indicated by dot notation).

$$\dot{\gamma} = \frac{v}{h} \quad (25)$$

The answer in shear stress of a system to an applied shear rate is its viscosity  $\eta$ .

$$\eta = \frac{\tau}{\dot{\gamma}} \quad (26)$$

Another interesting parameter is the deformation of the material upon application of a shear stress, the shear strain.

$$\gamma = \frac{s}{h} \quad (27)$$

There is also the shear modulus  $G$ . Also called rigidity modulus this material specific value gives information about the resistance of the material to deformation.  $G$  can only be applied when the measurement was done under stationary conditions so  $\tau$  as well as  $\dot{\gamma}$  are constant.

$$G = \frac{\tau}{\gamma} \quad (28)$$

Since we are dealing with viscoelastic composite materials, they behave sometimes liquid-like and sometimes solid-like. In this case the shear modulus is subject to changes over time and we must use the complex shear modulus  $G^*$ . This complex size can be split in its real and imaginary part so that:

$$G^* = G' + iG'' \quad (29)$$

In this equation  $G'$  is the storage modulus and  $G''$  is the loss modulus. The storage modulus shows the deformation energy stored in a system, so when this modulus is high the system can easily revert into its initial state. This is used to describe the elastic or solid-like behavior of a system. The loss modulus  $G''$  describes the energy lost upon deformation, so when this modulus is high the system will show liquid-like behavior and will act upon deformation by losing its initial state. The energy is lost by the dissipation of heat either in the sample or in its environment by friction. This is also called the viscous behavior of a system and is typically found in liquids. Since we can display complex numbers also in a vector system, there exists an angle between the vectors and the relationship of storage and loss modulus is the loss factor:

$$\tan \delta = \frac{G''}{G'} \quad (30)$$

The size of the loss factor gives information about both the sol/gel state of a sample. If its smaller than 1 the sample is solid-like (gel), if its larger than 1 the

sample is liquid like (sol), if it is exactly 1 the sample is in a transition state between the two states.[135]

The experiments involved oscillatory shear; more precisely, we performed amplitude- and frequency sweeps. Oscillatory measurements consist mostly of these two measuring modes. The start is always an amplitude sweep, which means the amplitude of deformation is varied, while the frequency of deformation is kept constant. This is done to determine the region of deformation in which the sample shows a linear response to the deformation, this is called the linear viscoelastic region (LVER). When the deformation is increased above this region the sample reacts nonlinear, which means the sample sustains damage and is changed irreversibly. When the “safe” region is determined a deformation without sample damage is chosen and a frequency sweep is conducted at this deformation. Both tests alone can already give information about the sample, for example by the limit of the LVER or by the absolute values of the moduli. The frequency sweep can also be used to determine the entanglement molecular weight  $M_e$ . [136] Here the values of  $G''$  and  $G'$  are compared to determine the minimum of  $\tan\delta$ . This method is called the MIN-Method. At this point the sample is in a local equilibrium and the value for  $G'$ , called  $G_N^0$ , can be used to determine  $M_e$  by using the following equation:

$$G_N^0 = \frac{4}{5} \frac{\rho RT}{M_e} \quad (31)$$

In this equation  $\rho$ ,  $R$  and  $T$  have their usual meaning.  $M_e$  is defined as the average molecular weight between two entanglement points and is used as a measure for the density of a polymer network.

For the measurements, we used an Anton Paar rotation rheometer MCR 502. This model is equipped with an air bearing measuring device, making it possible to change the measuring tools as required. We used a plate-plate geometry, once in a small angle light scattering (SALS) configuration with a PP43 GL/HT measuring tool, but we also used the same geometry without SALS with a PP25 measuring tool. There is also the magnetic measuring tool PP20/MRD/TI which can apply a magnetic field perpendicular to the sample plane. The tool is also in plate/plate geometry and the maximum field strength is reported at 1 T.[137]

### 3.1.6 SAXS\XPCS

Small Angle X-ray Scattering (SAXS) is a technique that uses hard X-rays to obtain information about nanoscale density variations in all kinds of materials. It has many applications, from determining size distributions to pore sizes in membranes and we used the technique to measure the orientation of an anisotropic sample in a magnetic field.

The technique is based on the elastic scattering of hard X-rays by the sample. The X-rays pass through the sample, get scattered on local electron density variations and get recorded at very small angles in the range of  $0.1 - 10^\circ$ . So, the resolution is in the range of 1 to 100 nm.

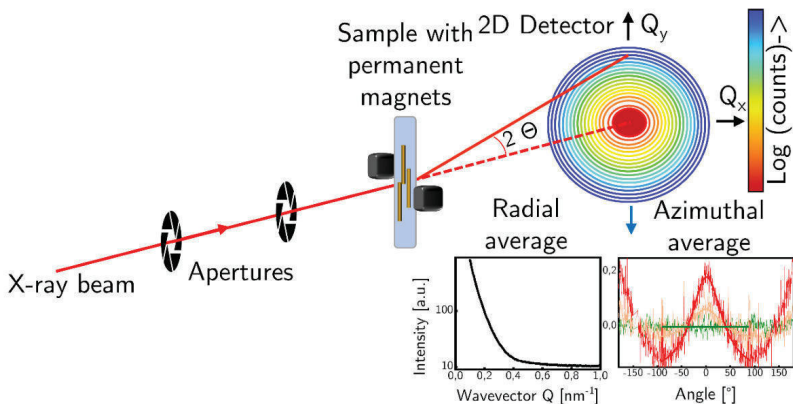


Figure 15: Schematic of a SAXS experiment. The beam is focused and positioned by the source and the apertures before it hits the sample. Upon hitting the sample some X-Rays are scattered and then hit the detector behind the sample. The detector counts the arriving X-Rays and creates a 2D image. This 2D image can then be interpreted by creating a radial average and evaluating the intensity against the wavevector or by creating an azimuthal average to compare the intensity with the angle.

In a typical experiment the X-ray beam is collimated by one or more apertures to be focused on the sample and to generate a small spot. After hitting the sample, the X-rays are scattered and detected by a 2D position sensitive detector. Through the interference of different scattering centers a scattering pattern is created that can be analyzed to gain information about the size and distribution of the particles (Figure 15). Usually, the particles in a sample have a random orientation, which

leads to a considerable data loss in the scattering information.[138] This can be somewhat mitigated by combining SAXS with an imaging method like TEM to refine the results and to start from a good base assumption. The usual procedure to gain information from the scattering curve is to assume a model and to try to fit the intensity function into this model. If the general dimensions of the particles are already known, choosing the model is much easier.

The obtained intensity curve is a superposition of a formfactor and a structure factor. The formfactor is dependent on the shape of the particles in the sample, each shape produces specific minima in the formfactor that can be fitted to gain information about the shape parameters. For example, for a cylinder the radius and the length of the cylinder can be obtained. Problems arise when the particles are not perfectly monodisperse in size and shape. This causes a smearing of the minima sometimes even obscuring them. For moderate values of polydispersity this is also a value that can be gained from a good fit.

Overlaid on the form factor is the structure factor. It is dependent on the interactions between the particles. It is sensitive to the distribution and can be fitted to gain the average interparticle distance. The structure factor is mainly of interest in highly ordered systems.

In our experiments we were mainly interested in the orientation of the particles. Instead of obtaining the radially averaged intensity, we integrated the intensity for each angle in the 2D Image and obtained the azimuthal average intensity distribution in a circle around the beam stop.

Since our particles reorient in a magnetic field, we applied a field by positioning two permanent magnets on remotely controlled sleds on opposing sides of the sample to set the field by changing the distance between the magnets. This allowed us to obtain the intensity distribution in dependence on the field strength. To analyze the intensity distribution we used the Herman orientation function:[139]

$$f_H = \frac{1}{2}(3\cos^2\theta - 1) \quad (32)$$

Here  $\theta$  is the angle between the applied field and the long particle axis. The function reaches its maximum of  $f_H=1$  when the long axis is parallel to the field and  $f_H = -0.5$  when the long axis lies perpendicular. At  $f_H = 0$  there is no orientation. We look at a special case of this equation in our case because our particle dimensions lie in parts outside of the available  $q$ -range. We can only see the short axis of our particles; the long axis is outside of the range. We solved

this by taking the position of the minimum of the peak instead of the maximum, by adding  $90^\circ$  to the position of the maximum.

While SAXS generates a 2D image of a system integrated over a certain (but sometimes very small) timescale, it is also possible to measure the dynamics of a sample, but several conditions need to apply to the beam-setup. The X-ray source needs to be capable of producing a coherent beam, which is sufficient in intensity to allow the acquisition of a speckle pattern in a very short timeframe. A speckle pattern is visible on an X-ray detector when a disordered sample is illuminated by coherent light. Coherence means the X-ray waves arriving at the sample have the same energy and a constant phase correlation. The evaluation of the intensity fluctuations of a speckle pattern gives access to the dynamics of the sample volume that created the pattern, similar to what we already learned from DLS. The volume of the sample that is the origin of a speckle pattern is made up of one whole or partial coherence volume. The coherence volume is spanned by the longitudinal correlation length  $\xi_l$ , which is dependent on the energy distribution of the photons, so on the wavelength difference of the X-ray waves, and by the transversal correlation length  $\xi_t$ , which is related to the size of the X-ray source. In a beamline setup  $\xi_l$  is controlled by an undulator and a monochromator, while  $\xi_t$  is controlled by apertures in the beam path and by the distance of the sample from the source. Another important factor is the coherent flux  $F_c$ , which is dependent on the wavelength with  $\lambda^3$ , making a high coherent flux easier achievable at longer wavelengths.

The method is called X-ray photon correlation spectroscopy and with this it is possible to create a series of speckle patterns in a very short amount of time, making slow changes in the structure of a sample visible and quantifiable. To take images quickly a coherent x-ray beam with a high coherent flux is needed, which is provided at the high coherence beamline P10 at DESY. The actual time resolution is also dependent on the count rate of the detector, which needs to be on the same or a faster timescale than the dynamics that are to be observed. The spatial sensitivity for dynamic measurements is in the range of tens of nanometers while the temporal resolution goes from tens of microseconds to thousands of seconds.[140] The technique is relatively similar to DLS but with a different photon source. The usage of X-rays has several advantages: there are no complications due to multiple scattering, the possibility to measure optically opaque samples and for some applications surface or magnetic sensitivity. Similar to DLS, the measured series of interference patterns can again be described by a time correlation function like equation (20), allowing for similar fitting procedures.



If a 2D detector is used, the time correlation function can be evaluated for each pixel, so areas of interest can be evaluated in isolation to pinpoint interesting structures in the sample and their time evolution.

Another type of correlation function employed in XPCS is the two-time correlation function, which is used to examine “aging” dynamics outside of equilibrium:

$$C(Q, t_1, t_2) = \frac{I(Q, t_1)I(Q, t_2)}{\langle I(Q, t) \rangle^2}. \quad (33)$$

The correlation function deployed before for an equilibrium state depends only on the time lag  $\tau = t_1 - t_2$  and not on the individual times  $t_1$  and  $t_2$ , so it can be averaged. However, if the system is not in an equilibrium and the relaxation time is dependent on the time that has passed, the function is dependent on  $t_1$  and  $t_2$ . Using this function provides information about temporal heterogeneities and the non-equilibrium nature of a sample, like particle orientation in our case.

SAXS data at the university of hamburg were taken on an Incoatec X-ray source I $\mu$ S with Quazar Monet1 optics. The focal spot diameter was 700  $\mu$ m, the wavelength was 0.154 nm, detector distance was 1.6 m and the detector a Rayonix SX165 CCD-Detector. Samples were prepared as colloidal suspensions. Particle content was adjusted to 2.5 wt% (m/m) by centrifugation and addition of water. The magnetic field was established by two cubic permanent magnets mounted on two sleds that can be moved symmetrically by a shaft. The distance between the magnets determined the magnetic field strength and was reduced from 50 mm in 1 mm steps. The minimum field strength with this setup at 50 mm is 35 mT, the highest field strength employed in this work was 533 mT at distance of 4.5 mm between the magnets. Baseline images without a magnetic field were taken in a standard capillary setup. For each image two frames were taken, each with a measurement time of 300 seconds, so 10 minutes measurement time for each field strength.

The measurements at BESSY were done in the medium-hard X-ray regime at 8 keV. The images were captured on a PILATUS 1 M detector model with a pixel size of 172  $\mu$ m x 172  $\mu$ m. The distance of the detector to the sample was  $4527.3 \pm 0.5$  mm. The magnetic field provided four field strengths of 14, 47, 79 and 615 mT, that were realized by varying the distance between two permanent magnets. Images were taken with an integration time of 60 seconds.

XPCS measurements were done at the P10 coherence applications beamline at DESY. P10 employed an U29 undulator at the time of our measurement. The beamline operates in the medium-hard X-ray regime (5-20 keV), in our case 7 keV were used. The detector was an EIGER X4M detector with a pixel size of  $75\text{ }\mu\text{m} \times 75\text{ }\mu\text{m}$ . The further specifics of the P10 beamline can be found in the datasheet.[141] The magnetic sample environment was realized by using a coil with a pure iron core that realized field strengths of up to 90 mT.[142] In this case the magnetic field was applied horizontally compared to the x-ray beam. The setup could be exchanged for a permanent magnet setup, in which the field strength was adjusted to 155, 230, 470 and 555 mT (Figure 16). In this case the magnetic field was tilted about  $45^\circ$  from the horizontal direction.

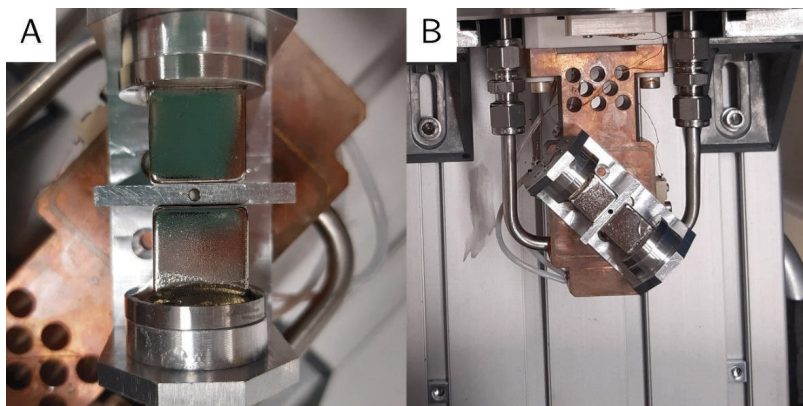


Figure 16: The permanent magnet setup at DESY. The displayed setup provides 555 mT in the sample area. The sample is mounted perpendicular to the magnets and the beam is guided through the hole visible between the magnets. (A) Closeup image. (B) The magnets mounted on the insert for the vacuum.

The different field strengths in the permanent magnet setup were realized by combining different sizes of permanent magnets, whose distance from the sample could be adjusted by washers. Temperature control was done by a Peltier element connected to the sample holder and by water cooling/heating controlled by a Lakeshore 340 thermostat that could be remotely controlled from outside the hutch.

## 4 Results and Discussion

### 4.1 Magnetic cores: Magnetite, the ferrimagnetic powerhouse

Magnetite displays the strongest magnetism of all iron oxides, which is of course mainly due to its well-defined crystal structure. The crystal structure is that of an inverse spinel, which has cubic symmetry. A cubic crystal symmetry also leads to particles in cubic shape when the reaction is carried out under only thermodynamically controlled conditions. This means that without surfactants or other guiding factors, magnetite particles will grow into cubes. We tried different synthetic approaches to overcome this thermodynamic barrier. Firstly, the application of different surfactants, polymeric and ionic, was tried in a batch reactor under varying synthesis conditions, from semi- batch to hydrothermal. Simultaneously we used a precursor-based synthesis approach with akaganeite as the precursor. This last reaction was also transferred into a microwave reactor with good results.

#### 4.1.1 Magnetite in batch reactions

As the most straightforward approach, synthesis protocols that happen in batch were tried first. These syntheses typically only consist of one or two iron salts, a strong base, sometimes also a weak base and a structure guiding agent.

The structure guiding agents were amphiphiles like CTAB, soft templates like PEG, steric stabilizers like PVP or charged stabilizers like citrate. We applied them to batch reactions with varying results. The most promising approach using a soft template involved PEG of various molecular weights, which was mostly used in a reaction where the iron salt was mixed up/dissolved together with thiosulfate (Figure 17).[21] The resulting particles are strongly polydisperse and show elongated morphologies as well as amorphous particles. While the control was rather poor, as evidenced by the polydispersity, this reaction yields many anisotropic particles. After drying the particles in air to prepare a powder for XRD the particles oxidized in large parts to hematite, which is then also evident in the XRD pattern. The initially black sample was retrieved in red color after exposure to air for several hours. We were unsuccessful in colloidally stabilizing

the particles, mostly due to large particles in the sample and agglomeration. Large magnetite particles possess a strong magnetic moment, leading to fast agglomeration if the particles are not immediately stable, which often makes stabilization of the whole sample impossible.

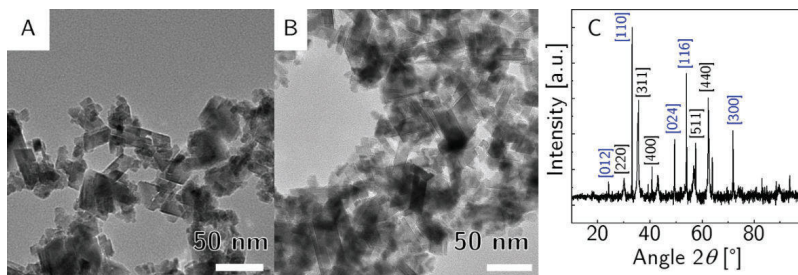


Figure 17: Magnetic particles created in a batch reaction, with ground up  $\text{FeSO}_4$ ,  $\text{Na}_2\text{S}_2\text{O}_3$  and treated with PEG as a growth directing agent. (A, B) Exemplary TEM images of the particles directly after the synthesis (C) XRD after the sample was dried in air. In black the reference peaks of magnetite, in blue of hematite. Note that most magnetite peaks also appear in the hematite diffractogram.

As mentioned above, PEG works as a soft template, it should form a matrix that the particles are enticed to grow into.[22] This seems to have worked for some particles in each sample but never yielded consistent morphologies across a whole ensemble. This is closely connected to the distribution of the PEG molecules in the reactor. Upon cooling the reactor to room temperature, we often noticed that the PEG was not fully dissolved but instead formed a gel like plug in the reactor. The plug was mostly colorless, the bulk of the particles was found in the surrounding solvent, indicating that little to no templating occurred. The most often used PEG 4000 is soluble in water up to 80 wt% (w/w) at 40 °C,[143] so solubility should not be a problem, given that the reactions were carried out at 150 °C and more than sufficient mixing time was applied. Since the ratio of PEG :  $\text{H}_2\text{O}$  was up to 1 : 1 for some experiments, the concentration was likely sufficient for templating to occur.[21] The problem seems to be lacking interaction between PEG and growing particles, there were no chemical or physical forces creating strong binding forces between the reactants. All the PEG variants used in this work were capped with hydroxyl groups, which do not facilitate strong interactions with growing magnetite particles. Without any surface altering

molecules, the surface of magnetite nanoparticles is very vulnerable to oxidation, explaining the mixed phases observed in the XRD.

Surfactants with a different form of interaction are for example CTAB, using a charged ammonium group for binding,  $\text{NaH}_2\text{PO}_4$  using a phosphate group, or citrate using one or more of its carboxylic functional groups. All of these were tested for their growth guiding ability. Citrate's two binding acid groups work very well for the stabilization of nanoparticles, but we observed a tendency to grow into an isotropic, spherical form across all citrate treated particles (Figure 18A). Phosphate coated particles showed interesting morphologies but were not phase pure. Phosphate was shown to specifically attach to the  $(2\bar{1}\bar{4})$  sites of hematite because here the distance of Fe-Fe with 2.29 Å matches best with the O-O distance in the  $\text{PO}_4^{3-}$  ions with 2.50 Å to restrict the growth of this crystal face and to produce rhombohedral particles instead of cubes.[61,66,144] A similar effect was observed in magnetite particles, where the (111) plane was favored, which is the main surface plane of magnetite at 40 nm particle size.[145] Our particles also show some shapes that could stem from growth restriction, but they also showed impurities of iron phosphate and other unwanted iron oxide phases (Figure 18B). CTAB did not show a preferred growing facet to attach to which led to cubic particles without elongation (Figure 18C). However, while they showed no anisotropic shape as desired, the CTAB coated particles showed a rather uniform morphology and a not too broad size distribution of  $18 \pm 6$  nm. The CTAB coated particles also showed a pure magnetite phase without impurities, so apart from not being highly anisotropic these particles meet all other desired requirements.

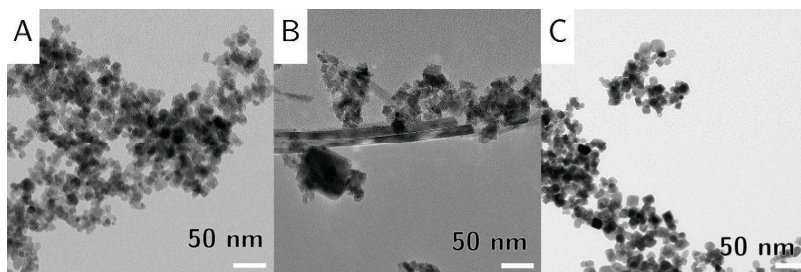


Figure 18: TEM images of citrate and phosphate coated particles. (A) Citrate particles with a tendency to grow spherical. (B) Phosphate coated particles with impurities of iron-phosphate and other iron oxides. (C) CTAB coated particles.

The hydrothermal reaction that employed CTAB as a surfactant was also among the first reactions using hydrazine as a weak base to accompany the strong base NaOH. Hydrazine proved to be almost a guarantor for a stable magnetite phase over the course of this work and was used in most of the following reactions.

Batch reactions were abandoned after the initial trials in favor of precursor-based reactions, because the precursor-based reactions were more reliable and yielded shapes with a higher degree of anisotropy.

A noteworthy different approach that we followed was first done by Matijević *et al.*[146] and later improved by Vereda *et al.*[147] Here, an  $\text{Fe}(\text{OH})_2$  Gel created from  $\text{FeSO}_4$  is partly oxidized by  $\text{KNO}_3$  and subsequently reduced to magnetite. This approach yields large octahedral magnetite particles with quite narrow size distribution. The particles are hydrophilic without adding any surface altering agents. The synthesis was first replicated in our lab, without making big adjustments (Figure 19A).

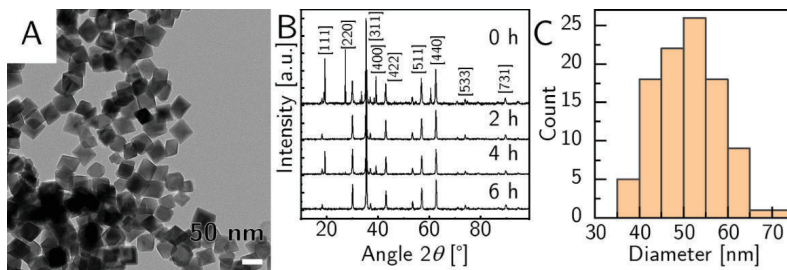


Figure 19: Magnetite octahedra made by oxidative aging of  $\text{Fe}(\text{OH})_2$  with  $\text{HNO}_3$ . (A) TEM image of the particles after 2.5 hours reaction time. (B) XRD taken in 2-hour time intervals, the magnetite phase is almost immediately present. All peak-assignments are taken from the hkl-indexes of magnetite JCPDS PDF-Nr. 01-075-1609. (C) Size distribution histogram.

We did a study of the particle formation by TEM and XRD to learn more about the formation process. Already as early as half an hour after the start of the reaction we found particles that were near their final size of about 60 nm. With the expected exception of a sample taken at the reaction start, all samples from 30 min onward up to 8 h were successfully precipitated by a magnet and showed the typical black color of magnetite. During the first four hours of the reaction we observed a narrowing of the size distribution, until after four hours the particle size was constant. After four hours we noticed small rod like

impurities in the TEM-images, but it could not be confirmed whether these contained also pure magnetite, as their fraction was too small. The phase determined by XRD showed a constant magnetite phase across the whole observed time frame. The reaction was very fast, and a stable magnetite phase was present from the beginning (Figure 19B). The particles showed a size distribution of  $51 \pm 7$  nm, (Figure 19C) close to the literature value where  $54 \pm 14$  nm were reported.[147] This particle size is at the limit to the one-domain range for magnetite particles ( $\sim 50$  nm).[148] To decrease the particle size we employed surfactants like citrate, which led to the spherical form visible in Figure 18A. This approach decreased the overall particle size to  $25 \pm 7$  nm, but also removed any trace of anisotropy. Citrate showed no specific binding to any crystal face but seems instead to hinder crystal growth by positively charging the particle surface. Phosphate binding led to amorphous particles, but also to the same phase impurities of iron phosphate that were discussed in the previous paragraph. The overall particle size decreased to  $35 \pm 21$  nm, but the polydispersity also increased by a large amount. The attachment of phosphate ligands likely caused strains in the crystal lattice that led to the observed growth anisotropy but also to the formation of other iron oxides. In this case CTAB showed no specific binding site and did not hinder the growth of particles in any direction. The resulting particles were as large as the original particles with  $56 \pm 10$  nm. After all, attempts to decrease the particle size by decreasing the reactant concentration or by applying growth limiting surfactants either failed to limit the growth of the particles by not attaching specifically enough or yielded undesired side effects like loss of shape or phase impurities. The reaction robustly yielded cubes or octahedra in the 50 nm range, that are hard to stabilize due to their high magnetic moment and size.

Ultimately, since the particles showed a strong magnetic moment, they agglomerated quickly, which increased their already hard to stabilize size. Large particles possess also significant mass which increases the pull of gravity on these particles, leading ultimately to precipitation and further agglomeration. Once particles are agglomerated and precipitated it is mostly impossible to separate and disperse them again due to the strong adhesive forces. This makes subsequent coating steps impossible, but the particles could still be used in conjunction with a stabilizing matrix for example with highly crosslinked PNIPAM. This would yield a highly magneto responsive material.

#### 4.1.2 Precursor based magnetite synthesis

Akaganeite with its tunnel structure is the ideal precursor for transformation into the different kinds of iron oxide. It was used as a universal precursor for all iron oxides occurring in this work. It was synthesized by forced hydrolysis of  $\text{FeCl}_3$  salt in aqueous medium. The iron salt causes the pH to be at around 3 during the reaction, which means the tunnel structure of akaganeite is filled with mostly chloride ions. Through the addition of  $\text{Na}_2\text{HPO}_4$  the shape is directed towards small acicular particles, also referred to as cigar shapes (Figure 20).[149] This is likely caused by a similar mechanism as the one described above for hematite where one crystal phase holds a favorable Fe-Fe distance when compared to the O-O distance of  $\text{PO}_4^{3-}$ . Another possible reason is a ligand exchange of the anion with surface OH-groups, which also might be selective for one crystal phase.[150] Our akaganeite particles show the usual morphology of small cigars with an average length of  $42 \pm 10$  nm and an average width of  $10 \pm 2$  nm.[126]

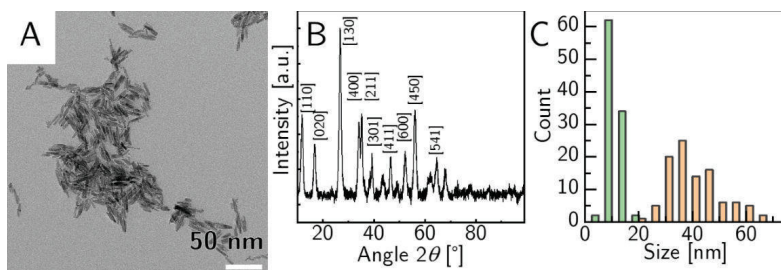
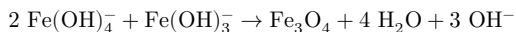
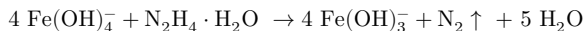
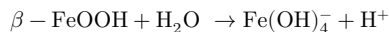


Figure 20: Akaganeite precursor particles (A) TEM image of the precursor with a length of about 30 nm and a width of about 10 nm. (B) XRD image with some referenced peaks of akaganeite from JCPDS PDF-Nr. 00-034-1266. (C) Size distribution histogram. The width is displayed in green, the length in orange.

The akaganeite precursor used to produce magnetite was also used to synthesize the other iron oxide phases: hematite and goethite. At first, we established the pathway from akaganeite precursor to a stable magnetite phase. We found out that the transition is easily done by using hydrazine as a weak base and as a catalyst, in conjunction with NaOH as a strong base.[15] Hydrazine fulfills the two-fold role of a weak base, that helps in adjusting the needed stoichiometry of  $\text{Fe(III)}:\text{Fe(II)}$  at 2:1 and on the other hand as a protection against



further oxidation after magnetite is formed. The proposed reaction mechanism is as follows:



The strong base NaOH leads to the dissolution of akaganeite to form the iron hydroxide species  $\text{Fe}(\text{OH})_4^-$ . Hydrazine hydrate then reduces this species to  $\text{Fe}(\text{OH})_3^-$  and the two iron hydroxide complexes react together to form magnetite.

We observed that heavy stirring in conjunction with the high pressures of a hydrothermal reaction vessel produces magnetite nanoparticles in the desired size range below 50 nm and with a pure phase (Figure 21C). We also tested the reaction in the absence of stirring without any applied pressure and the result also yielded a pure magnetite phase, but the size of the particles was inadequate (Figure 21A,B). It is immediately obvious from the TEM images, that the growth of the particles was not controlled sufficiently, leading to mostly cubic or amorphous magnetite particles. The size of the particles was widely distributed with a mean diameter of  $22 \pm 8$  nm for the best controlled sample. Uncontrolled growth is likely caused by aggregation of small growing particles coupled with Ostwald ripening. Since a stabilizing agent is missing, growing magnetite particles will likely aggregate even faster than other particles, because magnetic attraction is introduced into the system. Particles closer the bottom of the reactor are subjected to a stronger magnetic field and stronger mixing caused by the magnetic stirring bar, which would orient some magnetic moments in these particles and cause them to agglomerate with similarly oriented particles. Particles farther from the stirring bar will not “feel” a similar effect, the magnetic moments of the individual particles are oriented randomly to each other. This is a possible cause for the huge dispersity in badly stabilized samples. Some directional growth could be introduced by the surfactants left over from the precursor synthesis; we expect free phosphates to bind strongly to growing magnetite particles.

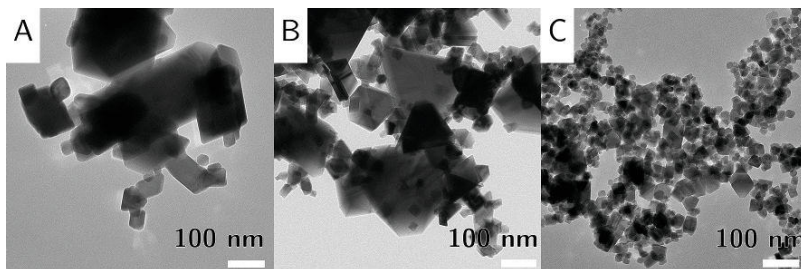


Figure 21: Magnetite particles synthesized under hydrothermal conditions with a precursor of akaganeite, without further surfactants. (A) Example of agglomerates created by insufficient stirring. (B) Example of large particles created when no pressure is applied during the hydrothermal treatment. (C) Example of a reaction with sufficient stirring and a pressure of 10 bar.

After the general reaction pathway for precursor-based reactions in a hydrothermal reactor was established, we had a look at the changes in a sample over time. We evaluated the shape of the particles using TEM (Figure 22A-D) and the phase of the particles using XRD (Figure 22E). To get a grasp for the general reaction pathway we chose reaction conditions without surfactants, since these may alter the morphology as well as the phase of the particles, as we already saw in this chapter on the example of  $\text{NaH}_2\text{PO}_4$ . Unfortunately, this had the side effect of losing control over the size of the particles, as is evident from the TEM images. All samples are polydisperse and we did not deem it necessary to determine the exact size distribution each time. Nevertheless, a transformation in the sample with time is clearly recognizable. After 5 hours of reaction time we see long rods in the sample that appear to have smaller particles on their surface (Figure 22A). Supplementing this with the observations from the diffractogram we can safely assume that the big rods contain goethite, while the majority of the sample is made from magnetite. The mechanism that leads to this is described as a dissolution-recrystallization process in literature.[15,118] The sample after 10 hours shows no long rods anymore (Figure 22B), but instead large agglomerates that can be identified as pure magnetite using the diffractogram. The images and diffractograms after 10 hours show no further change in the product, indicating that without surfactants the reaction is done sometime between 5 and 10 hours. Running the reaction longer than that, does not appear to have any negative

influence on the sample, but with surfactants I assume that a reduction of the polydispersity will take place in this timespan. This is backed up by the observations we did on the oxidative aging procedure I discussed in the previous chapter, where a slight size focusing happened after the magnetite phase was established.

When we tried sampling during the reaction from a big 125 mL reactor, we noticed that the process of sampling disturbed the reaction in a way that made the results irreproducible and not trustworthy. Therefore the time resolved reaction results shown here were obtained by performing each reaction in a separate 25 mL reactor, to get rid of the side effects of sampling during the reaction. Nevertheless, since no two reactions are exactly alike and the product may be the process of terminating the reaction and opening the reactor, some small uncertainty remains, whether all products would have arrived at the exact same endpoint, in terms of properties. The insight we gained from these kinetic studies is that a prolonged reaction time is only beneficial and therefore we performed subsequent reactions in this system for 24 hours. Since these kinetic studies are quite time and material intensive, we did not perform further studies on reactions with surfactants, since it is reasonable to assume that reactions with surfactants use the same pathway.[118]

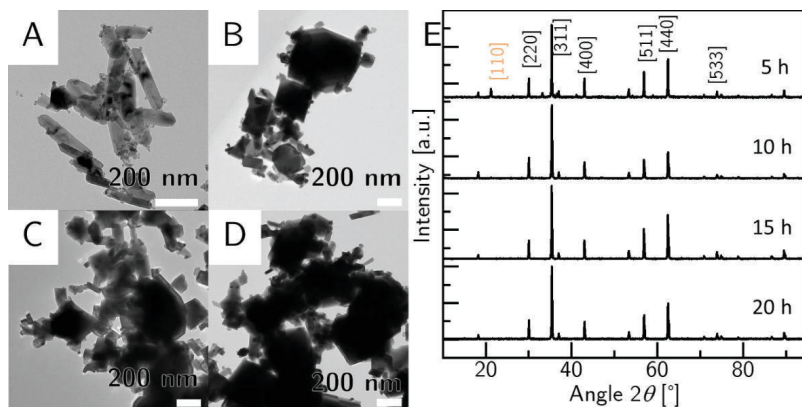


Figure 22: Time evolution of a precursor-based reaction in a hydrothermal reactor without surfactants. (A) 5 h after the start of the reaction. (B) 10 h (C) 15 h (D) 20 h (E) XRD of the reaction at 5 h intervals from 5 to 20 hours. The yellow index shows the location of the most prominent peak of goethite from JCPDS PDF-Nr. 00-017-0536, the black indices show a magnetite reference from JCPDS PDF-Nr. 01-075-1609.

Magnetization measurements reveal a saturation magnetization of 398 kA/m with a small coercivity field strength of 7.5 kA/m (Figure 23A). To compare that, magnetite particles with a diameter of 30 nm reportedly have a saturation magnetization of 437 kA/m ( $84 \text{ Am}^2/\text{kg}$ ) and a coercivity field strength of 65 kA/m.[151] The difference can be easily explained by the reduced size of our particles. The non-zero magnetic interaction of the particles without a field underlines the importance of stabilizers for magnetic particles to circumvent the agglomeration problem.

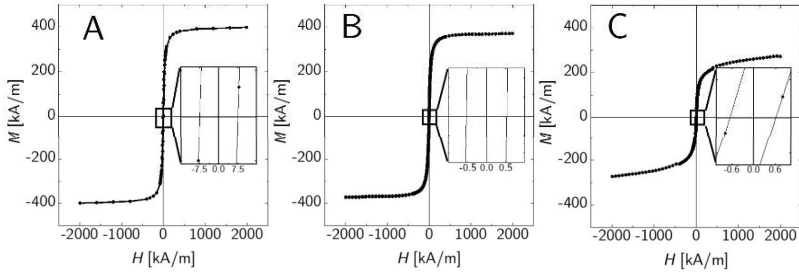


Figure 23: Comparison of the  $M/H$  curves of three different precursor based hydrothermal reactions. (A) Particles created without additional surfactants from a  $\text{NaH}_2\text{PO}_4$  coated precursor (B) Citrate coated particles created from a  $\text{NaH}_2\text{PO}_4$  coated precursor (C) Particles created with the help of dopamine from the same precursor.

Therefore, we tried different surfactants with the goal of influencing the particle growth direction as well as to stabilize the growing particles and prevent them from agglomerating. The two most successful surfactants were citrate and dopamine, both bidentate ligands. In the case of citrate, we observed a comparatively narrow size distribution of  $16 \pm 3 \text{ nm}$  (100 particles measured) (Figure 24A/C). The particles appear amorphous, no clear cubic shape is discernible, indicating that citrate does bind well to all growing crystal surfaces. No large agglomerates were observed in this sample, both growth control and stabilization appear to work. The XRD (Figure 24C) shows no impurity peaks, confirming a pure magnetite phase. The size evaluated utilizing the Scherrer-equation was determined to 14.4 nm, showing that the particles have good crystallinity and about 1 nm amorphous surface layer. The particles show a saturation magnetization of 373 kA/m with a very small coercivity field strength of 500 A/m (Figure 23B) . Note that the measurement accuracy for the field

strength is in the order of 1200 A/m, so these particles can be regarded as having no measurable hysteresis at room temperature. These particles are smaller than the ones synthesized without additional surfactants, disregarding the  $\text{NaH}_2\text{PO}_4$  present during the precursor synthesis. This explains the slightly diminished saturation magnetization and the small, almost zero hysteresis. Whether these particles are true superparamagnets cannot be determined without measurements at temperatures close to 0 K, but these particles show all the characteristics of superparamagnetic particles at room temperature.

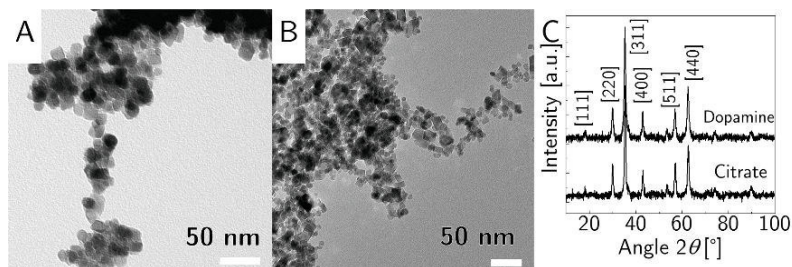


Figure 24: Surfactant coated particles, synthesized under hydrothermal conditions. (A) TEM image of citrate coated particles. (B) TEM image of dopamine coated particles. (C) XRD of the particles shown in A and B with references from JCPDS PDF-Nr. 01-075-1609.

The particles coated with dopamine show a more polydisperse distribution in size and shape (Figure 24 B/C). While some particles are amorphous, some particles show a slightly elongated shape, the distribution is  $16 \pm 5$  nm for the long axis and  $11 \pm 3$  nm for the short axis across 100 particles. The XRD reveals another pure magnetite phase, not essentially different from the citrate coated particles. The crystalline proportion is with 13.3 nm derived from the Scherrer-equation smaller than the diameter measured in TEM, indicating that the large particles could have a larger amorphous volume on the particle surface. Dopamine also fulfills a stabilizing role for the particles, but since the amount deployed in the reaction is very small (27 mg or 142  $\mu\text{mol}$ ) compared to the amount of precursor (27 mL at 5 wt. %, 1.35 g or 15 mmol) resulting in an iron : dopamine ratio of 106 : 1, the particles were not stable on their own, so PVP was added to stabilize the particles for further functionalization. The saturation magnetization of these particles is at 273 kA/m with a very small coercivity field strength of 600 A/m (Figure 23C). The low saturation magnetization indicates that the

volume contributing to the magnetization, the ferrimagnetic volume inside each particle, is lower than in the sample without dopamine and the one with citrate. This can have multiple causes: the surfactant could have a direct effect on the orientation of the surface spins, similar effects were shown for carboxylate anchoring groups[152], oxidation could have occurred, transforming the magnetite in the sample to the less magnetic maghemite, or some other effect could have influenced the crystallinity of the sample and reduced the magnetization. Another possible explanation is that the loss in saturation magnetization is caused by the additional stabilization of the dopamine coated particles with PVP. PVP having a large molecular mass and being supplied in excess could make up a big portion of the sample weight, thus reducing the magnetic material in the sample.

After all, dopamine was the only surfactant in our series of experiments that resulted in a slight increase in anisotropy in the sample. Although it decreased the saturation magnetization slightly, the method seems to be a step in the right direction.

#### 4.1.3 Magnetite microwave treatment

Apart from conventional reactions in a beaker and the hydrothermal technique we also used the relatively new and fast method of microwave treatment to facilitate the transition from an akaganeite precursor to magnetite. This approach was first done by Milosevic *et al.*[28] and to the best of my knowledge not further pursued by other groups. The general method is not very different from the one we deployed in the hydrothermal reactor, as the precursor is almost the same, except for the use of dopamine instead of  $\text{Na}_2\text{HPO}_4$ , and hydrazine is again used as a catalyst for the reaction. The precursor particles were synthesized as described in the reference and we received the same product without any significant deviations. The particles are  $34 \pm 10$  nm in length and  $8 \pm 2$  nm in width and some very small amorphous particles are present. In the XRD of the precursors only an akaganeite phase is present. The reaction in the microwave happens very fast, after two cycles each of about 40 seconds, a temperature of 100 °C is reached and the particles precipitate into a black magnetic solid. The product keeps almost the same shapes as the precursor particles (Figure 25A,B). The XRD shows a big portion of the akaganeite phase, but also some magnetite peaks that were more pronounced after the reaction. In the literature, the product contains “26 wt. % of  $\beta\text{-FeOOH}$ , 71.3 % of maghemite and 2.6 % of magnetite”[28], determined by XRD Rietveld refinement and Raman

spectroscopy. Our product indicates the presence of maghemite and magnetite by the [112] peak of magnetite in the diffractogram (Figure 25C). The large particles in the TEM image as well as the black color and magnetic attraction also indicate that a significant portion of the product is magnetite or maghemite. By XRD alone, a distinction between magnetite and maghemite is an approximation at best, so we did not determine whether the emerged phase is either of those. However, we also found a large portion of an akaganeite phase, which reduces the achievable magnetization. This method shows a possible pathway towards anisotropic structures, but the product needs further refinement before it can be used in a hydrogel. This approach could only be touched briefly in this work, but microwave treatment as a method for magnetic particle creation is very promising, because the method is fast and allows for the precursor to retain its shape, which was not achieved with any other method.

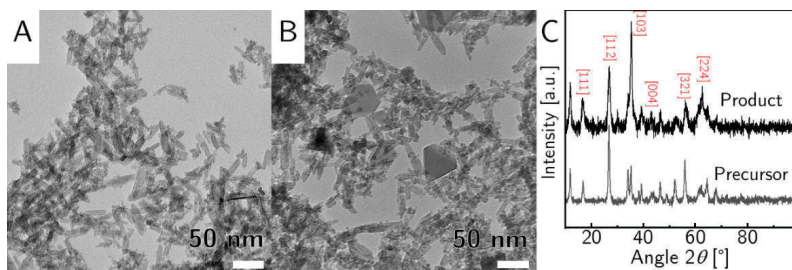


Figure 25: Particles synthesized in a microwave reactor. (A) The precursor particles of akaganeite coated with dopamine (B) The particles after the microwave treatment. (C) XRD of the particles before and after microwave treatment. The magnetite peaks that grew during the reaction are highlighted in red after JCPDS PDF-Nr. 01-075-1609.

## 4.2 Magnetic cores: Goethite, the anisotropic anti compass

The main pathway to create goethite from any iron precursor is to set the reactant solution to rather strongly alkaline conditions.[153] Goethite matches the description of an anisotropic magnetic particle perfectly because it naturally grows into long needle shaped particles. On top of its large form anisotropy goethite has also highly interesting magnetic properties that were well reported by Lemaire *et al.*[17] Contrary to a compass needle, a goethite needle orients not to the magnetic north but orthogonal to it and on top of that, its orientation is not constant but changes with the strength of the applied field. Our hydrothermal synthesis pathway allowed for significant improvements to the existing methods of creating goethite. Our synthesis pathway allowed to achieve some control over the size of the nanorods and thus to control their field dependent behavior. The long-term goal was to incorporate this material into a PNIPAM matrix and to study the influence the particles have on the matrix and vice-versa.

### 4.2.1 Goethite synthesis by aging

The main literature method to produce goethite is to use an aging protocol, where an iron precursor is aged at a pH value around 12 for several days. We were successful in reproducing the results produced by Lemaire *et al.* [18] synthesizing a goethite phase with flat elongated rectangular prisms (Figure 26).

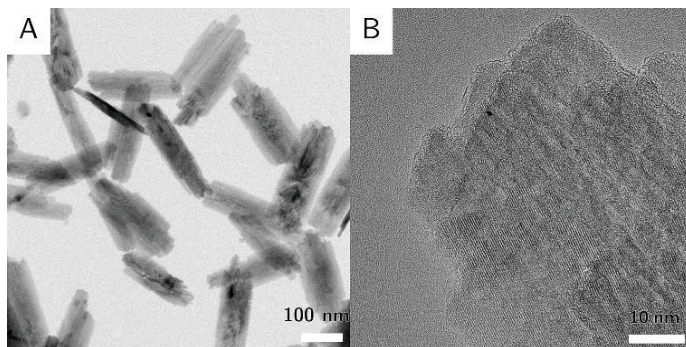


Figure 26: Goethite particles after aging for eight days, following a protocol by Lemaire *et al.*[18] (A) TEM-image (B) HR-TEM image. Both images show that the samples are polycrystalline.



The size distribution gives us a length of  $220 \pm 40$  nm and a width of about  $74 \pm 17$  nm, (Figure 26A) compared to the  $150 \pm 25$  nm and  $25 \pm 10$  nm produced in the reference. The third and shortest crystallographic axis ( $10 \pm 5$  nm in the reference), the c-axis, was also observed in our samples, but not in an adequate number to gain statistically significant results. The particles synthesized by us as well as the reference particles seem to be polycrystalline (Figure 26B).

This polycrystalline nature as well as the long aging time to produce the particles led us to move on with hydrothermal aging, as this could drastically shorten the reaction as well as introduce a better crystallinity.

#### 4.2.2 Goethite synthesis by precursor based hydrothermal reactions

By transferring the reaction into a hydrothermal reactor, we could greatly reduce the time needed for the aging process from days to hours. To produce our goethite particles, we used a two-step procedure that again involves precursor particles that consist of akaganeite. We found that once these precursors are subjected to a pH of 12 they transform into goethite. The phosphate on the surface of the precursor particles was not removed, so it might serve as a structure guiding agent. The quality of the goethite yielded by this reaction is mainly dependent on the precursor. After the precursor synthesis the pH value of the precursor solution is around 3. If the solution is then concentrated the pH value decreases further and the quality of the precursor begins to deteriorate. If the precursor is left in a medium with pH value below 3 the particles slowly dissolve until spherical particles remain. These transformed precursor particles lead to impurities in the product (Figure 27A). The interior structure of akaganeite is quite volatile at neutral pH values which lie around its isoelectric point of about 7.[154] The chloride in the interior tunnel structure can be swapped with hydroxide ions, this is less of a problem in an acidic milieu, therefore the particles should not be dialyzed, because this increases the pH value and washes out the chloride ions. The reactions using the precursor are strongly dependent on the concentration of chloride in the akaganeite tunnel structure, so changes in the precursor synthesis reduce the reproducibility of the product. Therefore, a lot of problems can be circumvented by sticking to one synthesis protocol.

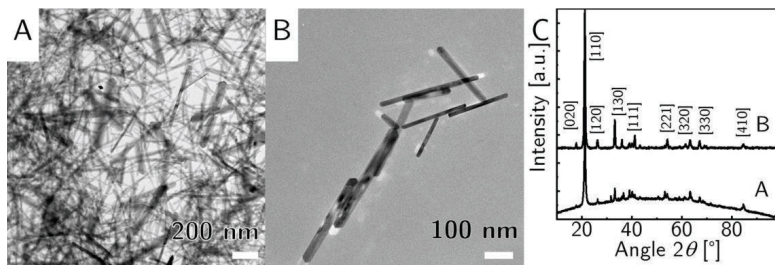


Figure 27: Goethite nanorods synthesized from different precursor batches. (A) Goethite nanorods from a precursor batch where chloride ions were exchanged for hydroxide ions. (B) Goethite nanorods from a precursor batch that was synthesized at 0.1 M and directly used for the second reaction. (C) XRD of the goethite rods in A and B, A was taken without subtracting X-ray fluorescence, the peaks are referenced after JCPDS PDF-Nr. 00-017-0536.

The highest reproducibility can be achieved, when the precursor is already synthesized in the exact concentration needed for the second reaction (0.1 M) to circumvent the problems of changing the ion concentration while concentrating the particles. After the first step yielded stable and reproducible results, in the second step the  $\beta$ -FeOOH particles were transformed to  $\alpha$ -FeOOH particles, so a change in the crystal structure was performed. As mentioned above, this requires a pH value of 12. The chloride ions are exchanged by hydroxide ions and the structure is reformed from a tunnel structure into the two connected octahedra chains. We found that goethite can be stabilized in aqueous media by PVP during as well as after the reaction. During the reaction, the long particles get stabilized instead of precipitating and thus enabled to continue growing, which allows for long rods up to 1  $\mu\text{m}$  in length. Without PVP, the reaction results in shorter particles. Small amounts of PVP introduced at the start of the reaction can also decrease the size dependent polydispersity. We pinpointed an influence on the particle length to the exact timing of the addition of PVP to the reaction. When PVP is given right at the start directly after adding NaOH, the particles grow shorter compared to the addition of PVP as the last ingredient after the precursor is added into the reactor. Prolonging the reaction time beyond a length of two hours does not change the product in a significant way. If there is a change, it is that the polydispersity increases and the particles shrink, impurities seem to be slightly favored. In short, there was no advantage in increasing the reaction time. The stirring speed on the other hand had a great influence on the product. The

reaction running under minimal perturbation by stirring produced longer particles than a reaction that was heavily stirred. We attributed this behavior to the increased volatility of long goethite rods; at strong perturbations, the rods simply break mechanically. Too little stirring was also detrimental as the educts were not properly mixed, which led to impurities caused by an uneven distribution of the pH value in the reactor. The best stirring speed was found to be 500 rpm to get reliable and reproducible results (Figure 27B).

With the above-mentioned combination of controlled precursor properties, a reaction time of 2 hours and a pH value of 12, we produced three goethite nanorods samples of different sizes. The parameters used to tune the length of the particles are displayed in Table 1.

Table 1: Parameters to create three desired nanorods sizes. The reaction time was set to 2 h, the pH to 12 by addition of NaOH. The reactions were done in a 25 mL hydrothermal reactor.

| <b>Length<br/>[nm]</b> | <b>Stirring speed<br/>[rpm]</b> | <b>Stirring Bar<br/>[mm]</b> | <b>PVP<br/>addition</b> |
|------------------------|---------------------------------|------------------------------|-------------------------|
| 206 $\pm$ 62           | 1000                            | 20                           | After NaOH              |
| 274 $\pm$ 97           | 500                             | 12                           | Last                    |
| 361 $\pm$ 129          | 100                             | 12                           | Last                    |

In Figure 28 we present three different samples produced to fit into the categories of short ( $\sim$ 210 nm, Figure 28A), intermediate ( $\sim$ 270 nm, Figure 28B) and long ( $\sim$ 360 nm, Figure 28C) nanorods. These nanorods were stabilized by PVP after the reaction. Goethite nanorods can also be coated with silica after the reaction, more will be told in the section about silica coatings (section 4.3).

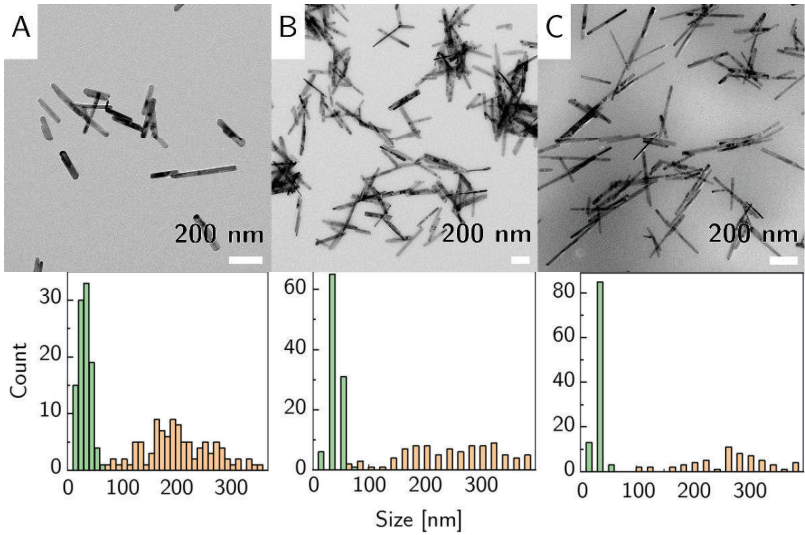


Figure 28: Goethite nanorods of different lengths synthesized in a precursor based hydrothermal reaction. Below the graphs the matching histograms are shown. (A)  $206 \pm 62$  nm x  $32 \pm 10$  nm (B)  $274 \pm 97$  nm x  $35 \pm 10$  nm (C)  $361 \pm 129$  nm x  $26 \pm 6$  nm. In the histograms the green columns depict the width of the particles and the orange columns the length.

#### 4.2.3 Goethite orientation

As explained in the theory (chapter 1.1.1.3.), goethite has the interesting property of changing its orientation when magnetic fields of different strengths are applied. To understand the orientational behavior, we can look at the magnetic energy of a single goethite nanorod in a micromagnetic model, which is already introduced in chapter 2.1.3.[18]

Considering that the magnetic susceptibility anisotropy is negative for goethite, there are essentially two different domains. In the first domain at a weak field, goethite nanorods will align parallel to a magnetic field due to the unaligned surface moments. Thus the minimum of the magnetic energy is located at  $\theta = 180^\circ$  which translates into an orientation of the long axis parallel to the field. While in the second domain in a strong field, goethite nanorods will align perpendicular to the field due to the negative anisotropy of their magnetic

susceptibility. In this domain the energetic minimum is located at  $\theta = 90^\circ$  which translates to perpendicular orientation of the long axis to the field. There is also a region in between the two domains where the minimum points at a finite angle, meaning the sample appears isotropic. Depending on the volume of the particles the point at which the energetic minimum changes shifts its position. To estimate the effects of particle size, three samples (as discussed in chapter 3.2.2) were investigated, one with short rods of about 210 nm length, one with intermediate length rods of 270 nm and one long particle sample with 360 nm length.

The orientation of the particles was measured with a 2D detector by SAXS at the University of Hamburg. We did not look at the additional information about the particle form factor, because of the  $q$ -range we could resolve ( $0.0912 - 2.08 \text{ nm}^{-1}$ ). The dimension of the long axis is larger than 200 nm this appears as a minimum in the intensity at very small  $q$ -values ( $< 0.022 \text{ nm}^{-1}$ ). In a standard experimental SAXS setups this  $q$ -range is covered by the beam stop if no very large detector distances are available. Here we wanted to focus on the orientation of the particles which could be detected the best either within the  $q$ -range which probes the size range of the length of the particles or even better with the length scale of the width of the particles due to the similar sizes of the width of the particles used.

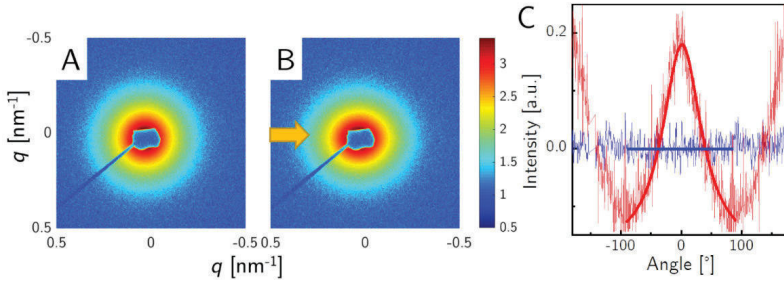


Figure 29: SAXS Detector image for a 210 nm goethite sample in a magnetic field. (A) 0 mT (B) 533 mT. The images are in false colors with a logarithmic scale for the intensity. (C) The azimuthal profile of the normalized intensity plotted against the angle in a circle around the beam stop. The averaged intensity at 0 mT is plotted in blue, with the solid line showing a fit, the averaged intensity at 533 mT is plotted in red, the solid line showing a Lorentz fit. The evaluated  $q$ -range was between  $0.163$  and  $0.507 \text{ nm}^{-1}$ . The angle  $0^\circ$  is starting at the  $x$ -axis of the detector image and proceeds counterclockwise. The direction of the magnetic field is indicated by the yellow arrow.

Without field the particles show an isotropic scattering pattern in the 2D SAXS image (Figure 29A). When the rods orient, i.e. perpendicular to the applied field, here shown for a field of about 533 mT in horizontal direction, the scattering pattern will deform to an ellipsoidal pattern (Figure 29B).

For an orientation of the long axis of the cylinders perpendicular to the magnetic field, the infield direction shows an elongated profile and the direction perpendicular to the field slims down. This happens because the rods align in the field and the oriented goethite rods are parallel to each other and modulate the scattering pattern. When the beam scatters only the short axis the minimum of the intensity is pushed out from the beam stop, so the  $q$ -values get larger. Contrary if the beam scatters only the long axis, the minimum is moved closer to the beam stop or even behind the beam stop. Therefore, we observe both axes simultaneously.

To analyze the orientational behavior the azimuthal profile of the 2D detector image of the scattering pattern was determined by integrating the intensity in circle segments around the beam stop averaged over the  $q$ -range between 0.163 and 0.507 nm<sup>-1</sup>. The angle 0° is starting at the  $x$ -axis of the detector image and proceeds counterclockwise. Without field we get a straight line and at 533 mT we observed that the normalized azimuthal intensity peaks along the  $x$ -axis at 0° and 180° (Figure 29C). As discussed before a maximum in field direction (at 0° and 180°) means that the particles are oriented perpendicular with the long axis to the field.

To analyze the azimuthal intensity a Lorentz-fit was applied. The position of the maximum of the fit can be utilized to get a function for the orientation of the nanorods. This orientation function is called the Herman Orientation function already mentioned in the theory but redisplayed here:[139]

$$f_H = \frac{1}{2} (3 \langle \cos^2 \Phi \rangle - 1) \quad (30)$$

Here  $f_H$  is the order parameter and  $\Phi$  is the position of the long axis of the particles compared to the field. This function can take values between -0.5 and 1. 1 depicts a parallel orientation of the long axis to the magnetic field, 0 depicts no orientation, i.e. isotropic scattering, and -0.5 depicts a perpendicular orientation of the long axis to the magnetic field. Since we are in the  $q$ -region probing the size of the small axis of the particles with our setup, the angle of the maximum of the fit monitors the orientation of the small axis and the minimum of the fit

monitors the long axis. This means we add  $90^\circ$  to the angle of the position of the maximum of the fit to get the orientation of the long axis.

The field strength at which the pattern showed visible orientation, so the onset for an observable peak (see the cyan line in Figure 30A), was dubbed the required field strength, because it is the field strength required for perpendicular orientation. When the field strength is further increased the peak grows, which means more rods orient in the magnetic field and contribute to the intensity.

For all three samples of about 210, 270 and 360 nm, we determined the azimuthal intensity between 0 mT and a maximum field of 533 mT, and we can see an interesting trend in the Lorentz-fits (Figure 30). The lines shown are the Lorentz-fits of the measured intensity for the peak around  $0^\circ$ . We tried to fit the parallel orientation which would show two peaks at  $-90^\circ$  ( $=-270^\circ$ ) and  $90^\circ$ , but those fits did not converge. For the largest sample we can see that the fits for the lower field strengths did not have their maximum around  $0^\circ$ , the intensity was very low and the orientation is hardly visible over noise.

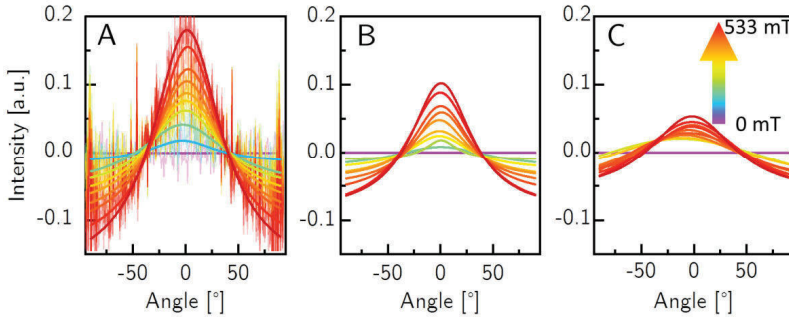


Figure 30: Lorentz-fits of the azimuthal intensity integrated along each angle between  $-90$  and  $90^\circ$ . (A) 210 nm nanorods displayed together with their normalized azimuthal intensity for comparison (B) 270 nm (C) 360 nm. The measured field strength went from 0 to 533 mT for each sample. Only field strengths with a clear difference in orientation compared to the previous one are shown, the color of the fits indicates the field strength as shown by the arrow color bar in (C).

When the short axis is parallel to the magnetic field, the orientation function equals  $-0.5$ , this means that the long axis is perpendicular, and the particles orient perpendicular to the magnetic field. When the orientation function is  $1$ , this means that the particles are oriented parallel to the magnetic field because the short axis is perpendicular to the magnetic field and the long axis is parallel.

orientation function the changes in orientation are easily visible (Figure 31A). Note that the position of the maximum was derived from a Lorentz-fit. When the fit did not converge or produced obvious errors, so when the particles were not oriented and the scattering was isotropic, we set the value for the position manually to zero. The orientation function jumps from zero to -0.5, but this does not mean that all particles are oriented instantly, the function shows only in what direction the rods are mainly oriented, not the degree of this orientation. The orientation function shows that we get an increase in the field strength required for reorientation with the length of the particles. The parallel orientation for these samples was not observed, because the concentration of the particle dispersion was low and we only measured each field strength for 300 seconds. It is likely that the parallel orientation is lost to noise, since it is quite a lot weaker than the perpendicular orientation in this  $q$ -range. The parallel orientation is mainly related to and caused by the surface of the particles.[18] Since the magnetic moments on the surface of the particles are uncoupled, they are free to align in a magnetic field. The influence of the surface is clearly visible in Figure 31B. Here, the surface area is plotted against the field strength required for an orientational change. There is a roughly linear dependency of the switching field strength on the surface area in the investigated particle size range, but we must keep in mind there were only three points to fit.

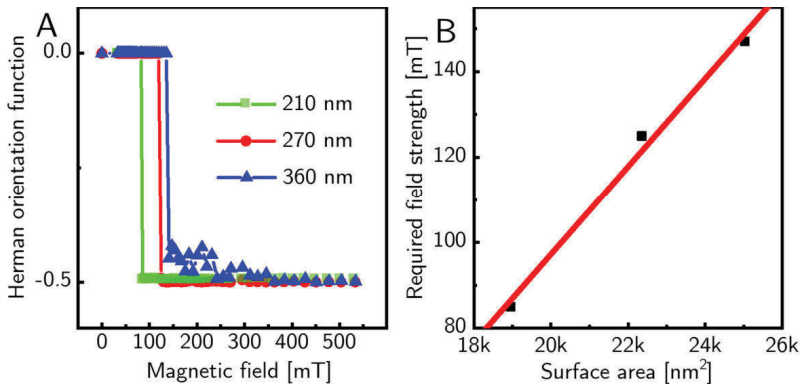


Figure 31: (A) The Herman orientation function of the orientation compared to the particle length in dependence on the field strength (B) The required field strength for an orientational switch in correlation to the surface area of the nanorods.



We did not observe the parallel orientation at low field strengths for the three samples we measured at our in-house SAXS setup, therefore we took the small sample, concentrated it from roughly 0.4 wt. % to 1.5 wt. % and measured it at the BESSY facility in Berlin. Here we had a synchrotron setup with high brilliance, but this setup only had four field strengths of 14, 47, 79 and 615 mT available. We determined the azimuthal intensity around the beam stop and fitted it to see the orientation (Figure 32A) within the  $q$ -range 0.125 and 0.388 nm<sup>-1</sup>. The magnetic field setup is in the same direction, high intensity at 0° means the particles are oriented perpendicular to the field and a peak at 90° means the particles are oriented parallel to the field. In this setup we saw the orientation of the particles parallel to the field because of the improved signal/noise ratio of the setup paired with a higher concentration for more signal and an average at a smaller  $q$ -range. We also used the position of the minima to measure the orientation parameter and we saw both orientations, but since the field range was very limited, we could not gauge the field strength required to switch the orientation from parallel to perpendicular (Figure 32B). However, since the sample is essentially the same, the required field strength for the switch measured in-house should still be the same.

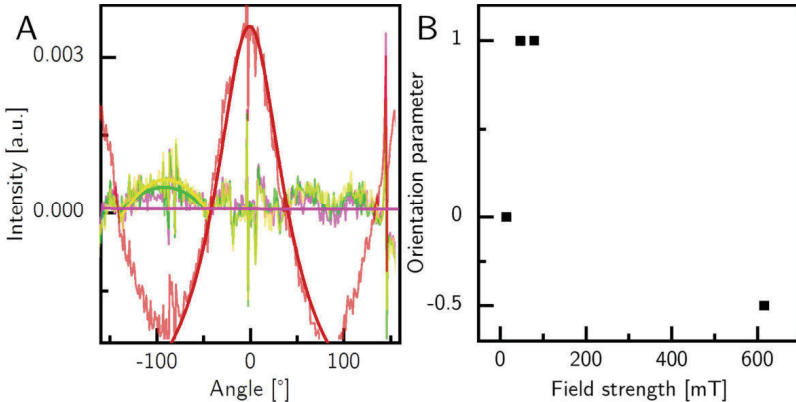


Figure 32: Orientation of a small nanorod sample measured at the BESSY facility. (A) Normalized azimuthal intensity measured at different field strengths with Lorentz-fits. (B) Herman orientation function derived from the fits in (A).

Above the required field strength to orient the particles the peak of the normalized azimuthal intensity increases with higher field strength. From the difference between maximum and minimum a degree of the orientation can be determined (see Figure 33A for reference). The larger the difference the more particles are oriented in the sample. However, we do not know if this was sufficient to achieve full orientation. Since we did not obtain a reliable value for 100 % orientation, we could not determine the degree of orientation in absolute values, however we can still obtain relative values when comparing the curves. From the Lorentz fits we determined the relative degree of orientation (Figure 33B).

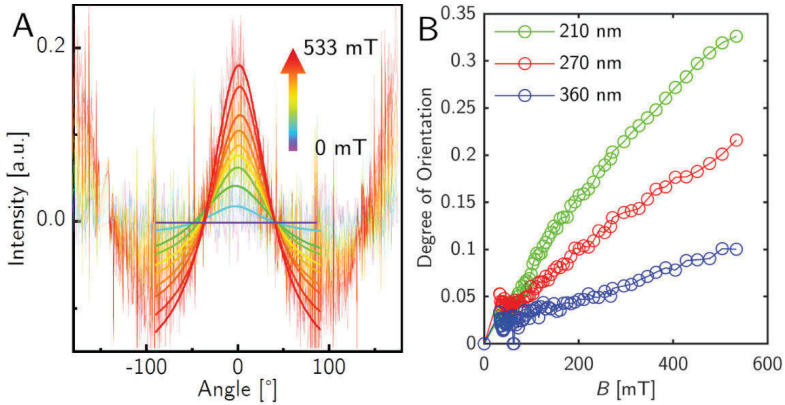


Figure 33: Differences in the orientation of three different length goethite samples with an increasing magnetic field. (A) The fitted intensity of a 210 nm sample in a field from 0 to 533 mT. The strength of the magnetic field is indicated by the colors of the curves, the scale is shown on the arrow. (B) The relative degree of orientation estimated by the difference between the maximum of the fit to the intensity and the minimum.

Taking this degree of orientation, we see that the shortest sample shows a bigger difference between zero orientation and the orientation at 533 mT than the longer samples. There is a clear dependence of the readiness to orient on the size of the particles. The small particles have an easier time rotating, while the longer particles seem to be hindered, they require a higher field strength to orient to the same degree as the smaller particles. These assessments can only be made relative to each other, since we did not measure a sample with 100 % orientation. The height of the fit is also influenced by the polydispersity of the sample.

In this section I showed that the three goethite nanorod sizes synthesized in our lab also change their response to a magnetic field along with their size. By measuring particles at a higher concentration with a more powerful SAXS setup we could also see the parallel orientation and I expect that we simply did not see the parallel orientation before because of the bad signal to noise ratio. We saw that the field strength required to switch the particles in their orientation from parallel to perpendicular to the field increases when the surface of the particles increases. This supports the theory that the weak magnetic moment caused by the unaligned magnetic moments on the particle surface is responsible for the parallel orientation at low field strengths. In addition, the orientations parallel to the field at low field and perpendicular to the field at high fields can be well explained by the internal magnetic energy of the goethite nanorods.

### 4.3 Silica shell: A stabilizing shell and the bridge to covalently bound gels

The synthesis of the silica shell was done to increase the long-term stability of the magnetite particles and to protect their surface from oxidation. Also, silica offers the possibility of easy functionalization utilizing the surface chemistry of silane groups. Silica shells were synthesized either by the method named after Werner Stöber[45] or in a bi-phase method derived from a paper by Zou and coworkers.[44] The deciding difference between the two is that the bi-phase method is carried out in an aqueous solvent while the Stöber method requires ethanol as the solvent.

#### 4.3.1 Stöber's adapted method

Stöber's method has been a standard method since its emergence in 1968 and was later transferred into a general particle coating protocol by Graf *et al.*[43] However, in the following paragraph it will always be referred to as Stöber's method. We applied the method to every particle system we synthesized that possessed enough colloidal stability. The citrate coated particles for example are very stable in water and slightly less stable in ethanol. When the synthesis of the shell was conducted at low particle concentrations a major part of the coated particles were single particles. Some large particles showed agglomeration prior to the treatment, so they were coated into a single silica shell (Figure 34A). This can in theory be avoided by doing careful size selection before the coating step,

but this was not tested enough for reliable results in our lab, so some multi-core particles remained in all samples. The thickness of the silica shell could be tuned from 9 nm to more than 30 nm. The dispersity of the shell thickness is quite low, mostly about  $\pm 1$  nm. After the coating, the particle size dispersity is greatly reduced. The dispersity is reduced because the silica shell grows uniformly around the particles, so the overall size decreases while the deviation of the particle size stays constant, thus the relative deviation is reduced. If there are particles in solution that precipitate during the reaction, the thickness of the silica shell around the remaining particles does not increase anymore, but instead small silica particles without a magnetic core are formed (Figure 34B). The most important criterion for a successful silica coating by Stöber's method is the colloidal stability of the seed particles prior to the reaction in ethanol at high pH. This shows the major drawback of this method: after the synthesis the particles should be stable in water and then be able to be transferred into ethanol at high pH which poses quite the challenge for most particle/ligand systems.

The reaction also works very well to coat non-magnetic particles with a silica shell, as shown on the example of goethite in Figure 34C. These particles were stabilized with PVP and the solubility in ethanol should be equally good as the solubility in aqueous solvents. However, we observed agglomeration in the samples prior to the coating step leading to mostly multiple coated particles per silica shell. The silica shells produced by Stöber's method become very smooth once they exceed a size threshold and the particles grow spherical, even if the coated particles are not spherical in the beginning.

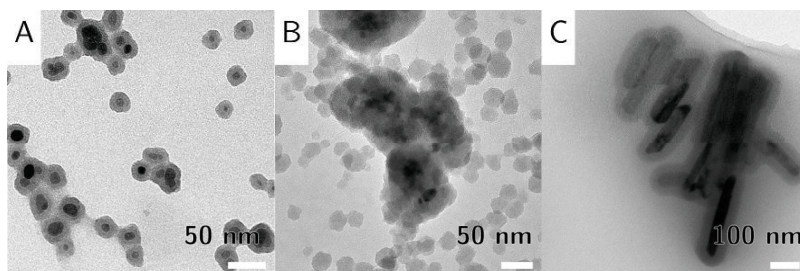


Figure 34: Particles coated with a silica shell by the adapted Stöber method. (A) Citrate coated magnetite particles, coated with a  $9 \pm 1$  nm thick shell. (B) PVP stabilized magnetite particles. The particles are agglomerated, and a lot of core-less silica particles were produced. (C) PVP stabilized goethite core/silica shell particles. The shell is roughly 31 nm thick.

Stöber's method offers a well-established procedure to create uniform silica coated particles and can be easily adapted to coat particles with a uniform shell. However, this method requires colloidal stability in organic medium, which can create issues with particle agglomeration during the phase transfer.

#### 4.3.2 Bi-phase method

The two-phase method has the advantage of working with water as solvent. This method is applicable to all particles with colloidal stability in water, so to all particles synthesized and stabilized in this work. The coating worked especially well on particles that were coated by citrate (Figure 35A). This was expected because these particles were the most stable in water in our experiments. Still, there are instances where more than one particle is present in one silica shell. The shell thickness can also be continuously tuned starting from about 6 nm up to at least 30 nm shell thickness. This was the largest shell we tested, but if an application requires an even thicker shell this can also be done by this method.[44] The most important property that particles must possess for the coating of single particles to be successful is prolonged colloidal stability. Unfortunately, the stability of the hydrothermally prepared particles was not enough to be coated as single particles. One of the successful approaches is shown in Figure 35B, while the particles are obviously coated, they still agglomerate and it is hard to discern, whether the shells are around one or more particles. These particles were not colloiddally stable after the silica coating, so no further investigations could be done.

As described before, this reaction is theoretically applicable to all systems in an aqueous solvent, we tested this by coating goethite nanorods that were stabilized by PVP. The coating can be easily adjusted down to 6 nm shell thickness (Figure 35C). At this shell thickness the shell appears rough on the outside, which is a feature often observed with this method that does not show up on particles coated by Stöber's approach. Since this seems to be mainly an aesthetic problem, the shape of the coating was ignored during our experiments.

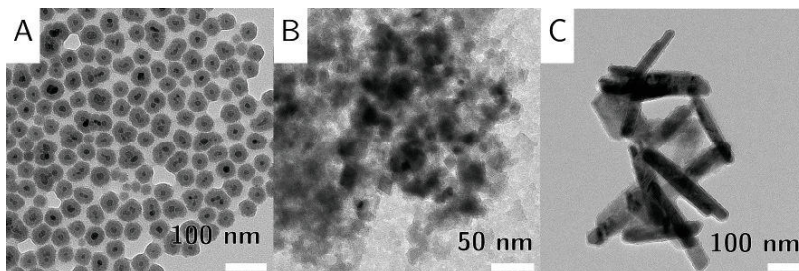


Figure 35: Particles coated with a silica shell by the bi-phase method. (A) Citrate coated magnetite particles coated with a  $13 \pm 1$  nm thick silica shell. (B) PVP stabilized magnetite particles. The particles are largely agglomerated, but some particles were coated individually. (C) PVP stabilized goethite particles coated with a roughly 6 nm thick silica shell.

This method offers similar results as Stöber's method in terms of silica coating of colloiddally stable particles. The adapted method by Graf *et al.* provides a smoother shell and although this was not important for our application it is nonetheless an important factor to consider. The great drawback of Stöber's method is the required stability in ethanol which is circumvented in the bi-phase approach by working in an aqueous medium. If the goal was an aqueous system the bi-phase approach offered more reliable results in general, while Stöber is generally preferred for organic media, when the particles can be transferred into ethanol at high pH.

One important property of silica shells in general is their easy functionalization with silane agents. We functionalized our silica shells with TPM to have binding sites for NIPAM, to bind the hydrogel covalently to the particles. Once the silica shell is functionalized with TPM, the particles are no longer soluble in water, they need to be transferred to ethanol. In the end, a phase transfer is necessary for both the Stöber approach and the bi-phase approach. The difference is whether the transfer happens to coated or to uncoated particles. Since the surface of the particles is more volatile before the coating with silica, we preferred the bi-phase method for most particles that were later incorporated into a gel. However, we achieved satisfactory results with both methods.

## 4.4 PNIPAM hydrogels, more than a simple matrix

Hydrogels were the last step in the synthesis of an anisotropic multiresponsive system. The nanoparticles were synthesized to be anisotropic in shape and magneto-responsive in their properties. The hydrogel should introduce another stimulus by reacting to a change in temperature by changing its size. The goal was to connect the change in size to the magneto response of the particles. There are two different approaches to create a hydrogel which is thermoresponsive as well as magneto responsive. The first approach is to covalently bind the particles to the matrix, so any response, movement or heat, can be directly transmitted. In the other approach the particles are not permanently connected to the matrix, the connection is mainly mitigated by physical interactions. In this case the particles are mixed into the hydrogel matrix. The particles are within the aqueous phase of the hydrogel. In the swollen state of the hydrogel the particles can move and rotate more freely than in the collapsed hydrogel state.

### 4.4.1 Covalently bound magneto hydrogels

#### 4.4.1.1 Microgel

After the particles were functionalized with TPM, utilizing their easily accessible silane chemistry, NIPAM was polymerized onto the silica shell in a grafting through approach. The polymerization was a free radical emulsion polymerization. At 60 °C PNIPAM is largely insoluble in water and polymers would precipitate. However due to the charges from the polymerization initiator KPS on the PNIPAM polymer chains the hydrogel is colloidally stable. For the growing PNIPAM chains to attach to the particles, the particles need to be very stable. This was tested on a model system made of  $54 \pm 10$  nm hematite cubes (Figure 36A), coated with a  $14 \pm 2$  nm silica shell (Figure 36B). The cores were colloidally stable in aqueous solution and then covered by a silica shell utilizing the Stöber process and functionalized by TPM. The shell was then incorporated into a microgel and the DLS measurements confirm that only one particle was present in each microgel bead (Figure 36C), since the hydrodynamic radius above the LCST allows for only one core to be present. This approach was done during the bachelor thesis of Nils Nun and later published in cooperation.[63]

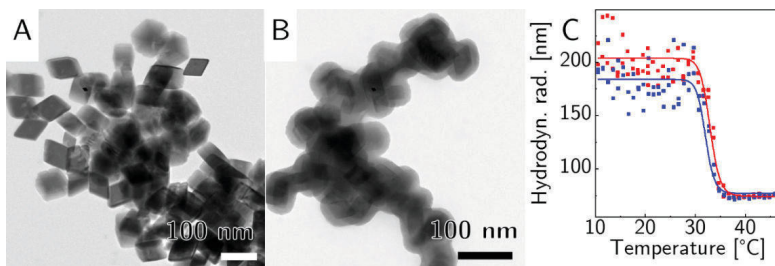


Figure 36: Example for a gel made with hematite cubes that were coated with a silica shell. (A) Hematite cubes with a core diameter of  $54 \pm 10$  nm (B) The cores from (A) coated with a  $14 \pm 2$  nm silica shell. (C) The thermoresponsive behavior of the cores incorporated into a PNIPAM shell measured with DLS.[63] The red dots and fit show the curve upon heating, the blue symbols the curve when cooled down.

Hematite is a great model system because the core size is roughly equal to the magnetite particles created in this work and it is easy to stabilize in an aqueous medium by peptization with  $\text{HNO}_3$ . The drawback of this system is the very weak magnetic moment of hematite. At the low concentrations in a hydrogel there is no magnetic influence of the particles on the matrix. Therefore, the coating reaction was performed on magnetite.

Multiple coating reactions were done during this work, but during most of them the particles precipitated too quickly and no joint phase was formed from particles and PNIPAM. This happened due to the pronounced magnetic moment of the magnetite particles, which leads to quick agglomeration before most stabilizing reactions can take place. On the one hand this shows the desired properties of magnetite, proving that it is a good choice for a magnetic core, but on the other hand it makes the clean incorporation as single core particles quite challenging. However, we did succeed in coating magnetite particles with silica and polymerizing a PNIPAM shell around these particles. Due to the strong magnetic moments there are still some clusters that got coated during the reaction, but we also see some single core silica particles (Figure 37A), which were successfully coated (Figure 37B). The cores in this case had a diameter of  $12 \pm 2$  nm and were synthesized by coprecipitation and coated by citrate. The silica shell was synthesized by the bi-phase method and had a diameter of  $8 \pm 2$  nm. These particles were very stable which is mostly due to their small size and following from this their superparamagnetism. When we increased the particle size to larger



particles their magnetic moments quickly became so large that only clusters were coated. Another interesting observation in the cryo-TEM image is that the PNIPAM particles show roughly the same size of about 100 nm, regardless of the number of particles incorporated into the shell. Besides the coated particles there are also some free polymeric particles visible, which could either be leftover monomer or small polymer droplets. After all the polymerization was still done in a rather uncontrolled free radical fashion, so some irregularities in the product are expected. This is of course a problem caused by the concentration of the magnetite particles, however when the concentration is increased this also favors the agglomeration of the particles.

We took 3D-tomography images to determine whether the particles were coated or whether they mainly stick to the surface of the PNIPAM microgel droplets (Figure 37C). These demonstrated that the particles are indeed inside the microgel, whether they are also covalently bound or mainly encapsulated cannot be determined by this method. We can, however, with certainty say that the coating step was successful in producing a magnetite PNIPAM hybrid material.

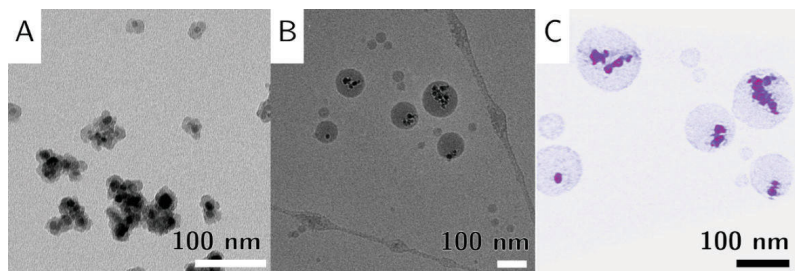


Figure 37: From particles to the gel. (A) TEM image of magnetite particles coated with a silica shell. (B) Cryo-TEM image of the silica coated particles in a shell of PNIPAM crosslinked by BIS and functionalized with AA. (C) 3D-tomography image rendered from a tomogram of the particles in B.

In the next step we investigated the properties of this new hybrid material. The magnetic as well as the thermoresponsive properties were investigated. The thermoresponsive properties were tested by dynamic light scattering (DLS). Here, we could determine the ability of the composite to undergo the PNIPAM typical phase transition at 32 °C, as well as the reversibility of this transition

(Figure 38A, B). We show here that the gel switches from an initial radius of 130 nm in the swollen state to a radius of 105 nm in the shrunken state. The transition is not instant as is typically the case for pure PNIPAM but is smeared over a broader temperature. A possible cause for this is the distribution of BIS and AA as it could have a significant effect on the LCST, by changing the solubility of the system. Another effect to keep in mind is the decreased penetration depth of water into the system due to its tightly crosslinked nature. This leads to a different solvation environment for NIPAM species near the core of the microgel, they are screened from most water molecules, compared to NIPAM molecules with a complete hydration shell on the outside of the microgel. The amount of hydration follows a gradient from the outside of the gel to the inside, which explains a gradual phase transition.

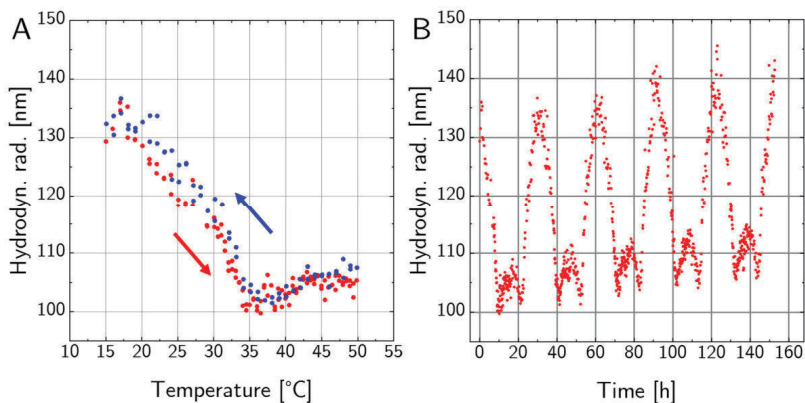


Figure 38: Temperature responsiveness of a hydrogel with magnetic cores. (A) LCST transition of a hydrogel measured with DLS (B) Reversibility of the hydrogel transition across five cycles spanning six days.

The slope of the radius reduction increases around 30 °C, the particle radius undergoes a minimum around 35 °C at 100 nm and then dips up a little to 105 nm. The behavior can be explained by the rearrangement of the PNIPAM chains and similar behavior was already investigated in a paper published in *Gels* in 2017 by our group.[155] The reason for this is a change in the crosslinker density, there is a gradient in concentration from the surface of the silica coated core to the outside of the microgel. This gradient leads to the formation of a strongly crosslinked

PNIPAM layer on the surface of the silica coated particles and to the formation of long chains to the outside of the particles, which are mostly elongated to maximize their surface area below the LCST. When the temperature is increased the long chains shrink back to the surface of the particles to decrease their surface area. The collapsed chains on the surface of the microgels form a rough layer that later rearranges which increases the radius again. The PNIPAM microgel droplets in the TEM appear polydisperse in size, this means they deviate quite a lot in molecular weight and possibly even in chemical makeup.

This shows that the addition of particles to the PNIPAM system leaves the thermosensitive behavior of the polymer matrix intact. This behavior is also reversible over several cycles. We tested that by repeated heating and cooling cycles with constant measuring over the course of a week (Figure 38B). The radius showed the same transition of a  $\Delta R$  of about 30 nm across 5 cycles. Small aggregation effects are visible through the increase in maximum and minimum radius of about 5 nm over the course of a week. The magnetization measurement shows a very low magnetization of 6 kA/m at 2.5 T, which is about 1.5 % of the magnetization of the pure particles, which is at 398 kA/m (Figure 39). However, this assumes the density of magnetite for the whole sample volume, more accurate is the comparison between the mass magnetization. Here the particles show a magnetization of 76 Am<sup>2</sup>/kg while the gel is at 0.03 Am<sup>2</sup>/kg. This makes for a proportion of magnetic material of 0.04 percent, deviations are to be considered due to the inaccuracy of the weighing process for these small masses. Elemental analysis substantiates this analysis. The gel was chemically digested by HNO<sub>3</sub> and HClO<sub>4</sub> and the iron content was determined to be 0.036 %  $\pm$  0.001 of the whole hydrogel at the given concentration. This also substantiates the use of VSM measurements to determine the iron content of a material. The gel shows no measurable hysteresis, the superparamagnetic effects of the particles are preserved in the gel. The magnetization curve shows a slope at 2.5 T; to saturate the magnetic moments, higher field strengths are required. This is an effect often observed in ferrofluids.[89]

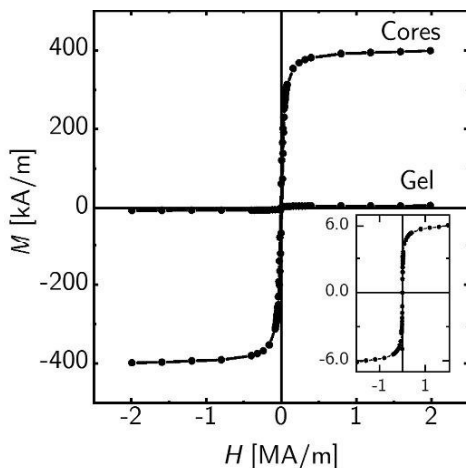


Figure 39: Magneto responsiveness of a hydrogel with magnetic cores. The magnetization of the gel compared to the magnetization of the raw particles; an enhanced image of the raw magnetization curve is shown in the insert. The gel has a saturation magnetization of 6 kA/m while the particles are at 398 kA/m.

#### 4.4.1.2 Macrogel

The microgel particles carry a primary amine function on the surface, introduced by the allylamine during the synthesis. The amine functions of the single microgel particles can be crosslinked by GA to form a macrogel, which consists of one giant gel network. This network shows similar thermo- and magneto-responsivity as its microgel counterpart. The main difference is in its flow behavior and thereby in its effects on the particles trapped in the matrix. The flow or rheological behavior was measured in a plate-plate geometry that could be magnetized up to a field strength of 777 mT. We measured the microgels as well as the macrogels in this setup, but the microgels were not distinguishable from water in their behavior, since more than 95 % of the micro-hydrogel consists of water. We put an emphasis on the gel-like properties of the composite materials, so we measured their behavior under shear strain. The speed of the gelation is dependent on the temperature. If GA is added at room temperature, the gelation process is very slow and, in most cases, we did not observe visible gelation at all. When GA is

added above the LCST of PNIPAM the gelation happens almost instantaneously. This is likely related to the position of the amine functions inside the microgel particles. When the gel is below the LCST the amine groups are inside the random coil formation. They can be at the outside of the microgel and get crosslinked, but with the same or a higher probability they are on the inside of the particle and attached GA is unlikely to find the amine function of another microgel particle to bind to. When the LCST is crossed and the phase transition is completed the hydrophilic parts of the network are turned outside, all the amine functions are on the outside of the microgel droplets and can be crosslinked to other droplets. Additionally, a higher temperature leads to faster diffusion and more microgel droplets meeting. For the oscillatory shear experiments the hydrogel was stirred for 15 minutes after the addition of GA to ensure complete gelation. In Figure 40 we present the rheological analysis of a macrogel that showed typical behavior for a PNIPAM hydrogel.

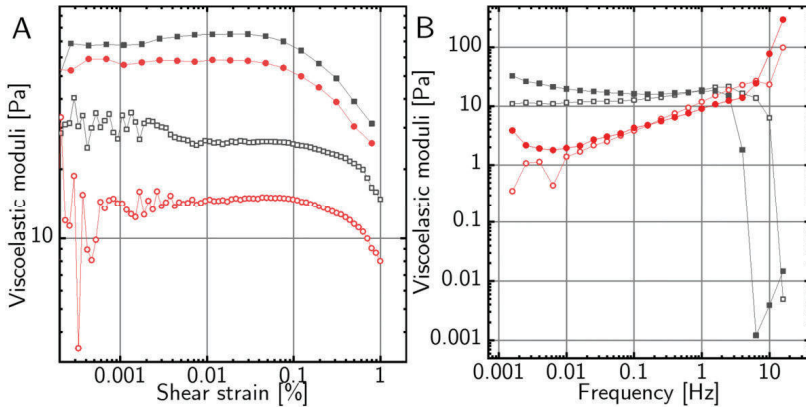


Figure 40: Rheological studies of a macrogel with magnetite particles. (A) Amplitude sweep of the gel after crosslinking at a frequency of 1 Hz with an applied field of 777 mT (full symbols) and without (empty symbols). The black symbols depict  $G'$  and the red symbols depict  $G''$  (B) Frequency sweep at a shear strain amplitude of 3 % after crosslinking of the gel with an applied field of 777 mT and without.

The behavior under shear strain was first tested by increasing the strain amplitude. The moduli at very low amplitudes can be disregarded as errors produced by the measurement setup. At an amplitude of 0.004 % both  $G'$  and  $G''$

display roughly constant values. When the strain is further increased the gel leaves the LVER and both moduli diminish in a regime which is called the non-linear viscoelastic regime.  $G'$  being higher than  $G''$  across the whole LVER is a good indicator for gel-like behavior, as more energy is stored in the elastic system than lost by viscous dissipation. The overall values for the viscoelastic moduli in this measurement are very low when compared to other hydrogels,[156] which is to be expected since we observe a highly swollen system underneath the transition temperature. Our values are about two magnitudes lower than other reported hydrogels. When the magnetic field is switched on, we observe a small but noticeable increase in the viscoelastic moduli. Also, the onset of the nonlinear regime is shifted to slightly lower strain amplitudes. Here the magnetic particles seem to have a slight hardening effect on the hydrogel once the magnetic field is switched on.

We also performed oscillatory tests where the strain amplitude was fixed and the shear frequency varied. This test was done to get information about the time dependent properties of the hydrogel. The viscous moduli show a crossover at high frequencies, at this point the character of the hydrogel changes from a liquid-like behavior to a gel-like behavior. This means that the gel will act like water to quick deformations but is stable against slow deformations. Towards lower frequencies both  $G'$  and  $G''$  decline, which means that the crosslinking degree is low. The values of  $G'$  are constantly higher than 10 Pa, this indicates a low amount of gel-stability. In this measurement there was no significant difference between the measurement with and without an applied field, except around very low frequencies which is unreliable for these samples at best. We conclude that, while the magnetic particles show some effects on the gel rigidity in the amplitude sweep, their magnetic properties have no effects on the gel-stability.

The particle load for this hydrogel at 0.04 % based on VSM measurements is quite low which is based on the need for low concentrations to prevent agglomeration. The method of starting from a core with subsequent sheathing with silica and the polymer shell, naturally adds a lot of non-magnetic material to the particles which reduces the magnetization of the composite material. Nevertheless, by applying a field we were able to significantly change the rigidity of the gel, showing that it is indeed magneto responsive. To increase the particle load we also did some research into hydrogels where the magnetic particles are rather loosely connected to the hydrogel by physical adsorption to achieve a higher particle load.

#### 4.4.2 Loosely connected macro-hydrogel

This hydrogel does not rely on covalent bonds to interact with the particles, but rather traps them by forming a dense network. This entrapment is meant to hinder the particles in their movement. The degree of hindrance can be influenced by different factors, namely by the crosslinker density, to form tighter or looser networks, or by the size of the microgel beads that are crosslinked together. The crosslinker density could be varied the easiest by changing the amount of GA in the system. The method was adapted from the work by Nack and we could successfully reproduce the results, leading to three different gels (Figure 42).[42] The degree of crosslinking was set to  $\chi = 0.1, 0.05$  and  $0.025$  with:

$$\chi = \frac{n_{GA}}{n_{GA} + n_{PNIPAM}} \quad (34)$$

This was done to create networks with decreasing density. The size of the crosslinked gels was determined by DLS (Figure 41). The maximum and minimum radius as well as the LCST were fitted from the obtained data using the following equation:[157]

$$R = \frac{R_{\max} - R_{\min}}{1 + \exp((T - LCST)/k)} + R_{\min} \quad (35)$$

Here  $R_{\max}$  is the radius at the maximum at low temperatures,  $R_{\min}$  is the minimum radius at high temperatures accordingly. LCST here is defined as the temperature where the hydrodynamic radius is decreased by 50%. The parameter  $k$  defines the width of the transition, a small  $k$  defines a narrow temperature area of the transition.

The only difference between the gels was the amount of GA added to the systems, the amount of PNIPAM was kept constant. All gels show the PNIPAM specific LCST around  $30^\circ\text{C}$ , this does not seem to be influenced by the amount of crosslinker in the system. The transition is reversible and shows only a slight hysteresis in the transition temperature. The minimal radius varies between 100 nm and 150 nm, while the maximum radius shows variation between 300 nm and 483 nm (Table 2). The maximum radius is expected to show larger fluctuations, because the PNIPAM chains are elongated and variations in chain length that appear due to the free radical polymerization have a larger influence. From the maximum and the minimum radius we can determine the swelling degree  $a$  by:

$$\alpha = \frac{R_{\min}^3}{R_{\max}^3} \quad (36)$$

When the degree of crosslinking is increased,  $\alpha$  normally decreases, because the crosslinking prevents the PNIPAM chains from fully elongating below the LCST. The changes we observe in  $\alpha$  are most likely random fluctuations caused by the free radical polymerization and can be disregarded.

Table 2: Parameters extracted from the fits for the gels at three different crosslinking degrees in Figure 41.  $K$  defines the width of the transition and  $\alpha$  is the swelling degree.

| $\chi$ | $R_{\max}$ [nm] | $R_{\min}$ [nm] | $LCST$ | $k$  | $\alpha$ |
|--------|-----------------|-----------------|--------|------|----------|
| 0.1    | 295             | 99              | 31     | 1.2  | 0.038    |
| 0.05   | 483             | 150             | 31     | 0.51 | 0.030    |
| 0.025  | 384             | 115             | 31     | 0.65 | 0.027    |

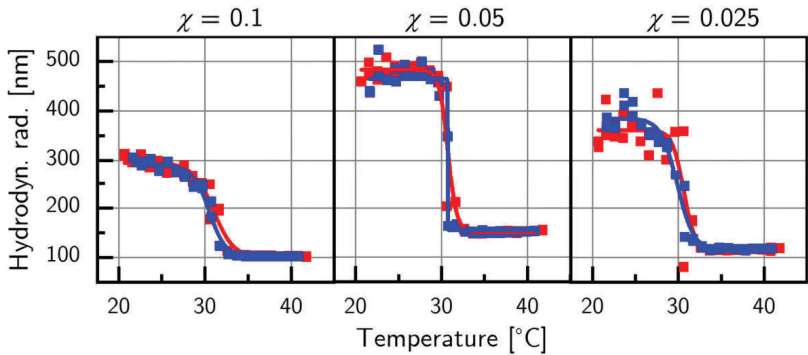


Figure 41: Comparison of the temperature dependent behavior for the three differently crosslinked gels at  $\chi = 0.1$ , 0.05 and 0.025. The curve upon heating is depicted in red, the curve upon cooling is depicted in blue.

Another aspect to keep in mind is the varying concentration of crosslinker, since the crosslinker keeps the linked chains from fully extending. Due to the



random nature of the polymerization it is hard to determine the influence of the crosslinker amount on the size of the microgel beads, as it does not appear to change in a predictable way.

In the TEM images (Figure 42) the influence of the crosslinker is visible. The network with the highest amount of crosslinker is bound together so tightly, the microgel beads seem to grow together. The network with the lowest amount of crosslinker appears to be not crosslinked at all. When looking at the TEM images one must keep in mind that these are not cryo-TEM images, so they do not display the true behavior in an aqueous solution but serve mainly as a first hint. Since the samples are dried before they enter the TEM column the water evaporates and the closest the solvated hydrogel gets to this state is in the collapsed state. This drying of the sample is irreversible, and the radius of the dried sample should not be compared to the radius obtained by DLS.

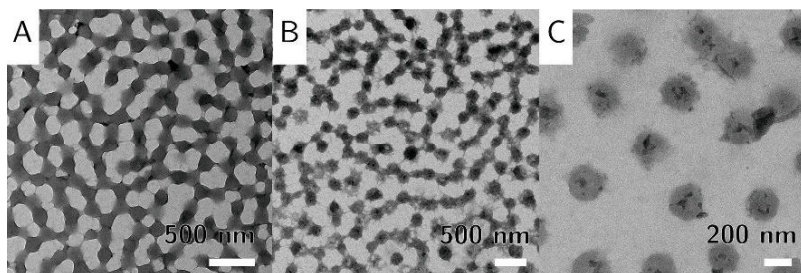


Figure 42: Three hydrogels made from PNIPAM and GA. The degree of crosslinking was varied from (A)  $\chi = 0.1$  over (B)  $\chi = 0.05$  to (C)  $\chi = 0.025$ .

We did oscillatory shear tests and measured the answer of the gels in a similar way to the experiments done on the covalently bound gels (Figure 43). We observed that the viscoelastic moduli increased when the crosslinking degree  $\chi$  is reduced, indicating a stronger gel. The end of the LVER does not seem to be influenced by the crosslinking degree, for the samples with  $\chi = 0.1$  and  $0.05$  the value is at around  $0.053\%$  shear deformation, for the sample with  $\chi = 0.025$  the value is at  $0.072\%$  shear deformation, which can be ascribed to the uncertainty of the measurement. For all samples, the storage modulus is higher than the loss modulus in the full LVER range, so the gel-like character of the samples is observed. Interestingly the crossover between storage and loss modulus seems to

shift to higher values when the degree of crosslinking is reduced, which could indicate a more gel like character for the less crosslinked sample.

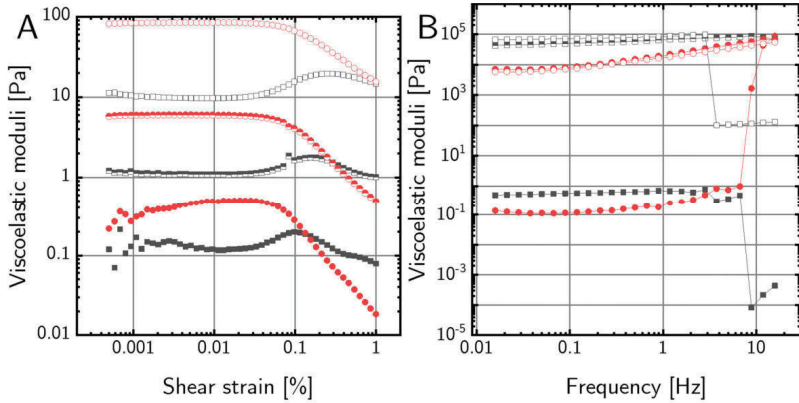


Figure 43: Oscillatory shear tests of three gels with a different crosslinker degree. (A) Amplitude sweeps at a fixed frequency of 1 Hz. (B) Frequency sweeps at a fixed deformation of 1%. The black symbols show the storage modulus, while the red symbols show the loss modulus. The full symbols show the gel at  $\chi = 0.1$ , the half full symbols show the gel at  $\chi = 0.05$  and the empty symbols show the gel at  $\chi = 0.025$ .

The frequency sweeps reveal a similar behavior in comparison to the amplitude sweeps, as the viscoelastic moduli also increase with decreasing crosslinker content in the gel. Here the gel with a crosslinking degree of 0.1 shows very low moduli around 1 while both other gels show moduli several orders of magnitude larger. The gels at crosslinking degrees of 0.1 and 0.025 show a crossover of the storage and loss modulus at higher frequencies and after that the moduli run parallel. This behavior means that at fast frequencies so at fast movements the gel-character of the sample is not persistent, while at slow deformations the gel-character is preserved. The sample with a crosslinker degree of 0.05 does not show non-gel-like behavior. The light slope coming from higher frequencies to lower frequencies with a plateau at the very low frequencies is typical for weakly crosslinked hydrogels.[135] The low viscoelastic moduli of the highly crosslinked gel is likely connected to the low wt% of this sample of just 1.2 % polymer in the sample. The other gels were way more concentrated at 4.7 and 7 wt% polymer, which makes conclusions drawn from the comparison of these gels unreliable.

Almost as easy as changing the crosslinking degree is the regulation of the size of the microgel beads.[158] Since PNIPAM gets largely insoluble in water above its LCST and the reaction happens at 60 °C, about 30 °C above its LCST, the growing chains need to be stabilized. The hardly soluble PNIPAM forms droplets in the aqueous reaction medium and these droplets were stabilized by an emulsifying agent. The emulsifying agent was SDS and by varying the amount of SDS we could easily achieve a wide range of possible microgel bead sizes crosslinked into a macrogel, by varying the size of the PNIPAM droplets. The characterization of these gels was done mostly by DLS to determine their size and by oscillatory rheology tests to determine their viscoelastic properties.

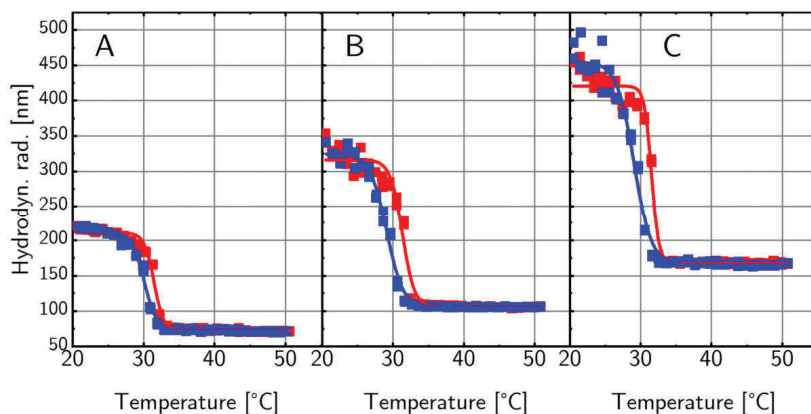


Figure 44: Three gels with different sizes analyzed with regard for their LCST behavior. (A) 0.557 mol/L SDS (B) 0.215 mol/L SDS (C) 0.0344 mol/L SDS

The DLS showed that the LCST stays reliably around 31 °C regardless of the size of the microgel, here shown exemplarily for three different SDS concentration 0.557 mol/L, 0.215 mol/L and 0.0344 mol/L (Figure 44). All the syntheses were done with a crosslinker density of GA of about 0.025.

The size of the microgel changed mainly in the radius below the LCST, here we tuned the size from roughly 200 nm to about 500 nm by changing the SDS concentration between 1.1 mM and 6.8  $\mu$ M. The  $\alpha$  stays at roughly the same value of  $0.044 \pm 0.009$ , which is to be expected since the ratio of GA : NIPAM stayed constant. The radius above the LCST was subject to less change, at a temperature

of 45 °C we managed to tune the hydrodynamic radius between 70 nm and 170 nm (Figure 45). The radius above the LCST follows roughly an inverse exponential behavior compared to the amount of SDS employed in the reaction.

The reason for the decreased change of the radius above the LCST is the difference between an elongated chain and the same chain compressed to a tiny globule. While an increase in chain length will directly increase the hydrodynamic radius below the LCST at an almost equal amount, an increase in chain length does almost nothing for the volume of the collapsed globule above the LCST.

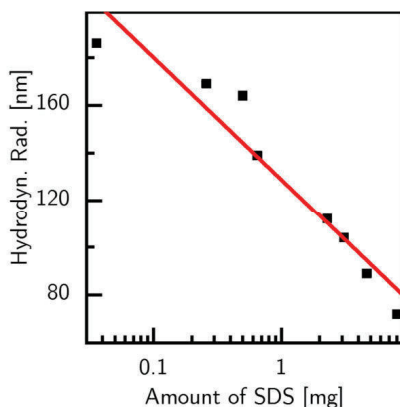


Figure 45: The hydrodynamic radius at 45 °C changes above the LCST in the collapsed state with the amount of SDS employed in the reaction.

Next, the flow behavior of three of these gels under shear stress was studied. This gives a good approximation for the damping the hydrogel can exert on the movement of the particles later trapped inside its meshes. The rheological measurements were done with the same aspects in mind as the tests on the covalently bound gel (Figure 46). The small gel showed a very strong increase in its viscoelastic moduli. The medium sized gel and the large gel show high moduli even at room temperature. The boundary of the LVER has a tendency towards lower amplitudes when the temperature is increased to 40 °C. For the sake of clarity, the values for the loss modulus were omitted in Figure 46 but all values were constantly below the values of the storage modulus  $G'$ , so the gel-like character of all gels was confirmed by the measurements. When the values of  $G'$  within the LVER below the LCST (blue symbols) are compared, it becomes clear

that the gels increase in rigidity as the size of the crosslinked microgel spheres increases. For the samples above the LCST (red symbols) this trend is preserved.

Except for the small gel at room temperature all gels show the characteristics of strongly crosslinked polymer-gels in tests with a fixed amplitude and varied frequency. The storage modulus is almost constant over a large frequency area. Only at very low frequencies a slight tendency towards higher moduli is visible in the gel. We determined the entanglement molecular weight  $M_e$  by using the MIN-Method described in the theory section (3.1.5), [159] the values are listed in Table 3.

Table 3: Three PNIPAM/GA gels with different microgel sizes compared below and above the LCST. The temperature of 22 °C amounts to room temperature. The hydrodynamic radius was fitted from DLS measurements, the concentration was determined by gravimetry, the end of the LVER was approximated based on the amplitude sweep and the  $M_e$  was calculated based on equation (31).  $\alpha$  is the swelling degree, determined by equation (36).

| Sample                | $R_{hyd}$<br>[nm] | Concentration<br>[wt%] | End of<br>LVER<br>[%] | $M_e$<br>[g/mol] | $\alpha$   |
|-----------------------|-------------------|------------------------|-----------------------|------------------|------------|
| Small gel @<br>22 °C  | 212               | 3.64                   | 4                     | 148000000        | 0.039<br>± |
| Small gel @<br>40 °C  | 72                | 3.64                   | 0.5                   | 49200            | 0.002      |
| Medium gel @<br>22 °C | 324               | 2.93                   | 2.2                   | 105000           | 0.033<br>± |
| Medium gel @<br>40 °C | 104               | 2.93                   | 0.7                   | 25600            | 0.003      |
| Large gel @<br>22 °C  | 442               | 4.00                   | 1                     | 22100            | 0.052<br>± |
| Large gel @<br>40 °C  | 165               | 4.00                   | 0.7                   | 16700            | 0.005      |

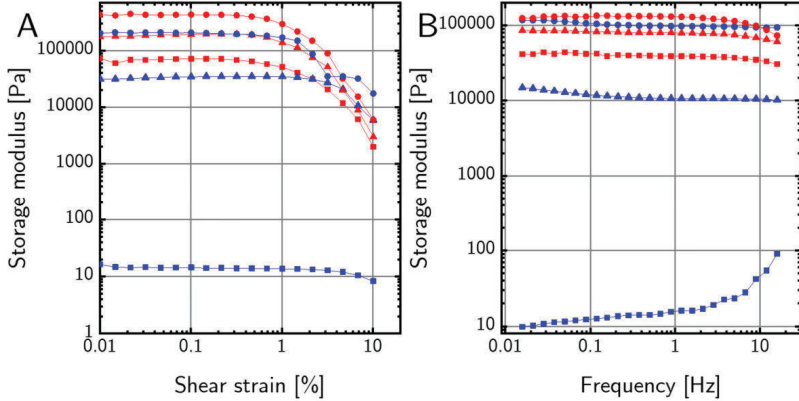


Figure 46: Rheological investigation of three different sized hydrogels. (A) Amplitude sweep for the three gels. (B) Frequency sweep for the three gels. Blue depicts the data at room temperature, red depicts the data for 40 °C. The square symbols depict a small 212 nm (74 nm above LCST) gel, the triangles a medium 324 nm (104 nm) gel and the circles a large 442 nm (165 nm) gel. The loss modulus is omitted here for the sake of clarity.

The entanglement molecular weight decreases when the temperature is raised above the LCST, for all samples. This makes sense because when the gel shrinks the entanglement points move closer to each other and the average distance and molecular weight between them decreases. This was also shown in a SAXS measurement (Figure 47). We measured a concentrated sample of a small gel at room temperature and compared it to its diluted gel sample (Figure 47A).[160] By dividing the intensity through the formfactor we were able to obtain the structure factor. The position of the first maximum of the structure factor determines the nearest neighbor distance  $D_{NN} \left( = \frac{2\pi}{Q_{\max}} \right)$  which was about 296 nm (Figure 47C). At 45 °C there was no structure factor (Figure 47B), because the particles are in the swollen state and the volume concentration decreased, so they don't have any particle interaction anymore. The particle form factor can only be observed in the case of the diluted sample in Figure 47A. From these curves we also fitted the radius using the form factor of a sphere weighted with a Schulz-Flory distribution by looking at the first minimum and got 151 nm in the swollen state and 73 nm above the LCST, which is in good agreement with the data obtained from DLS (see Table 3), since the SAXS measurement does not include the hydration shell which is very pronounced at 20 °C and very small at 45 °C.[160]

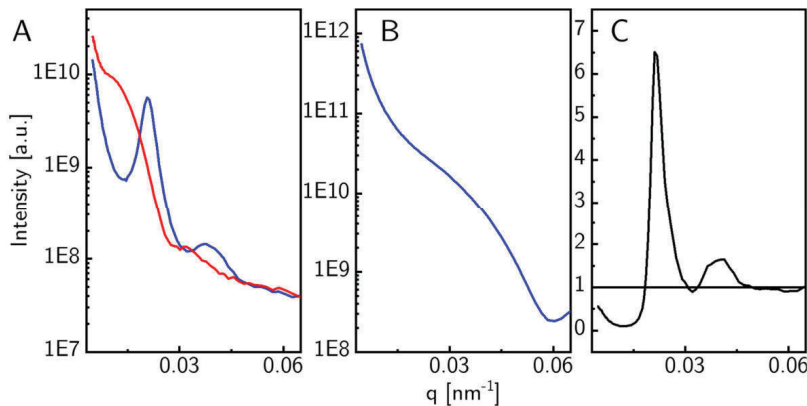


Figure 47: SAXS curves of the small gel at room temperature and at 45 °C. (A) The curve for a concentrated sample compared to the curve for a diluted sample at 20 °C. The concentrated curve is depicted in blue, the diluted curve in red. The sample was diluted to measure only the formfactor. (B) The concentrated sample at 45 °C. (C) The structure factor obtained from dividing the form factor in (A) by the concentrated curve.

Furthermore, there is a decrease in  $M_e$  when the size of the gel is increased. This effect is visible at room temperature as well as at 40 °C, which means it cannot be solely attributed to the different concentrations of the hydrogel samples, as above the LCST all water is pressed out of the system and the properties solely depend on the gel. A possible explanation is that larger gels have more entanglement points than smaller gels, which is likely the case because the PNIPAM chains are longer and thus have more opportunities to entangle. A larger number of entanglements per chain also explains the increased moduli measured for larger hydrogels. The difference in  $M_e$  between gels over and under the LCST seems to decrease when the gel is larger, which can also be explained by an increased number of entanglements, which makes for a more stable distance between entanglement points, as each entanglement point is supported by several others.

Unfortunately, the magnetic response of loosely connected hydrogels mixed with magnetite could not be measured because in the rheology setup a gradient field is applied. Only the bottom plate of the measuring device is magnetized so the particles precipitate since they are not tightly bound to the hydrogel network.

For hydrogels mixed with goethite no reaction was observed on application of the magnetic field, it is likely that the particles would orient at a field of 777 mT, but this did not affect the rheological properties. The orientation can however be measured in a scattering experiment, as was done for the pure particles and repeated for composite hydrogels at the DESY facility.



## 4.5 Particle orientation and dynamics of particles trapped in a hydrogel

The orientation of pure particles was described in detail in section 4.2.3 and the goal in this section is to see whether these findings carry over to particles trapped in a loosely connected hydrogel matrix. To study the orientation of the particles we used the ultra-small angle X-ray scattering (USAXS) setup at the coherence applications beamline P10 at the DESY facility. Here it was possible not only to measure the static behavior of the sample, but also to measure the dynamics of the particles in the network. To compare their matrix interactions we wanted to investigate the three goethite samples discussed in chapter 4.2.2 within differently sized gels. However, the time slot allowed for only one detailed study. Since the small goethite nanorods of 210 nm orient at small field strengths we focused on this particle system. The idea was to compare the dynamics of the particles trapped in an increasingly large hydrogel matrix, with the length of the nanorods being in the same dimension as the microgel size. The most important factor when comparing the matrix materials was the difference in viscosity, as the viscosity increased with rising gel size. Ultimately, due to the limited timeframe available for the experiment, two systems will be shown here, one with short 210 nm goethite nanorods mixed into a small 212 nm radius hydrogel and one with a medium 324 nm radius hydrogel (the gels were discussed in 4.4.2). The measured systems were investigated in a coil setup providing a continuous magnetic field between 0 and 90 mT and in a permanent magnet setup with available fields of 155, 230, 470 and 555 mT. Additionally, we were able to adjust the temperature during each measurement, so the change in dynamics above the LCST of the hydrogel could also be investigated. Details about the setup are shown in section 3.1.6.

### 4.5.1 Particle orientation within the gel network

For any static scattering experiment it is first important to rule out any effects that might be caused by damage that occurs in the sample due to exposure to the powerful X-ray beam. For this reason, the sample was moved after each measurement to have a fresh sample region. Additionally, a precautionary measure to prevent beam damage is to insert silicon wafers into the beam path to absorb some of the X-ray power and so reduce the intensity on the sample. Beam damage was evaluated by taking a quick 0.01 s exposure picture series and

evaluating for eventual streaks or changes in the measured radial average intensity of the sample over time. Any sample regions with streaks or changes were disregarded.

As described above, samples were measured at different field strengths and temperatures to evaluate their orientation. The scattered pattern shows the orientation of the sample and the averaged radial intensity was evaluated at different wavevectors  $q$  (Figure 48).

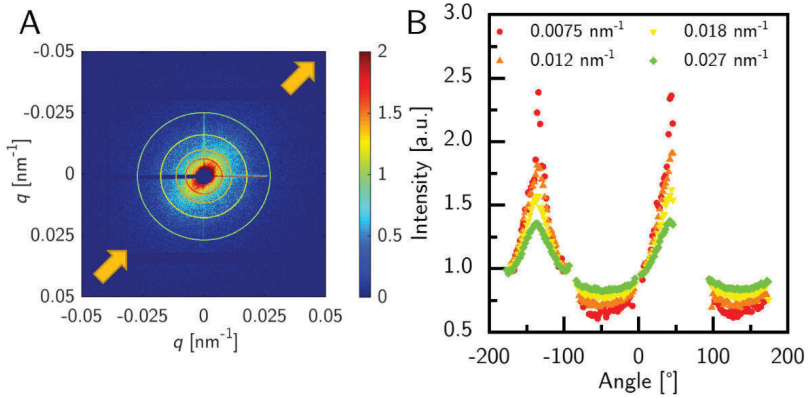


Figure 48: (A) A typical scattering pattern. The rings around the beamstop indicate the radial intensities at the analyzed  $q$  values which are shown in (B). The colors of the scattering pattern depict the intensity as indicated by the color bar. (B) The averaged radial intensities for each  $q$  values depicted in (A). The angle  $0^\circ$  is set to the  $x$ -axis on the detector and the scale proceeds counterclockwise. Missing values stem from masked regions on the detector (mask not shown here for clarity). The image was taken at room temperature with an applied field of 230 mT acting on small 210 nm nanorods in a small gel. The direction of the magnetic field is depicted by the yellow arrows.

Since the intensity decays rapidly over  $q$  only  $q$ -values close to the beam stop were evaluated. The intensity distribution around the beam stop shows some gaps where the image on the detector was masked. Masking is necessary because apertures in the beam path also scatter X-rays leading to signals that do not stem from the sample, which should be disregarded. In Figure 48A the mask shown in dark blue is the one covering the beam stop itself. Starting from the center a cross with increased intensity is visible that extends on the  $x$  and  $y$ -axis. This cross

stems from the slits used to adjust the size of the X-ray spot on the sample and was masked out to gain accurate results (the mask is not shown here for clarity). To analyze the particle orientation, we calculated the radial intensities for different wavevectors (Figure 48B). Due to the mask the intensities at some angles are missing. Here the small 210 nm nanorods in a small gel were measured at a field strength of 230 mT. The particles align with the long axis perpendicular to the field, visible in the two maxima of the intensity around  $-135^\circ$  and  $45^\circ$ . The scattered pattern is rotated when compared to the images shown before, because the magnet setup is tilted by  $45^\circ$  (compare the image in section 3.1.6). The increase in intensity means that the minimum of the scattering pattern moves to larger  $q$  values, so to smaller particle sizes which makes the short axis visible at  $-135^\circ$  and  $45^\circ$  and the long axis at  $-45^\circ$  and  $135^\circ$ .

I will now describe the general procedure used to evaluate each measurement. As an example, I will take the data of the small nanorods in a small gel, where we see strong alignment with an applied magnetic field of 230 mT. Like in the case of pure particles we can extract the maxima and minima of the peaks at  $45/-135^\circ$  and  $45/135^\circ$ , respectively. The relative degree of orientation was extracted simply by subtracting the maximum value of the intensity from the minimum, while the position of the minimum could be used again to derive the nematic order parameter or the Herman orientation function (see theory section 3.1.6). Since the experiments in the permanent magnet setup happen exclusively in the strongly oriented domain the nematic order parameter was at its maximum of one across the whole region and thus omitted.

From our previous experiments with the pure goethite nanorods we expected only weak if any alignment of samples measured in the coil setup, because 90 mT were barely enough to orient the shortest nanorod sample. Therefore, the main analysis of the orientation dynamics happened in the permanent magnet setup where the orientation is clearly visible. For the small gel we did a full temperature sweep at 555 mT, for the large gel and other field strengths we only measured at room temperature ( $20^\circ\text{C}$ ) and above the LCST ( $45^\circ\text{C}$ ).

The orientation degree varies strongly with field strength and temperature, since both parameters influence the ability of the nanorods to orientate (Figure 49). The first thing to note is that the small gel allows for a stronger particle orientation at the given field strength compared to the medium gel which is not surprising given its lower rigidity (shown in the previous section in Figure 46). As mentioned above the sample shows only a very low orientation degree at field strengths below 100 mT. After the low field strengths were measured in a coil setup, the high field strengths were measured in the permanent

magnet setup. We measured the particle gel systems from high to low field strengths, so we started with the highest field strength of about 555 mT, followed by 470, 230 and 155 mT.

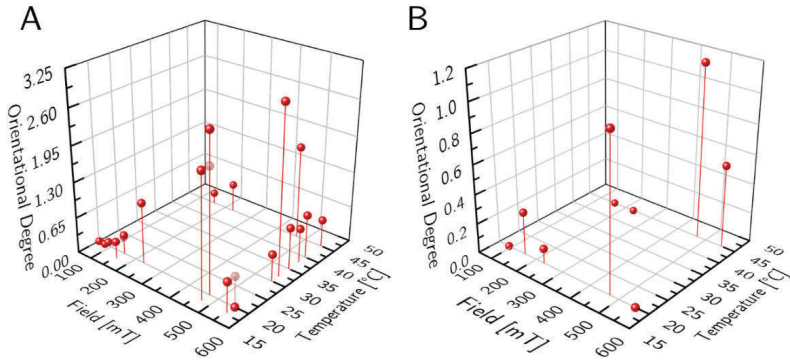


Figure 49: Orientational degree of a small 210 nm goethite nanorod sample embedded in two different hydrogels across varied field strengths and temperatures. (A) Nanorods in a small 212 nm hydrogel. The transparent symbols depict measurements that were taken, after the sample finished a temperature cycle and was cooled to 20 °C again. (B) Nanorods in a medium sized 324 nm hydrogel.

Interestingly enough, we observed no orientation at 20 °C, but once the temperature was increased to the LCST we observed that the particles orient. The nanorods began to rotate as soon as the phase transition started at 30 °C and reached a local maximum in orientation degree when the transition was completed at 35 °C. After that the orientational degree decreases when the temperature is increased to 45 °C. This degree of orientation is maintained when the sample is cooled down to 20 °C. These findings carry over to the medium hydrogel, where the same tests were done but with a less detailed analysis. The trend of no orientation at room temperature followed by orientation after crossing the LCST is preserved, indicating a robust result. After the highest field strength was measured the magnets were moved further apart to decrease the field strength to 470 mT without changing the sample. Here we see a different trend: the orientation reaches almost the maximum value of the 555 mT series and decreases its orientation when the LCST is crossed again. For the medium gel, high

orientation is observed across the whole temperature range. After the two high field strength measurements the orientation is greatly decreased when lower field strengths are applied, similar to the behavior observed in the pure particle sample. We observe a similar trend in the change of orientation in both samples, as the orientation decreases when the phase transition is finished and increases again when the threshold is crossed from the high temperature side.

When a fresh sample made of nanorods and hydrogel is introduced into a magnetic field at room temperature, we observed no orientation, even at the highest fields available. This leads to the assumption that the magnetic particles are firmly anchored and trapped in the hydrogel and at this temperature the matrix is too rigid for the particles to orient. When the temperature is increased up to the phase transition temperature of about 30 °C the change in the solvation state of the polymer chains changes and thus possibly also the interactions between the goethite nanorods and the hydrogels. On top of that the microgel particles shrink, which might allow the nanorods more freedom of motion. This is further supported by the fact that the sample achieves maximum orientation at 35 °C, so when the phase transition is complete. The hydrogel is in the shrunken state allowing the particles maximum freedom of motion. When the temperature is further increased the orientation declines, which could be caused by the thermal energy increasing the molecular motion, which possibly disrupts some orientational behavior. This assumption is backed up by the observed trend of decreasing orientation with increasing temperature for lower field strengths. When the temperature is decreased again to the starting point at 20 °C, we observe no change in orientation, leading to the further assumption that any orientation introduced at high temperatures is “frozen” below the LCST, since the particles cannot move in the rigid gel. When looking at the lower field strength results, we noticed a problem with the measurement procedure, which becomes obvious in hindsight. Since the particle/matrix composites are first subjected to the highest field strength, they might retain a great deal of orientation, even when the magnet setup is changed in between measurements, which further supports the thesis that the orientation is “frozen”. The orientation degree at 470 mT is the highest value observed in the experiment, although a stronger field should also orient more of the sample. This could be explained by effects leftover from 555 mT that were “frozen” into the sample. Nevertheless, we observe the same trend of decreasing orientation degree upon elevated temperature, with retained orientation when the temperature is decreased. This effect is consistent across the whole observed magnetic field range in the small gel. In the medium gel the particles are even more restricted in their orientation, visible in an overall lower orientational

degree. At 230 and 155 mT there is no visible orientation left at high temperatures. A possible explanation is that the hydrogel is too rigid at this temperature to allow particle movement.

The conclusion of the static orientational degree is that the matrix severely hinders the magnetic particles in their orientation, but its thermosensitive properties allow some movement during the phase transition. After the transition is finished the gels are very rigid and allow little movement of the particles. The orientation of the particles is “frozen” when the temperature is decreased, the particles are trapped in the matrix again.

#### 4.5.2 Particle dynamics within the gel network

The results so far could have also been obtained in a conventional SAXS setup, but to gain insights into the diffusion dynamics induced by particle orientation we need the additional information of coherence. We measured both slow dynamics by taking 600 images with 1 s integration time for each image and fast dynamics by taking 10000 images with 0.01 s integration time for each image.

The analysis then happens quite similar to that for a DLS experiment where  $g_1$  functions are fitted to gain access to the relaxation rate  $\Gamma$ , which then leads to the diffusion coefficient using the relation:

$$\Gamma = D q^2. \quad (37)$$

Utilizing the 2D detector we were able to access the  $g_2$  functions for selected  $q$ -values and for selected angles. This way we could compare the dynamics dependent on the field direction, we calculated the  $g_2(q, t)$  parallel to the field direction, perpendicular to the field direction and averaged for the whole ring (Figure 50). We observed that the dynamics for an oriented sample also diverge dependent on the orientation of the nanorods. The dynamics for an oriented sample at 555 mT (Figure 50A) for example show faster dynamics perpendicular to the field than parallel to the field. The sample is oriented perpendicular to the field at this field strength, but the short axis provides most of the scattered intensity. At 90 mT (Figure 50B) the dynamics are almost constant without a shift in relaxation time, due to the missing orientation at this field strength.

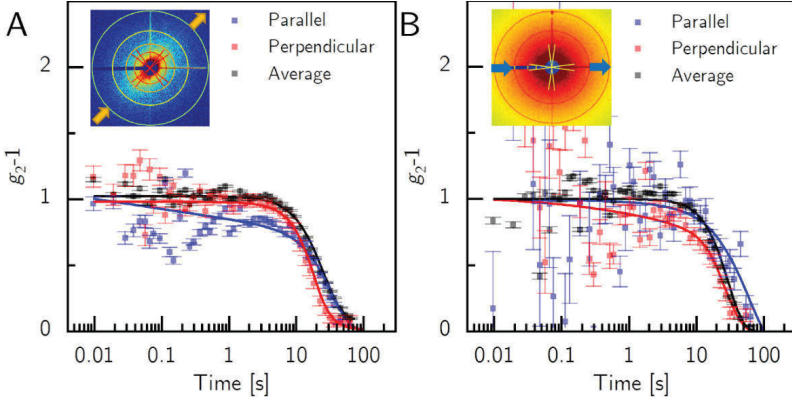


Figure 50: Examples for  $g_2$  functions for the 210 nm nanorods in a small 212 nm gel at one evaluated  $q$ -value of  $0.010 \text{ nm}^{-1}$  (A) at 555 mT and 20 °C and (B) at 90 mT and 20 °C. The curves were normalized and subtracted by one. The blue square symbols depict the direction parallel to the field, the red symbols the direction perpendicular to the field and the black symbols the average across the whole ring. The inserts show the scattering patterns with the direction of the magnetic field indicated by the yellow (blue) arrows.

From each fit of  $g_1$  we obtained a  $\Gamma$  which was averaged across all four angles for each  $q$  (Figure 51). Since  $\Gamma$  shows a linear dependence on  $q^2$ , the diffusion coefficient could be calculated by a linear fit using equation (37). It is obvious even without looking at the diffusion coefficient that for an oriented sample at 555 mT (Figure 51A) the diffusion should be influenced by the particle orientation. The slope for the curve showing the direction perpendicular to the magnetic field is steeper than the one parallel to the field, which mirrors the orientation of the particles with their long axis perpendicular to the field. This translates into a diffusion coefficient perpendicular to the field of  $D_{\text{perp.}} = 113 \pm 9 \text{ nm}^2/\text{s}$ , while the curve parallel to the field leads to  $D_{\text{par.}} = 61 \pm 5 \text{ nm}^2/\text{s}$  and the average  $D_{\text{ave.}}$  across all directions is at  $71 \pm 8 \text{ nm}^2/\text{s}$ . In theory  $D_{\text{ave.}}$  is equal to  $(2 \cdot D_{\text{par.}} + D_{\text{perp.}})/3$  for spindles or rods,[161] which is in good agreement with the measured data, e.g.  $(2 \cdot 61 + 113)/3 = 78 \text{ nm}^2/\text{s}$ , when the relative error is considered.

Particle diffusion in the same direction as the rod orientation is faster than perpendicular to it, which proves that the nanorods are well able to influence the matrix. For a sample with no or very weak orientation at 155 mT we observe

almost no variations in the diffusion coefficient for the different directions (Figure 51B). For  $D_{\text{par.}}$  we obtained  $362 \pm 16 \text{ nm}^2/\text{s}$ , for  $D_{\text{perp.}} = 353 \pm 27 \text{ nm}^2/\text{s}$  and on  $D_{\text{ave.}} = 300 \pm 32 \text{ nm}^2/\text{s}$ . These values present standard deviations large enough to assume no directed diffusion at these magnetic fields. The insert shows a clear direction dependent shift in the not normalized intensity indicating at least some orientation in the sample but this seems to be insufficient to influence the diffusion.

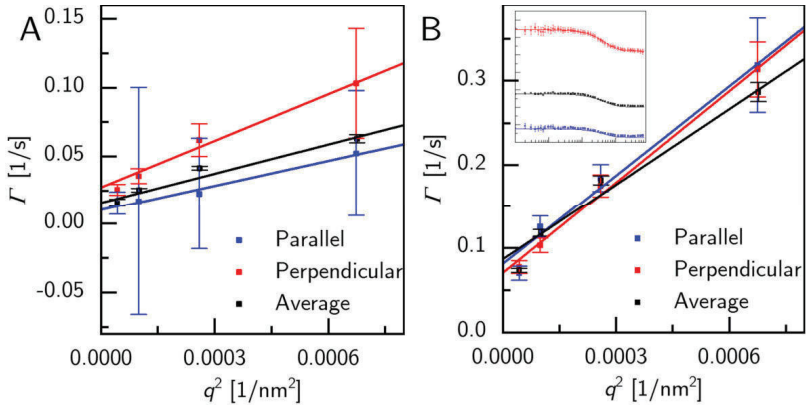


Figure 51: Diffusion coefficients from the fitted  $g_l$  functions versus the square of the wave vectors with linear fits, for different directions for a strongly oriented sample with small nanorods in a small gel (A) at 555 mT at 20 °C and (B) at 155 mT at room temperature. In blue the averaged diffusion coefficient parallel to the applied field, in red perpendicular to the field, and in black averaged over the whole ring are displayed. The insert in (B) shows the averaged  $g_z$ -functions against time at  $q = 0.010 \text{ nm}^{-1}$ , for (A) they are shown in Figure 50A.

Wherever possible we evaluated  $D$  dependent on the field strength and temperature (Figure 52.). Most dynamics at 45 °C in a small gel were too fast to be observed in the timeframe given by the experimental setup. It is thus reasonable to assume that diffusion at 45 °C is much faster than displayed in the graph for a small gel. The diffusion at low temperatures seems to be inversely proportional to the field strength, as the lower field strengths show higher  $D$ . It might be the case that the aligned particles open channels in the matrix during the phase transition which enable faster diffusion.

If we look at the same particles in the medium gel, we see that this gel provided overall more data points, because the matrix is more rigid and thus diffusion is



slower, even at 45 °C. The diffusion coefficients at 20 °C are again low at high fields with faster diffusion along the direction perpendicular to the field in good agreement with the directed diffusion observed for the small gel. The diffusion coefficients are comparable to the small gel. At high temperature, the diffusion at 555 mT can only be compared to the diffusion at 470 mT in the small gel, which is on a similar level, with faster diffusion along the nanorod orientation direction. At low field strengths and 45 °C diffusion is quite slow without a preferred direction.

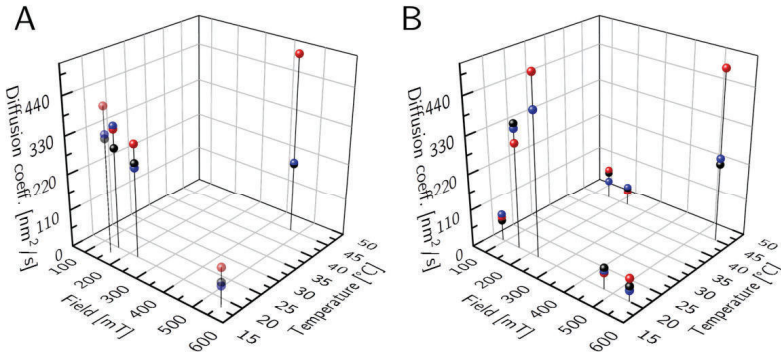


Figure 52: Diffusion coefficients and their dependency on field strength and temperature for small goethite particles in (A) a small 212 nm matrix and (B) a medium 324 nm matrix. The red spheres show the diffusion coefficient along a direction parallel to the field, the blue spheres along a perpendicular direction to the field and the black dots the average diffusion coefficient across the whole sample.

Although the sample dynamics were very fast and the statistics of the obtained results were often not good enough for meaningful interpretation, we managed to get enough data points for an at least preliminary assessment of the sample dynamics. We could show that diffusion in oriented samples is sped up along the orientation direction of the nanorods and slowed down perpendicular to the rod orientation. These results highlight the influence that magnetic particles have on their surrounding matrix, but also the influence the matrix has on the particles, by limiting their maneuverability.

## 5 Conclusion and Outlook

Iron oxide nanoparticles today are already used in many applications for example as catalysts or in medicine as contrast agents.[48,162] The anisotropic magnetic core of the multiresponsive hydrogel was realized in two ways: by synthesizing highly anisotropic, antiferromagnetic goethite and by synthesizing weakly anisotropic, ferrimagnetic magnetite.

A strong magnetic response was provided by the synthesis of ferrimagnetic magnetite particles. We started with reactions in batch that served well to establish working reaction parameters in the hydrothermal environment. We successfully produced small particles in the range of  $18 \pm 6$  nm using CTAB as a surfactant, but other surfactants were tried as well. Reactions using PEG as a surfactant are described extensively in literature, but we found insufficient phase purity to be a recurring issue with this approach, so it was ultimately abandoned. The synthesis of the magnetic particles could be improved by replacing the batch reactions by precursor-based reactions. The precursor of choice are akaganeite particles (the same as in the goethite synthesis). The precursor-based reactions were done exclusively in a hydrothermal reactor and after the initial parameters were evaluated the synthesis became highly reliable. Different surfactants were applied. With  $\text{Na}_2\text{HPO}_4$  we achieved one of the best results in terms of magnetic properties with a saturation magnetization of about 398 kA/m with a size of  $22 \pm 8$  nm. Notable is dopamine as a surfactant as this reliably produced samples that showed elongated particles with an aspect ratio of about 1.5 or 16/11 nm. The magnetic properties of the dopamine coated samples were slightly worse with a saturation magnetization of 273 kA/m, but it is likely the case because they were stabilized with PVP, so the magnetic content of the sample was likely overestimated based on gravimetry. It is notable that all samples show a negligibly small hysteresis, so we assumed superparamagnetic behavior. Low temperature measurements could further prove this assumption.

The synthesis of goethite was successfully reproduced from the literature provided by Lemaire *et al.*[18]; an aging procedure that took about 10 days, but the results were polycrystalline and had a broad distribution. We aimed to achieve a highly defined product by employing a precursor-based strategy, where an akaganeite precursor is transformed to goethite in a hydrothermal process. The reaction in a hydrothermal reactor proved to be faster, 4 hours compared to 10 days, and delivered a product that was tunable in size as well as in its field dependent

behavior. The product was less polydisperse than other examples in current literature, especially regarding reactions in water. It seems to be the nature of goethite to grow into acicular particles with a rather broad length distribution which our experiments also confirmed.[50] Nevertheless, we were able to synthesize particles that can be put into three categories: short rods around 210 nm, intermediate rods around 270 nm and long rods with lengths that range from 300 nm to 1  $\mu\text{m}$ . Interestingly the width of the particles is consistently around 30 nm. We showed in this work that the increased surface of these particles shifts the field strength necessary to provoke the goethite reorientation from about 85 mT to around 147 mT. This can be well explained by micromagnetic theory and is another good example for the surface influence in nanometric particles.[18] It furthermore highlights the straightforward tunability of the reorientation switch by the particle size.

The number of applications for nanoparticles will surely increase further in the future, but the problem of a reproducible synthesis path remains. It is often the case that results from one research group cannot be reproduced by another group.[38,39] However, there have also been positive examples where methods from multiple groups could be reproduced and compared in one laboratory.[29] I would like to believe that the number of well written and reproducible research articles will increase and help the field to grow, as I hope that this work provides easy pathways to reproduce the displayed results. An important factor for the further development of this field is also the emergence of new synthesis techniques. Microwave synthesis is an example of a high throughput method that got attention in the last couple of years that offers a different kind of heating and thus opens new synthesis pathways.[28] Another emerging technology is the use of microfluidic devices for particle synthesis.[163] This allows for easy screening of the synthesis process *in situ* while providing large quantities of product in a short time. The small size scales should enable a very high degree of control over the synthesis conditions, ultimately leading to perfectly reproducible products.

Especially for the synthesis of anisotropic magnetite a technique with more control than the hydrothermal approach could yield better results, since the growth conditions need to be very exact, exceeding the degree of control that can be reached by chemistry alone. I think with less random chance encounters as present in the current reactor systems the synthesis of anisotropic particles with uniform properties could be even more precise than it already is.

Apart from hydrothermal methods we also employed a microwave-assisted synthesis approach which led to cigar shaped particles which consisted of a mixed phase of magnetite and akaganeite. The important aspect of this reaction was

that the shape of the precursor stayed largely intact during the reduction, so this could be a feasible pathway towards reproducible anisotropic magnetite nanorods.

The encapsulation of nanoparticles with silica is a very promising approach to achieve a better biocompatibility and prolonged stability.[46] The easily accessible silane chemistry allows deposition of all kinds of molecules, from drugs over polymers and should be utilized more in the future. We employed it to connect the magnetic core covalently to the hydrogel by synthesizing a silica shell using the well-established approach of Stöber[45] but also a newer bi-phase method originating from Zou *et al.*[44] With both methods it was possible to coat different iron oxide particles with a shell of tunable thickness. Since the bi-phase approach is faster and more reliable in coating single particles, though, this approach was ultimately preferred to Stöber's method. For the incorporation into a hydrogel both particles need to be coated with TPM after the coating reaction, so a phase transfer is necessary in either case.

When functionalized with TPM the functionalized particles were stable and the following encapsulation with the hydrogel was very straightforward. Although we did not create a batch of pure single core particles this should be feasible when the particles are well stabilized. We proved that our reaction pathway can produce single core particles. We also showed the thermoresponsive and magnetic properties of the hydrogel by measuring DLS and the magnetization. The thermoresponsive behavior was reversible even after multiple cycles over the course of nearly a week. The saturation magnetization corresponds to a particle load of about 1% particles in the finished hydrogel and a total iron content of 0.04%. This low value was to be expected since very low concentrations of iron are necessary to prevent agglomeration of the particles. Nevertheless, the particle content of the covalently bound hydrogel has already a quite low limit. However, we found a way to circumvent the low particle load problem by gel preparation without initial particles. In this approach the particles can be mixed into the gel at any desired content, but the interactions between particle and matrix are less direct. The mechanical properties as well as the thermoresponsive properties of the covalently linked hydrogel were not influenced by the particle content without an applied magnetic field which is good because for potential applications this parameter can be chosen freely. When the field is applied, we observed a slight stiffening of the gel, so the gel is magneto responsive.

For the synthesis of the loosely connected gel we varied different parameters to tune gel properties. The crosslinking degree was varied as well as the amount of SDS used during the emulsion polymerization. Reducing the amount of crosslinker lead to more isolated microgel particles while showing no difference in

the swelling behavior. The rheological measurements show an increase in the viscoelastic moduli with decreasing crosslinker density, but this effect could also be caused by the different polymer concentrations of the samples. All hydrogels show the typical behavior for weakly crosslinked gels. We successfully confirmed a linear dependency of the hydrodynamic radius of PNIPAM microgels on the SDS concentration in a double logarithmic plot.[158] The microgels prepared with varying amounts of SDS had a crosslinker density of 0.025 and showed the behavior of strongly crosslinked gels.

The different microgels were mixed with goethite to prepare systems where the movement of goethite is limited by the matrix. We could show that smaller PNIPAM gels allow for more motion of the goethite particles in the matrix, while larger gels restrict the particles. We could show that the thermosensitive properties of the matrix can be exploited to allow the particles to orientate when the temperature is elevated and to restructure the gel upon phase transition. We were able to trap particles in a state where their orientation is “frozen” at 20 °C. Another interesting observation was the dependence of diffusion dynamics on the particle orientation. We observed the expected result of sped up diffusion along the direction the particles are oriented in. Overall, these experiments served to highlight the importance of studying the interactions between particles and matrix, to predict these behaviors. The interactions are sometimes unexpected and go both ways, as the gel influences the freedom of motion of the particles and the particles influence the direction of the diffusion inside the hydrogel.

Although the results were very interesting, it became abundantly clear that the system was too complicated to get a complete understanding of the behavior within one measurement time at the beamline. In order to get more conclusive results, one needs more detailed measurements and some improvements would help for a possible further investigation, e.g. the magnetic sample chamber needs a better tunability of the magnetic field even above 90 mT.

Hydrogels in general have a bright future, since they are a very versatile and biocompatible material class.[164] The particular hydrogel treated in this work based on PNIPAM might be transferred to another polymeric system in the future. There are block copolymers with a better tunable LCST and comparable chemical stability that might be better suited for biological applications.[5,6] Nevertheless, PNIPAM remains an easily accessible system that functions well as a model system. In the future I would like to believe that more attention will be focused on composite materials, because in this case *the whole is greater than the sum of its parts* and there is much to gain by creating materials even more versatile.

## 6 Experimental section

This section is mainly oriented towards readers eager to replicate the results shown in this work or future colleagues trying to make sense of my samples. Therefore, I used the original sample codes and tried to give as much details as possible, tables are used for quick reference, even if they only contain one line. All materials mentioned were used as received and the supplier can be found in the disposal section 6.6.2. Whenever, water is mentioned in this section, the water was purified by a Millipore® filter at 18.4 MΩ.

### 6.1 Akaganeite

Akaganeite was used as the universal precursor for this work, yet the synthesis was not changed at all. Briefly, iron(III)chloride is hydrolyzed in the presence of  $\text{Na}_2\text{HPO}_4$  to akaganeite. The reaction was done in a large batch, because ideally one batch should be used for all related reactions to keep the results reproducible. In a standard reaction 8.14 g of  $\text{FeCl}_3 \cdot 6 \text{H}_2\text{O}$  (0.03 mol) dissolved in 1.5 L of water was mixed with 13.7 mL of a  $\text{NaH}_2\text{PO}_4$  stock solution concentrated at 0.065 M in water. The mixture was put in an oil bath at 80 °C for two days. The color changed from a yellow tone to the dark orange of akaganeite over the course of one hour. After two days the reaction mixture was concentrated until the desired concentration was reached, which was the case when 200 mL solution were left. The synthesis parameters are displayed in Table 4.

Table 4: The precursor batch used to synthesize the particles in this work. The samples are sorted in the order of appearance of the product particles in this work. The wt. % were determined by gravimetry.

| Sample name                | $\text{FeCl}_3 \cdot 6\text{H}_2\text{O}$<br>[g]<br>[mol] | $\text{NaH}_2\text{PO}_4 \cdot 2\text{H}_2\text{O}$<br>[g]<br>[mol] | wt.<br>% | Notes  |
|----------------------------|---|---|----------|--|
| BF_P2_ $\beta$ -FeOOH      | 8.11<br>0.030   | 0.11<br>$0.69 \cdot 10^{-3}$  | 5.1      |  |
| SH_ $\beta$ -<br>FeOOH_P10 | 8.14<br>0.030   | 0.11<br>$0.69 \cdot 10^{-3}$  | 8.15     |  |
| HG_15                      | 8.19<br>0.030   | 0.11<br>$0.69 \cdot 10^{-3}$  | 5.03     |  |
| EC1P                       | 1.31<br>0.005   | 0.16<br>$1.0 \cdot 10^{-3}$   | 0.75     | Concentration<br>adjusted to be<br>directly usable |
| MS_56                      | 8.14<br>0.030   | 0.11<br>$0.69 \cdot 10^{-3}$  | 8.1      |  |
| $\beta$ -FeOOH_P8          | 8.16<br>0.030   | 0.11<br>$0.69 \cdot 10^{-3}$  | 12       |  |

## 6.2 Hematite

Hematite was synthesized by hydrolyzation in a hydrothermal reactor. The synthesis was adapted from a paper by Malik *et al.*, [61] and done by Nils Nun during his bachelor thesis and later published in collaboration.[63]

An iron(III)chloride solution of 0.01 mol/L was prepared and heated to 100 °C in a hydrothermal reactor for 192 h at 1.5 bar. The product was filtrated and washed by centrifugation with water for three cycles. The synthesis parameters are displayed in Table 5.

Table 5: Synthesis parameters for the synthesis of hematite cubes.

| Sample                             | $\text{FeCl}_3 \cdot 6 \text{ H}_2\text{O}$<br>[g]<br>[mol] | $\text{c}(\text{Fe}^{3+})$<br>[mol/L] | V (Product<br>suspension)<br>[mL] |
|------------------------------------|---|---------------------------------------|-----------------------------------|
| NN_ $\alpha\text{-Fe}_2\text{O}_3$ | 1.22<br>4.50  | 0.01                                  | 300                               |



## 6.3 Goethite

### 6.3.1 Aging reactions

The standard literature synthesis was done after Lemaire *et al.*[18] but the original paper was the PhD thesis from J. Hernandez.[165] We adapted the synthesis and used it for reference purposes. In short 1 M NaOH was dropped into a 0.1 M solution of Fe(III)(NO<sub>3</sub>)<sub>3</sub> until the pH value was higher than 11, after that stirring was stopped and the suspension was left in a beaker for nine days. The solution changed colors from yellow at the start to a reddish brown after the addition of the base. The particles quickly precipitated to the bottom of the beaker after stirring was stopped. The color changed slightly over the course of 9 days until the familiar ochre color of goethite was present. The synthesis parameters are displayed in Table 6.

Table 6: Goethite sample prepared by aging of a basic solution at pH ~12.

| Sample        | Fe(NO <sub>3</sub> ) <sub>3</sub> ·9 | NaOH 1 M [mL] | Notes            |
|---------------|--------------------------------------|---------------|------------------|
|               | H <sub>2</sub> O[g]<br>[mol]         |               |                  |
| SH_Goethit_P1 | 1.93<br>4.8·10 <sup>-3</sup>         | 12            | Aging in 15 days |

### 6.3.2 Precursor based hydrothermal reactions

All precursor-based reactions started from the precursor of akaganeite which is described in section 6.1. After that the reactions diverged because a lot of different parameters were tested. In general, the reactions ran as follows:

The base solution of NaOH, final concentration 0.5 mol/L, was prepared and stirred until all the pellets were dissolved. After that either the precursor or PVP were added into the reactor. In all successful reactions we employed ~0.18 g (18 µmol) of PVP, so the concentration in a 25 mL reactor was about 0.72 mmol/L. The amount of precursor solution was chosen, so that the final concentration in the reactor was about 0.1 mol/L. Water was added until the total volume was about 25 mL. After all reactants were inside the Teflon lined

reaction vessel, the reactor was sealed. The sealed vessel was put into a heating mantle, pressurized to 10 bar with nitrogen and stirred for an hour before the temperature was raised to 160 °C over the course of two hours. The temperature was kept at 160 °C during the following reaction which took between two and 12 hours. After the reaction, the reactor was taken out of the heating mantle and either cooled in an ice bath or in air. When the reactor was at around 60 °C the pressure was released, and the reactor was opened. The product was washed three times by centrifugation at 4000 G for 10 minutes. After that the product had, depending on the reaction conditions, a yellow color, the higher the concentration of product in solution the darker the sample appeared. The synthesis parameters are displayed in Table 7.

Table 7: All the goethite samples presented in this work, sorted in chronological order. All samples were treated in a hydrothermal reactor.

| Sample         | Precursor      | PVP [g]<br>[mol]                        | Time<br>[h] | Notes                      |
|----------------|----------------|---|-------------|----------------------------|
| SH_bFeOOH_1202 | BF_P2_β-FeOOH  | -                                       | 12          | 0 bar at start             |
| SH_Goethit P4  | SH_β-FeOOH_P10 | -                                       | 12          |                            |
| HG_41          | HG-15          | 0.18 at<br>start<br>$1.8 \cdot 10^{-5}$ | 1           |                            |
| SH_146f        | EC1P           | 0.18 at<br>start<br>$1.8 \cdot 10^{-5}$ | 2           | 100 rpm                    |
| SH_146g        | EC1P           | -                                       | 2           | 100 rpm                    |
| SH_146j        | EC1P           | 0.18 last<br>$1.8 \cdot 10^{-5}$        | 2           | 500 rpm                    |
| SH_146 e       | EC1P           | 0.18 last<br>$1.8 \cdot 10^{-5}$        | 2           | 100 rpm                    |
| SH_150 b       | EC1P           | 0.18 last<br>$1.8 \cdot 10^{-5}$        | 2           | 500 rpm                    |
| SH_153         | EC1P           | -                                       | 2           | 100 ml reactor<br>1000 rpm |

## 6.4 Magnetite

### 6.4.1 Batch reactions

#### 6.4.1.1 PEG directed batch reactions

Most reactions using PEG as a structural guiding agent and as a soft template were based on a paper by Farid A. Harraz.[21] Hydrated ferrous sulfate ( $\text{FeSO}_4 \cdot 7 \text{H}_2\text{O}$ ) was ground uniformly together with  $\text{Na}_2\text{S}_2\text{O}_3$  in a mortar. PEG was dissolved in water using mild heating to  $\sim 50^\circ\text{C}$  and then the ground up reactants were added to the mixture. This reaction mixture was added into a 25 mL Teflon<sup>®</sup> lined stainless-steel autoclave together with NaOH. The reactor was heated to  $150^\circ\text{C}$  over the course of two hours and kept at that temperature for 24 hours. After 24 hours the reactors were taken out of the heating mantle to cool down to ambient temperatures. The product was transferred into a beaker and washed by magnetic separation for three cycles. Any non-magnetic material was removed by decantation. The synthesis parameters are displayed in Table 8.

Table 8: Experimental parameters for PEG directed batch reactions. Only reactions displayed in this work are shown here.

| Sample  | $\text{FeSO}_4 \cdot 7$<br>$\text{H}_2\text{O}$<br>[g]<br>[mol] | PEG<br>[g]<br>[mol]          | NaOH<br>[g]<br>[mol] | $\text{Na}_2\text{S}_2\text{O}_3$<br>[g]<br>[mol] | Time<br>[h] | Notes                             |
|---------|---|------------------------------|----------------------|---|-------------|-----------------------------------|
| SH_P68b | 1.01<br>$3.6 \cdot 10^{-3}$                                     | 12.03<br>$3.0 \cdot 10^{-3}$ | 2.05<br>0.051        | 0.50<br>$3.2 \cdot 10^{-3}$                       | 24          |                                   |
| SH_P72B | 1.00<br>$3.6 \cdot 10^{-3}$                                     | 12.00<br>$3.0 \cdot 10^{-3}$ | 2.02<br>0.050        | 0.63<br>$3.2 \cdot 10^{-3}$                       | 24          | Half<br>water,<br>half<br>ethanol |

### 6.4.1.2 Reactions with other surfactants

This section describes a class of batch reactions that happened in a hydrothermal reactor. In typical reactions the iron precursor was  $\text{FeCl}_3 \cdot 6 \text{H}_2\text{O}$  concentrated to 0.2 M in either a 25 mL reactor or in one case a 450 mL reactor. The iron salt was mixed with the surfactant directly in the reactor. A second solution of the base mixture, consisting of NaOH and hydrazine, was prepared in a beaker and stirred until all NaOH was dissolved. Then the two mixtures were united in the reactor and the reactor was filled with water until its full volume was utilized. The reactor was sealed and put into the heating mantle, where it was heated to 160 °C for 24 h. The temperature was slowly raised over the course of 2 hours. After the reaction was finished the reactor was cooled down to room temperature by either cooling in air or in an ice bath. The magnetic particles were separated by magnet induced precipitation and washed three times with water and ethanol. After this the particles were stored in water. The synthesis parameters are displayed in Table 9.

Table 9: Reaction parameters for batch reactions with different surfactants. All reactions were done in a hydrothermal reactor.

| Sample     | $\text{FeCl}_3 \cdot 6 \text{H}_2\text{O}$<br>[g]<br>[mol] | CTAB<br>[g]<br>[mol] | Hydrazine<br>[mL]<br>[mol] | NaOH<br>[g]<br>[mol] | Notes   |
|------------|--|----------------------|----------------------------|----------------------|---------|
| SH_Mag_P23 | 24.53  | 3.29                 | 34.42                      | 18                   | 450 mL  |
|            | 0.091  | $9.0 \cdot 10^{-3}$  | 0.38                       | 0.45                 | Reactor |

In another reaction ethanol and water were used as mixed solvents in a batch reaction in a flask. First 4.00 g of NaOH (0.1 mol) was mixed with the surfactant  $\text{NaH}_2\text{PO}_4 \cdot 2 \text{H}_2\text{O}$  (1.28 g dissolved in 18 mL of water and 18 mL of ethanol in a two-necked flask. The contents of the flask were heated up to reflux. Then  $\text{FeSO}_4 \cdot 7 \text{H}_2\text{O}$  was mixed with  $\text{Na}_2\text{S}_2\text{O}_3$  by mortar and added to the reaction flask. The resultant reaction has been stirred and kept under reflux for six hours. After that the product was washed by magnetic decantation and rinsed with water three times. The synthesis parameters are displayed in Table 10.

Table 10: Reaction parameters for a batch reaction using different surfactants in a water/ethanol mixture.

| Sample | FeSO <sub>4</sub> ·7 H <sub>2</sub> O | NaH <sub>2</sub> PO <sub>4</sub> | Na <sub>2</sub> S <sub>2</sub> O <sub>3</sub> |
|--------|---------------------------------------|----------------------------------|---|
|        | [g]                                   | [g]                              | [g]   |
|        | [mol]                                 | [mol]                            | [mol]   |
| CG_18  | 2.00                                  | 1.28                             | 1.00  |
|        | 7.2·10 <sup>-3</sup>                  | 8.2·10 <sup>-3</sup>             | 6.3·10 <sup>-3</sup>                          |

#### 6.4.1.3 Oxidative aging

This method is based on a publication of Vereda *et al.*[117] which was in turn based on the method of Sugimoto and Matijević.[123] In the first step the base solutions of KOH and KNO<sub>3</sub> were prepared. KOH was prepared in a 2.81 molar solution in 6.25 mL water and KNO<sub>3</sub> was prepared as a 2 M solution in 12.5 mL water. These two solutions were then added to a beaker with 100 mL of water, which was purged by nitrogen for 45 minutes. In the next step a 0.27 mol/L solution of FeSO<sub>4</sub> · 7 H<sub>2</sub>O was prepared in 11.25 mL water and purged with nitrogen for 45 minutes. Finally, both solutions were unified in a closed flask, which was purged for another minute with oxygen to get rid of oxygen residues. The concentration of the reactants in the final reaction solution were: FeSO<sub>4</sub> · 7 H<sub>2</sub>O 0.025 M, KNO<sub>3</sub> 0.2M and KOH 0.125 M. The solution showed a green color. The flask has been refluxed in a preheated 90 °C oil bath and kept at that temperature for 4 hours. After the reaction, the flask was cooled to room temperature in an ice bath and the product was separated by magnetic separation. The product was washed four times with water and ethanol. The final product was stored in ethanol. The synthesis parameters are displayed in Table 11.

Table 11: Parameters for the oxidative aging reaction. The amount of  $\text{KNO}_3$  is based on creating a 2 M stock solution in 100 mL  $\text{H}_2\text{O}$  which was used in further experiments not shown here.

| Sample | KOH<br>[g]<br>[mol] | $\text{KNO}_3$<br>[g]<br>[mol] | $\text{FeSO}_4 \cdot 7$<br>$\text{H}_2\text{O}$<br>[g]<br>[mol] | Notes                   |
|--------|---------------------|--------------------------------|---|-------------------------|
| SL_A8  | 1.96<br>0.035       | 2.02<br>0.02                   | 1.74<br>$6.3 \cdot 10^{-3}$                                     |                         |
| CG_03  | 1.03<br>0.018       | 2.63<br>0.026                  | 0.86<br>$3.1 \cdot 10^{-3}$                                     | 0.91 g citrate<br>added |

#### 6.4.2 Precursor based reactions

The precursor-based reactions were conducted similarly to the synthesis of goethite described earlier in this section. The first ingredient was always an akaganeite precursor, after that magnetite synthesis also requires a strong base. We received good results when the strong base was complimented by a weak base, here hydrazine, to guarantee the stoichiometry of  $\text{Fe(II)}/\text{Fe(III)}$  of 1/2. In a standard reaction the strong base was added first to the Teflon reactor, together with some water and hydrazine to dissolve the  $\text{NaOH}$ . After that the surfactant was added in some cases and at last the precursor solution. The amount of the reactants can be found in Table 12. After all educts were added to the reactor the autoclave was sealed and in most cases pressurized to 10 bar by nitrogen. The reaction vessel has been heated to  $160\text{ }^\circ\text{C}$  and kept at that temperature for 24 hours. After the reaction was finished the reactor was cooled to room temperature either over time or with an ice bath. The product was washed by magnetic separation for three cycles, all nonmagnetic material was discarded. The synthesis parameters are displayed in Table 12.

Table 12: Precursor based experiments in their order of appearance in this work. The precursor concentrations are given in the akaganeite chapter. The pressure  $p$  is the maximum pressure observed during the reaction. If not otherwise specified, the reactions were done after 24 hours in the reactor.

| Sample | Precursor                    | NaOH<br>[g]   | Hydrazine<br>[mL]           | Surfactant<br>[g]<br>[mol]                  | $p$<br>[bar] | Notes                        |
|--------|------------------------------|---------------|-----------------------------|---|--------------|------------------------------|
| SH_85  | MS_56<br>8 mL                | 0.82<br>0.020 | 0.77<br>$8.4 \cdot 10^{-3}$ | -   | -            | Inadequate stirring          |
| SH_87  | MS_56<br>16 mL               | 0.81<br>0.020 | 1.53<br>0.017               | -   | 7.5          | Reactor not fully closed     |
| SH_90  | MS_56<br>20 mL               | 0.80<br>0.020 | 2.00<br>0.022               | -   | 40           |                              |
| SH_58  | $\beta$ -FeOOH<br>P8<br>3 mL | -             | 1.53<br>0.017               | Citrate<br>0.40<br>$2.1 \cdot 10^{-3}$      | -            |                              |
| SH_107 | HG_15<br>22.5 mL             | 5.00<br>0.13  | 6.86<br>0.075               | Dopamine<br>0.028 g<br>$0.15 \cdot 10^{-3}$ | 25           | 2 h, large reactor<br>150 mL |

### 6.4.3 Microwave assisted synthesis

The synthesis of particles in a microwave reactor was based on a paper by Milosevic *et al.*, [28] technically this synthesis is also precursor based, but since the precursor synthesis differs from the usual procedure it will be explained here.

For the synthesis 1.35 g  $\text{FeCl}_3 \cdot 6 \text{H}_2\text{O}$  (5.00 mmol) were dissolved in 10 ml of water (0.50 M). 10 mL of  $\text{H}_2\text{O}$  together with 33  $\mu\text{L}$  of  $\text{HCl}$  (0.04 M) were added to this solution. To this mixture of  $\text{HCl}$  and iron salt, a milliliter of dopamine solution with 2.00 mg/mL was added. This was stirred for 30 min at 500 rpm. While the solution was stirring 180 ml of water were heated to 80 °C and after 30 min the iron salt mixture was added into the hot water to start the reaction. The reaction was maintained at 80 °C for 2 hours. After this the pH was measured to 1.14.

A 1 M  $\text{NaOH}$  solution was prepared by dissolving 4.00 g of  $\text{NaOH}$  in 100 mL  $\text{H}_2\text{O}$ . The alkaline solution was slowly added to the reaction mixture until the pH was neutral and the particles started to precipitate. The color of the precipitate was the orange/brown color of akaganeite. The product was isolated by centrifugation at 4000 rpm in three cycles.

The product concentration was set to 0.06 M and 2 mL were mixed with 40  $\mu\text{L}$  of  $3.9 \times 10^{-2}$  M hydrazine solution. This reaction mixture was then transferred into a microwave reaction vessel and heated at 200 W for 30 seconds or until the temperature of 110 °C was reached. After that it was cooled to room temperature by pressurized air. This cycle was repeated once, and a black precipitate was obtained. The synthesis parameters are displayed in Table 13.

Table 13: Synthesis parameters for the synthesis of  $\text{Fe}_3\text{O}_4$  nanorods in a microwave reactor. The reaction mixture was heated for 30 seconds at 200 W.

| Sample  | $\text{FeCl}_3 \cdot 6 \text{H}_2\text{O}$<br>[g]<br>[mmol] | $\text{HCl}$<br>[mL]<br>[ $\mu\text{mol}$ ] | Dopamine<br>[mg]<br>[ $\mu\text{mol}$ ] | Hydrazine<br>[mmol/L]<br>[ $\mu\text{mol}$ ] |
|---------|---|---|---|--|
| SH_124d | 1.35  | 0.033                                       | 2.00                                    | 39   |
|         | 5.00  | 48.13                                       | 10.55                                   | 49.99  |



## 6.5 Gel synthesis

### 6.5.1 Covalent

The gel synthesis with the goal of binding the particles covalently to a hydrogel was based on an approach by Karg *et al.*[41] but heavily modified to fit our system. In the first step  $\text{Na}_2\text{S}_2\text{O}_3$  and SDS were dissolved in 600 mL of  $\text{H}_2\text{O}$  and heated to 60 °C. The NIPAM monomer and the BIS crosslinker were dissolved in 40 mL Ethanol. The thermic initiator  $\text{K}_2\text{S}_2\text{O}_8$  was dissolved in 10 mL  $\text{H}_2\text{O}$  and added to the flask together with one crystal of  $(\text{NH}_4)_2\text{Fe}(\text{SO}_4)_2$  and stirred until dissolved. To start the polymerization the solution of NIPAM and BIS was added to the flask. The temperature of 60 °C has been kept for 4 hours. When the reaction was well underway 265  $\mu\text{L}$  of AA (3.54  $\mu\text{mol}$ ) were added to the flask. After the reaction was finished the entire flask was transferred into a dialysis tube to dialyze against 5 L of water. This was done to get rid of the leftover SDS, which would otherwise influence the thermoresponsive behavior of the polymer. The water in the dialysis bath was changed daily until there was no visible foam formation in the discarded wastewater. The PNIPAM hydrogel was concentrated with a rotary evaporator.

For some reactions the sequence of addition of NIPAM and BIS was changed to change the network structure. All experiments mentioned in this work are shown in Table 14.

Table 14: Experimental parameters for the PNIPAM hydrogel syntheses shown in this paper.

| Sample    | NIPAM<br>[g]<br>[mol]       | BIS<br>[g]<br>[mol]           | SDS<br>[g]<br>[mol]          | $\text{Na}_2\text{S}_2\text{O}_3$<br>[g]<br>[mol] | $\text{K}_2\text{S}_2\text{O}_8$<br>[g]<br>[mol] | Allylamine<br>[ $\mu\text{L}$ ]<br>[mol] |
|-----------|-----------------------------|-------------------------------|------------------------------|---|--|--|
| MS_Mag_P1 | 2.26<br>0.020               | 0.12<br>$0.81 \cdot 10^{-3}$  | 0.38<br>$1.3 \cdot 10^{-3}$  | 1.90<br>0.012                                     | 0.14<br>$0.50 \cdot 10^{-3}$                     | 265<br>$3.5 \cdot 10^{-6}$               |
| SH_P74    | 0.75<br>$6.7 \cdot 10^{-3}$ | 0.041<br>$0.27 \cdot 10^{-3}$ | 0.13<br>$0.44 \cdot 10^{-3}$ | 0.063<br>$0.40 \cdot 10^{-3}$                     | 0.039<br>$0.14 \cdot 10^{-3}$                    | 88.33<br>$1.2 \cdot 10^{-6}$             |

### 6.5.2 Loosely connected gel

The synthesis of crosslinked PNIPAM/GA hydrogels was directly adapted from the dissertation of Annemarie Nack.[42] In a typical synthesis 250 mL of H<sub>2</sub>O were heated to 80 °C while constantly being bubbled with nitrogen. After one hour the reaction mixture of NIPAM, GA and SDS dissolved in 10 mL of H<sub>2</sub>O was added into the reaction flask. After all reactants were dissolved and the solution was homogeneous the initiator K<sub>2</sub>S<sub>2</sub>O<sub>8</sub> was added and the reaction started. After a few minutes the reaction became noticeably turbid. The reaction has been kept at 80 °C for 4 hours, after this time the reaction mixture was a colorless, opaque liquid that showed opalescence. After cooling the reactant mixture to room temperature, the gel became transparent. The gel was dialyzed against water until no more foam formation was visible in the wastewater and after that concentrated to the desired gel content by a rotary evaporator. The synthesis parameters for all syntheses can be found in Table 15.

The amount of crosslinker was measured as the ratio between GA and the total amount of substance, so:

$$\chi = \frac{n_{GA}}{n_{GA} + n_{NIPAM}} \quad (38)$$

Table 15: Experimental parameters for the PNIPAM/GA hydrogel syntheses shown in this work.  $\chi$  was calculated according to equation (38). The wt. % were determined by gravimetry.

| Sample       | NIPAM<br>[g]<br>[mol] | GA<br>[μL]<br>[mol]  | SDS<br>[g]<br>[mol]   | K <sub>2</sub> S <sub>2</sub> O <sub>8</sub><br>[g]<br>[mol] | $\chi$ | Wt. % |
|--------------|-----------------------|----------------------|-----------------------|--|--------|-------|
| $\chi=0.1$   | 5.00                  | 230                  | 0.02                  | 0.10   | 0.1    | 1.2   |
|              | 0.044                 | 2.4·10 <sup>-6</sup> | 0.69·10 <sup>-6</sup> | 0.37·10 <sup>-3</sup>  |        |       |
| $\chi=0.05$  | 5.01                  | 110                  | 0.02                  | 0.10   | 0.05   | 2.77  |
|              | 0.044                 | 1.2·10 <sup>-3</sup> | 0.69·10 <sup>-6</sup> | 0.37·10 <sup>-3</sup>  |        |       |
| $\chi=0.025$ | 5.07                  | 53                   | 0.02                  | 0.11   | 0.025  | 7.00  |
|              | 0.045                 | 5.6·10 <sup>-7</sup> | 0.69·10 <sup>-6</sup> | 0.40·10 <sup>-3</sup>  |        |       |
| EC_3         | 1.013                 | 10.6                 | 8.03·10 <sup>-3</sup> | 0.02   | 0.025  | 3.64  |
|              | 9.0·10 <sup>-3</sup>  | 1.1·10 <sup>-7</sup> | 0.27·10 <sup>-3</sup> | 0.80·10 <sup>-6</sup>  |        |       |
| EC_5         | 1.03                  | 10.6                 | 3.10·10 <sup>-3</sup> | 0.02   | 0.025  | 2.93  |
|              | 9.1·10 <sup>-3</sup>  | 1.1·10 <sup>-7</sup> | 11·10 <sup>-6</sup>   | 0.78·10 <sup>-6</sup>  |        |       |
| EC_7         | 1.01                  | 10.6                 | 0.50·10 <sup>-3</sup> | 0.02   | 0.025  | 4     |
|              | 8.9·10 <sup>-3</sup>  | 1.1·10 <sup>-7</sup> | 1.7·10 <sup>-6</sup>  | 0.084·10 <sup>-3</sup>                                       |        |       |

## 6.6 Silica shell synthesis

### 6.6.1 Stöber

The synthesis of a silica shell after Werner Stöber[45] is the standard silica coating approach in ethanol at high pH. We used an adapted approach by Graf *et al.*[43] for our silica coating. In a general approach the particles to be coated were concentrated to roughly 0.1 wt. % in water. The particle solution was mixed with roughly 250 mL of ethanol and has been stirred for about a minute to ensure good a good particle distribution. After that 16 mL of 25 %  $\text{NH}_3$  (0.171 mol) were added to the flask and the mixture has been stirred for another minute. The actual silica coating happened by adding 0.4 mL of TEOS (1.8  $\mu\text{mol}$ ) divided into four 0.1 mL portions that were added in 5-minute intervals to the reaction mixture. This mixture has been stirred at room temperature for one day to ensure that no free TEOS was left in solution. After one day a methacrylate function was added to the silica coated particles by adding 0.4 mL of 3-trimethoxy propyl methacrylate (TPM) (1.68 mmol) to the solution. The final product was then concentrated using a rotary evaporator.







### 6.6.2 Bi-phase synthesis






The Bi-phase synthesis is derived from a paper by Zou *et al.*[44] To coat  $\text{Fe}_3\text{O}_4$  nanoparticles with a silica shell, 50 mg of the particles were added to 100 mL of water in a round bottom flask, together with 1 mL of a 35 % hydrazine solution (11  $\mu\text{mol}$ ) . After that 0.4 mL of TEOS (1.8  $\mu\text{mol}$ ) were added into the solution to start the silica coating. The reaction has been heated to 90 °C for 2 h, after that the reaction was finished and the particles could be used. In order to add a methacrylate function to these particles they need to be suspended in ethanol again. 0.4 mL of TPM (1.68 mmol) were added to the ethanol suspension and has been stirred for one day to ensure covalent binding. In a later approach the solution was also heated to boiling to ensure covalent binding of the TPM to the silica particles. This method was also applied to coat other iron oxide particles, like goethite and akaganeite.

## 7 Safety and Disposal

The chemicals that were used in this work are listed in Table 16 together with their GHS-Pictograms, Hazard- and Precautionary-Statements, as well as indications for disposal. [166]

Table 16: Used chemicals, their Hazard- and Precautionary-Statements, plus indications for disposal. The substance names are supplemented with the company they were obtained from and with a purity. (Sigma Aldrich = SiAl, Alfa Aesar = AA, Burdick und Jackson = BJ, VWR, Fluka, Merck, Carl Roth = CR, Grüssing = Grü, Acros, TCI)

| Substance  | Symbol  | Hazard-Statements                  | Precautionary-Statements                            | Disposal |
|--|---|------------------------------------|---|----------|
| $\text{FeCl}_3 \cdot 6 \text{H}_2\text{O}$<br>SiAl 97 %            |    | 290, 302,<br>315, 318              | 280, 305+351+338                                    | [1]      |
| $\text{FeCl}_2 \cdot 4 \text{H}_2\text{O}$<br>SiAl 99 %            |    | 302, 315,<br>318                   | 280,<br>301+312+330,<br>305+351+338+310             | [1]      |
| $\text{Fe}(\text{NO}_3)_3 \cdot 9 \text{H}_2\text{O}$<br>SiAl 98 % |    | 314                                | 280,<br>303+361+353,<br>304+340+310,<br>305+351+338 | [1]      |
| $\text{FeSO}_4 \cdot 7 \text{H}_2\text{O}$<br>Merck<br>99.5 %      |   | 302, 315,<br>319                   | 301+312+330,<br>305+351+338                         | [1]      |
| CTAB<br>SiAl 99 %  |  | 302, 315,<br>318, 335,<br>373, 400 | 260, 280,<br>301+312+330,<br>305+351+338+310        | [1]      |
| BIS<br>SiAl 98 %   |  | 302                                | 301+312+330   | [1]      |
| PEG 4000<br>SiAl 100 %   | Substance not dangerous according to GHS  |                                    |   | [2]      |
| PEG 400<br>SiAl 100 %  | Substance not dangerous according to GHS  |                                    |   | [2]      |

| Substance   | Symbol  | Hazard-Statements                         | Precautionary-Statements  | Disposal |
|---|---|---|---|----------|
| PEG 20000<br>AA 100 %   |   | Substance not dangerous according to GHS  |   | [2]      |
| Allylamine<br>SiAl 98 %   |    | 225,<br>301+331,<br>310, 411              | 210, 261, 273, 280,<br>301+310, 302+350   | [3]      |
| Glutaraldehyde<br>50% in H <sub>2</sub> O<br>SiAl 50 %  |    | 301+331,<br>314, 317,<br>334, 335,<br>410 | 261, 273, 280,<br>301+310+330,<br>303+361+353,<br>304+340+310,<br>305+351+338+310<br>342+311, 391,<br>403+233 | [3]      |
| Hydrazine 35%<br>in H <sub>2</sub> O<br>SiAl 35 %   |    | 301+331,<br>314, 317,<br>350, 410         | 201, 261, 273, 280,<br>301+310+330,<br>305+351+338  | [3]      |
| TPM<br>SiAl 98 %  |   | Substance not dangerous according to GHS  |   | [1]      |
| Trinatrium<br>citrat dihydrat<br>BJ 99 %  |   | Substance not dangerous according to GHS  |   | [2]      |
| Ethanol<br>VWR<br>99.8 %  |   | 225, 319                                  | 210, 305+351+338  | [4]      |
| Amberlite MB-<br>6113 (Ion-<br>Exchanger)<br>VWR<br>100 %   |   | Substance not dangerous according to GHS  |   | [2]      |
| (NH <sub>4</sub> ) <sub>2</sub> Fe(SO <sub>4</sub> ) <sub>2</sub><br>· 6 H <sub>2</sub> O<br>In-House |   | Substance not dangerous according to GHS  |   | [1]      |
| Na <sub>2</sub> SO <sub>3</sub><br>In-House   |   | Substance not dangerous according to GHS  |   | [2]      |
| TEOS<br>Fluka 99 %  |  | 226, 319,<br>331, 335                     | 210,<br>304+340+311,<br>305+351+338   | [5]      |







| Substance   | Symbol  | Hazard-Statements                         | Precautionary-Statements                                     | Disposal |
|---|---|---|--|----------|
| KPS<br>Merck 99 %                                   |  | 272, 302,<br>315, 317,<br>334, 335        | 210, 280,<br>301+312+330,<br>302+352                         | [1]      |
| Na <sub>2</sub> HPO <sub>4</sub><br>Merck<br>99.5 % | Substance not dangerous according to GHS  |   |  | [1]      |
| SDS<br>CR 99 %                                      |  | 228,<br>302+332,<br>315, 318,<br>335, 412 | 210, 261, 280,<br>301+312+330,<br>305+351+338+310<br>370+378 | [2]      |
| NaOH<br>Grü 99 %                                    |  | 290, 314                                  | 260, 280,<br>303+361+353,<br>304+340+310,<br>305+351+338     | [5]      |
| Dopamine<br>hydrochloride<br>Acros 99 %             |  | 302, 410                                  | 264, 270, 273,<br>301+312+330,<br>391, 501                   | [1]      |
| NIPAM<br>TCI 98 %                                   |  | 302, 319                                  | 305+351+338  | [1]      |
| HCl<br>VWR 37 %                                     |  | 290, 314,<br>335                          | 260, 280,<br>303+361+353,<br>304+340+310,<br>305+351+338     | [1]      |
| PVP<br>TCI 100 %                                    | Substance not dangerous according to GHS  |   |  | [2]      |

Table 17: Used carcinogenic and mutagenic substances and substances toxic for reproduction.

| Substance | Hazard-Statements              | CMR-Classification | Amount  |
|-----------|--------------------------------|--------------------|---|
| Hydrazine | 301+331, 314,<br>317, 350, 410 | 1B (C)             | 500 mL in 35%<br>solution in H <sub>2</sub> O |

## Disposal:

- [1] Substance is dissolved in  $\text{H}_2\text{O}$ , neutralized and discarded into the canister for other acids.
- [2] Solid was discarded into the contaminated waste bucket.
- [3] Substance was discarded into the canister for halogen containing / poisonous substances.
- [4] Substance was discarded into the canister for non-halogen containing solvents.
- [5] Substance was discarded into the canister for other bases.



## 8 References

1. hydrogel in Publications - Dimensions Available online: [https://app.dimensions.ai/discover/publication?search\\_text=hydrogel&search\\_type=kws&search\\_field=full\\_search](https://app.dimensions.ai/discover/publication?search_text=hydrogel&search_type=kws&search_field=full_search) (accessed on **18.5.2020**).
2. Hoffman, A.S. "Intelligent" Polymers in Medicine and Biotechnology. *Artif. Organs* **1995**, *19*, 458–467, doi:10.1111/j.1525-1594.1995.tb02359.x.
3. Gil, E.S.; Hudson, S.M. Stimuli-reponsive polymers and their bioconjugates. *Prog. Polym. Sci.* **2004**, *29*, 1173–1222, doi:10.1016/j.progpolymsci.2004.08.003.
4. Tran, N.B.; Kim, J.Y.; Kim, Y.; Kim, Y.J.; Kim, J. CO<sub>2</sub> -responsive swelling behavior and metal-ion adsorption properties in novel histamine-conjugated polyaspartamide hydrogel. **2016**, *43305*, 1–10, doi:10.1002/app.43305.
5. Lutz, J.-F.F.; Akdemir, Ö.; Hoth, A. Point by point comparison of two thermosensitive polymers exhibiting a similar LCST: Is the age of poly(NIPAM) over? *J. Am. Chem. Soc.* **2006**, *128*, 13046–13047, doi:10.1021/ja065324n.
6. Bozorg, M.; Hankiewicz, B.; Abetz, V. Solubility behaviour of random and gradient copolymers of di- And oligo(ethylene oxide) methacrylate in water: Effect of various additives. *Soft Matter* **2020**, *16*, 1066–1081, doi:10.1039/c9sm02032b.
7. Reis, A. V; Moia, T.A.; Sitta, D.L.A.; Mauricio, M.R.; Guilherme, M.R.; Rubira, A.F.; Muniz, E.C.; Ten, E.T. Sustained release of potassium diclofenac from a pH-responsive hydrogel based on gum arabic conjugates into simulated intestinal fluid. **2016**, *43319*, 1–9, doi:10.1002/app.43319.
8. Li, G.; Liu, G.; Kang, E.; Neoh, K.; Yang, X. pH-Responsive Hollow Polymeric Microspheres and Concentric Hollow Silica Microspheres from Silica- Polymer Core- Shell Microspheres. *Langmuir* **2008**, *24*, 9050–5, doi:10.1021/la8010579.
9. Piao, Y.; Kim, J.; Na, H. Bin; Kim, D.; Baek, J.S.; Ko, M.K.; Lee, J.H.; Shokouhimehr, M.; Hyeon, T. Wrap-bake-peel process for nanostructural transformation from  $\beta$ -FeOOH nanorods to biocompatible iron oxide nanocapsules. *Nat. Mater.* **2008**, *7*, 242–247, doi:10.1038/nmat2118.
10. Abdollah, S.M.; Fereshteh, F.; Nazanin, F. Synthesis and modification of iron oxide nanoparticles (magnetite) for biomedical applications. *Res. J. Biotechnol.* **2017**, *12*, 87–95, doi:10.1016/j.biomaterials.2004.10.012.
11. Bee, A.; Massart, R.; Neveu, S. Synthesis of very fine maghemite particles. *J. Magn. Magn. Mater.* **1995**, *149*, 6–9, doi:10.1016/0304-8853(95)00317-7.
12. Soenen, S.J.H.; Himmelreich, U.; Nuytten, N.; De Cuyper, M. Cytotoxic

- effects of iron oxide nanoparticles and implications for safety in cell labelling. *Biomaterials* **2011**, *32*, 195–205, doi:10.1016/j.biomaterials.2010.08.075.
13. Cullity, B.D.; Graham, C.D. *Introduction to Magnetic Materials*; John Wiley & Sons, Inc., **2008**;
  14. Yang, Z.; Yao, K. Effects of several kinds of anisotropy on the coercivity behaviors of iron oxides. *J. Appl. Phys.* **1993**, *73*, 6665–6667, doi:10.1063/1.352549.
  15. Peng, Z.; Wu, M.; Xiong, Y.; Wang, J.; Chen, Q. Synthesis of Magnetite Nanorods through Reduction of  $\beta$ -FeOOH. *Chem. Lett.* **2005**, *34*, 636–637, doi:10.1246/cl.2005.636.
  16. Kasparis, G.; Erdocio, A.S.; Tuffnell, J.M.; Thanh, N.T.K. Synthesis of size-tuneable  $\beta$ -FeOOH nanoellipsoids and a study of their morphological and compositional changes by reduction. *CrystEngComm* **2019**, 1293–1301, doi:10.1039/c8ce01778f.
  17. Lemaire, B.J.; Davidson, P.; Ferré, J.; Jamet, J.P.; Panine, P.; Dozov, I.; Jolivet, J.P. Outstanding Magnetic Properties of Nematic Suspensions of Goethite ( $\alpha$ -FeOOH) Nanorods. *Phys. Rev. Lett.* **2002**, *88*, 4, doi:10.1103/PhysRevLett.88.125507.
  18. Lemaire, B.J.; Davidson, P.; Ferré, J.; Jamet, J.P.; Petermann, D.; Panine, P.; Dozov, I.; Jolivet, J.P. Physical properties of aqueous suspensions of goethite ( $\alpha$ -FeOOH) nanorods: Part I: In the isotropic phase. *Eur. Phys. J. E* **2004**, *13*, 291–308, doi:10.1140/epje/i2003-10078-6.
  19. Lemaire, B.J.; Davidson, P.; Petermann, D.; Panine, P.; Dozov, I.; Stoenescu, D.; Jolivet, J.P. Physical properties of aqueous suspensions of goethite ( $\alpha$ -FeOOH) nanorods: Part II: In the nematic phase. *Eur. Phys. J. E* **2004**, *13*, 309–319, doi:10.1140/epje/i2003-10079-5.
  20. Thies-Weesie, D.M.E.; De Hoog, J.P.; Henar Hernandez Mendiola, M.; Petukhov, A. V.; Vroege, G.J. Synthesis of goethite as a model colloid for mineral liquid crystals. *Chem. Mater.* **2007**, *19*, 5538–5546, doi:10.1021/cm071229h.
  21. Harraz, F.A. Polyethylene glycol-assisted hydrothermal growth of magnetite nanowires: Synthesis and magnetic properties. *Phys. E Low-Dimensional Syst. Nanostructures* **2008**, *40*, 3131–3136, doi:10.1016/j.physe.2008.05.007.
  22. He, K.; Xu, C.-Y.; Zhen, L.; Shao, W.-Z. Hydrothermal synthesis and characterization of single-crystalline Fe<sub>3</sub>O<sub>4</sub> nanowires with high aspect ratio and uniformity. *Mater. Lett.* **2007**, *61*, 3159–3162, doi:10.1016/j.matlet.2006.11.023.
  23. Lian, S.; Kang, Z.; Wang, E.; Jiang, M.; Hu, C.; Xu, L. Convenient synthesis of single crystalline magnetic Fe<sub>3</sub>O<sub>4</sub> nanorods. *Solid State Commun.* **2003**, *127*, 605–608, doi:10.1016/S0038-1098(03)00580-5.

24. Wang, J.; Wu, Y.; Zhu, Y. Fabrication of complex of  $\text{Fe}_3\text{O}_4$  nanorods by magnetic-field-assisted solvothermal process. *Mater. Chem. Phys.* **2007**, *106*, 1–4, doi:10.1016/j.matchemphys.2007.04.061.
25. Wiogo, H.; Lim, M.; Munroe, P.; Amal, R. Understanding the formation of iron oxide nanoparticles with acicular structure from iron(III) chloride and hydrazine monohydrate. *Cryst. Growth Des.* **2011**, *11*, 1689–1696, doi:10.1021/cg101623n.
26. Huang, Z.; Zhang, Y.; Tang, F. Solution-phase synthesis of single-crystalline magnetic nanowires with high aspect ratio and uniformity. *Chem. Commun. (Camb)*. **2005**, 342–4, doi:10.1039/b410463c.
27. Jia, B.; Gao, L. Fabrication of  $\text{Fe}_3\text{O}_4$  core-shell polyhedron based on a mechanism analogue to Ostwald ripening process. *J. Cryst. Growth* **2007**, *303*, 616–621, doi:10.1016/j.jcrysgro.2007.01.023.
28. Milosevic, I.; Jouni, H.; David, C.; Warmont, F.; Bonnin, D.; Motte, L. Facile microwave process in water for the fabrication of magnetic nanorods. *J. Phys. Chem. C* **2011**, *115*, 18999–19004, doi:10.1021/jp205334v.
29. Davis, K.; Qi, B.; Witmer, M.; Kitchens, C.L.; Powell, B.A.; Mefford, O.T. Quantitative measurement of ligand exchange on iron oxides via radiolabeled oleic acid. *Langmuir* **2014**, *30*, 10918–10925, doi:10.1021/la502204g.
30. Wu, M.; Xiong, Y.; Jia, Y.; Niu, H.; Qi, H.; Ye, J.; Chen, Q. Magnetic field-assisted hydrothermal growth of chain-like nanostructure of magnetite. *Chem. Phys. Lett.* **2005**, *401*, 374–379, doi:10.1016/j.cplett.2004.11.080.
31. Zhang, Y.; Sun, L.; Fu, Y.; Huang, Z.C.; Bai, X.J.; Zhai, Y.; Du, J.; Zhai, H.R. The Shape Anisotropy in the Magnetic Field-Assisted Self-Assembly Chain-like Structure of Magnetite. **2009**, 8152–8157.
32. Vereda, F.; De Vicente, J.; Hidalgo-Álvarez, R. Influence of a magnetic field on the formation of magnetite particles via two precipitation methods. *Langmuir* **2007**, *23*, 3581–3589, doi:10.1021/la0633583.
33. Zhang, W.; Jia, S.; Wu, Q.; Ran, J.; Wu, S.; Liu, Y. Convenient synthesis of anisotropic  $\text{Fe}_3\text{O}_4$  nanorods by reverse co-precipitation method with magnetic field-assisted. *Mater. Lett.* **2011**, *65*, 1973–1975, doi:10.1016/j.matlet.2011.03.101.
34. Wang, J.; Chen, Q.; Zeng, C.; Hou, B. Magnetic-field-induced growth of single-crystalline  $\text{Fe}_3\text{O}_4$  nanowires. *Adv. Mater.* **2004**, *16*, 137–140, doi:10.1002/adma.200306136.
35. Fikai, D.; Fikai, A.; Vasile, B.S.; Oprea, O.; Fikai, D. *Synthesis of rod-like magnetite by using low magnetic field*; **2011**; Vol. 6.
36. Podoliak, N.; Buchnev, O.; Bavykin, D. V.; Kulak, A.N.; Kaczmarek, M.; Sluckin, T.J. Magnetite nanorod thermotropic liquid crystal colloids: Synthesis, optics and theory. *J. Colloid Interface Sci.* **2012**, *386*, 158–166,

- doi:10.1016/j.jcis.2012.07.082.
37. Lian, S.; Wang, E.; Gao, L.; Kang, Z.; Wu, D.; Lan, Y.; Xu, L. Growth of single-crystal magnetite nanowires from  $\text{Fe}_3\text{O}_4$  nanoparticles in a surfactant-free hydrothermal process. *Solid State Commun.* **2004**, *132*, 375–378, doi:10.1016/j.ssc.2004.08.013.
  38. Baer, D.R. The Chameleon effect: Characterization challenges due to the variability of nanoparticles and their surfaces. *Front. Chem.* **2018**, *6*, doi:10.3389/fchem.2018.00145.
  39. Baker, M.; Penny, D. Is there a reproducibility crisis? *Nature* **2016**, *533*, 452–454, doi:10.1038/533452A.
  40. Karg, M.; Hellweg, T. New “smart” poly(NIPAM) microgels and nanoparticle microgel hybrids: Properties and advances in characterisation. *Curr. Opin. Colloid Interface Sci.* **2009**, *14*, 438–450, doi:10.1016/j.cocis.2009.08.002.
  41. Karg, M.; Pastoriza-Santos, I.; Liz-Marzán, L.M.; Hellweg, T. A versatile approach for the preparation of thermosensitive PNIPAM core-shell microgels with nanoparticle cores. *ChemPhysChem* **2006**, *7*, 2298–2301, doi:10.1002/cphc.200600483.
  42. Nack, A. Particle-matrix interactions in ferrogels containing shape-anisotropic , magnetic nanoparticles Dissertation. **2017**.
  43. Graf, C.; Vossen, D.L.J.; Imhof, A.; Blaaderen, A. Van A General Method To Coat Colloidal Particles with Silica. **2003**, 6693–6700.
  44. Zou, J.; Peng, Y.-G.; Tang, Y.-Y. A facile bi-phase synthesis of  $\text{Fe}_3\text{O}_4/\text{SiO}_2$  core-shell nanoparticles with tunable film thicknesses. *RSC Adv.* **2014**, *4*, 9693–9700, doi:10.1039/c3ra47043a.
  45. Stober, W. Controlled Growth of Monodisperse Silica Spheres in the Micron Size Range 1. **1968**, *69*, 62–69.
  46. Lucht, N.; Friedrich, R.P.; Draack, S.; Alexiou, C.; Viereck, T.; Ludwig, F.; Hankiewicz, B. Biophysical Characterization of (Silica-coated) Cobalt Ferrite Nanoparticles for Hyperthermia Treatment. *Nanomaterials* **2019**, *9*, 1713, doi:10.3390/nano9121713.
  47. Cornell, R.M.; Schwertmann, U. *The Iron Oxides*; **2003**; Vol. 39; ISBN 3527302743.
  48. Neamtu, M.; Nadejde, C.; Hodoroaba, V.D.; Schneider, R.J.; Verestiuc, L.; Panne, U. Functionalized magnetic nanoparticles: Synthesis, characterization, catalytic application and assessment of toxicity. *Sci. Rep.* **2018**, *8*, doi:10.1038/s41598-018-24721-4.
  49. Post, J.E.; Buchwald, V.F. Crystal structure refinement of akaganeite. *Am. Mineral.* **1991**, *76*, 272–277.
  50. Cornell, R.M.; Schwertmann, U. The Iron Oxides: Structure, Properties, Reactions, Occurrences and Uses. *Techniques* **2003**, doi:10.1002/3527602097.
  51. Post, J.E.; Heaney, P.J.; Von Dreele, R.B.; Hanson, J.C. Neutron and

- temperature-resolved synchrotron X-ray powder diffraction study of akaganéite. *Am. Mineral.* **2003**, *88*, 782–788, doi:10.2138/am-2003-5-607.
52. Yuan, Z.Y.; Su, B.L. Surfactant-assisted nanoparticle assembly of mesoporous  $\beta$ -FeOOH (akaganeite). *Chem. Phys. Lett.* **2003**, *381*, 710–714, doi:10.1016/j.cplett.2003.10.033.
53. Gash, A.E.; Satcher, J.H.; Simpson, R.L. Strong akaganeite aerogel monoliths using epoxides: Synthesis and characterization. *Chem. Mater.* **2003**, *15*, 3268–3275, doi:10.1021/cm034211p.
54. Jung, J.; Song, K.; Bae, D.R.; Lee, S.W.; Lee, G.; Kang, Y.M.  $\beta$ -FeOOH nanorod bundles with highly enhanced round-trip efficiency and extremely low overpotential for lithium-air batteries. *Nanoscale* **2013**, *5*, 11845–11849, doi:10.1039/c3nr04502a.
55. Kozin, P.A.; Boily, J.F. Proton binding and ion exchange at the akaganéite/water interface. *J. Phys. Chem. C* **2013**, *117*, 6409–6419, doi:10.1021/jp3101046.
56. Mohapatra, J.; Mitra, A.; Tyagi, H.; Bahadur, D.; Aslam, M. Iron oxide nanorods as high-performance magnetic resonance imaging contrast agents. *Nanoscale* **2015**, *7*, 9174–9184, doi:10.1039/C5NR00055F.
57. Tadic, M.; Milosevic, I.; Kralj, S.; Mitric, M.; Makovec, D.; Saboungi, M.L.; Motte, L. Synthesis of metastable hard-magnetic  $\epsilon$ -Fe<sub>2</sub>O<sub>3</sub> nanoparticles from silica-coated akaganeite nanorods. *Nanoscale* **2017**, *9*, 10579–10584, doi:10.1039/c7nr03639f.
58. Jain, A.; Ong, S.P.; Hautier, G.; Chen, W.; Richards, W.D.; Dacek, S.; Cholia, S.; Gunter, D.; Skinner, D.; Ceder, G.; et al. Commentary: The Materials Project: A materials genome approach to accelerating materials innovation. *APL Mater.* **2013**, *1*, 011002, doi:10.1063/1.4812323.
59. Coey, J.M.D. Magnetic Properties of Iron in Soil Iron Oxides and Clay Minerals. In *Iron in Soils and Clay Minerals*; Springer Netherlands: Dordrecht, **1988**; pp. 397–466.
60. Märkert, C.; Fischer, B.; Wagner, J. Small-angle scattering from spindle-shaped colloidal hematite particles in external magnetic fields. *J. Appl. Crystallogr.* **2011**, *44*, 441–447, doi:10.1107/S0021889811009617.
61. Malik, V.; Grobety, B.; Trappe, V.; Dietsch, H.; Schurtenberger, P. A closer look at the synthesis and formation mechanism of hematite nanocubes. *Colloids Surfaces A Physicochem. Eng. Asp.* **2014**, *445*, 21–29, doi:http://dx.doi.org/10.1016/j.colsurfa.2013.12.069.
62. Pu, Z.; Cao, M.; Yang, J.; Huang, K.; Hu, C. Controlled synthesis and growth mechanism of hematite nanorhomboheda, nanorods and nanocubes. *Nanotechnology* **2006**, *17*, 799–804, doi:10.1088/0957-4484/17/3/031.
63. Hinrichs, S.; Nun, N.; Fischer, B. Synthesis and characterization of anisotropic magnetic hydrogels. *J. Magn. Magn. Mater.* **2017**, *431*, 237–240, doi:10.1016/j.jmmm.2016.10.016.

64. Lian, S.; Wang, E.; Kang, Z.; Bai, Y.; Gao, L.; Jiang, M.; Hu, C.; Xu, L. Synthesis of magnetite nanorods and porous hematite nanorods. *Solid State Commun.* **2004**, *129*, 485–490, doi:10.1016/j.ssc.2003.11.043.
65. Sugimoto, T.; Muramatsu, A. Formation Mechanism of Monodispersed  $\alpha$ -Fe<sub>2</sub>O<sub>3</sub>-Particles in Dilute FeCl<sub>3</sub>-Solutions. *J. Colloid Interface Sci.* **1996**, *184*, 626–638, doi:http://dx.doi.org/10.1006/jcis.1996.0660.
66. Jones, F.; Ogden, M.I.; Oliveira, A.; Parkinson, G.M.; Richmond, W.R. The effect of phosphonate-based growth modifiers on the morphology of hematite nanoparticles formed via acid hydrolysis of ferric chloride solutions. *CrystEngComm* **2003**, *5*, 159–163, doi:10.1039/B302911E.
67. Gualtieri, A.F.; Venturelli, P.; Rietveld, T. In situ study of the goethite-hematite phase transformation by real time synchrotron powder diffraction. *Am. Miner.* **1999**, *84*, 895–904, doi:10.2138/am-1999-5-624.
68. Lemaire, B.J.; Davidson, P.; Ferré, J.; Jamet, J.P.; Panine, P.; Dozov, I.; Jolivet, J.P. Outstanding Magnetic Properties of Nematic Suspensions of Goethite ( $\alpha$ -FeOOH) Nanorods. *Phys. Rev. Lett.* **2002**, *88*, 4, doi:10.1103/PhysRevLett.88.125507.
69. Coey, J.M.D.; Barry, A.; Brotto, J.; Rakoto, H.; Brennan, S.; Mussel, W.N.; Collomb, A.; Fruchart, D. Spin flop in goethite. *J. Phys. Condens. Matter* **1995**, *7*, 759–768, doi:10.1088/0953-8984/7/4/006.
70. Faivre, D.; Schüler, D. Magnetotactic bacteria and magnetosomes. *Chem. Rev.* **2008**, *108*, 4875–4898, doi:10.1021/cr078258w.
71. Bragg, W.H. The structure of the spinel group of crystals. *London, Edinburgh, Dublin Philos. Mag. J. Sci.* **1915**, *30*, 305–315, doi:10.1080/14786440808635400.
72. Dunlop, D.J. Superparamagnetic and single-domain threshold sizes in magnetite. *J. Geophys. Res.* **1973**, *78*, 1780–1793, doi:10.1029/jb078i011p01780.
73. Meisen, U.; Kathrein, H. The Influence of Particle Size, Shape and Particle Size Distribution on Properties of Magnetites for the Production of Toners.
74. Fock, J.; Bogart, L.K.; González-Alonso, D.; Espeso, J.I.; Hansen, M.F.; Varón, M.; Frandsen, C.; Pankhurst, Q.A. On the ‘centre of gravity’ method for measuring the composition of magnetite/maghemite mixtures, or the stoichiometry of magnetite-maghemite solid solutions, via 57 Fe Mössbauer spectroscopy. *J. Phys. D. Appl. Phys.* **2017**, *50*, 265005, doi:10.1088/1361-6463/aa73fa.
75. Gonano, C.A.; Zich, R.E.; Mussetta, M. *Definition for Polarization P and Magnetization M Fully Consistent with Maxwell’s Equations*; **2015**; Vol. 64;.
76. Pierre, W. La variation du ferromagnétisme avec la température. *Comptes Rendus des Séances l’Académie des Sci.* **1906**, *143*, 1136–1139.
77. Weiss, P. L’hypothèse du champ moléculaire et la propriété

- ferromagnétique. *J. Phys. Théorique Appliquée* **1907**, 6, 661–690, doi:10.1051/jphystap:019070060066100.
78. Heisenberg, W. Zur Theorie des Ferromagnetismus. *Zeitschrift für Phys.* **1928**, 49, 619–636, doi:10.1007/BF01328601.
  79. Bethe-Slater curve by Zureks - Bethe-Slater-Kurve – Wikipedia Available online: [https://de.wikipedia.org/wiki/Bethe-Slater-Kurve#/media/Datei:Bethe-Slater\\_curve\\_by\\_Zureks.svg](https://de.wikipedia.org/wiki/Bethe-Slater-Kurve#/media/Datei:Bethe-Slater_curve_by_Zureks.svg) (accessed on **30.3.2020**).
  80. Anderson, P.W. Antiferromagnetism. Theory of superexchange interaction. *Phys. Rev.* **1950**, 79, 350–356, doi:10.1103/PhysRev.79.350.
  81. Pavarini, E.; Koch, E.; Anders, F.; Jarrell, M. *Modeling and Simulation 2 Modeling and Simulation Band / Volume 2 ISBN 978-3-89336-796-2 Correlated Electrons: From Models to Materials*; ISBN 9783893367962.
  82. File:SingleDomainMagneticCharges.svg - Wikipedia Available online: <https://en.wikipedia.org/wiki/File:SingleDomainMagneticCharges.svg> (accessed on **3.4.2020**).
  83. Abert, C. Micromagnetics and spintronics: models and numerical methods. *Eur. Phys. J. B* **2019**, 92, 120, doi:10.1140/epjb/e2019-90599-6.
  84. Néel, M.L. Théorie du traînage magnétique des ferromagnétiques en grains fins avec application aux terres cuites. *Ann. Geophys.* **1949**, 5, 99–136, doi:10.1017/CBO9781107415324.004.
  85. French, S.J. Polar Molecules. *Sci. Am.* **1936**, 155, 24–25, doi:10.1038/scientificamerican0736-24.
  86. Lutz, J.F.; Hoth, A. Preparation of ideal PEG analogues with a tunable thermosensitivity by controlled radical copolymerization of 2-(2-methoxyethoxy)ethyl methacrylate and oligo(ethylene glycol) methacrylate. *Macromolecules* **2006**, 39, 893–896, doi:10.1021/ma0517042.
  87. Graziano, G. On the temperature-induced coil to globule transition of poly-N-isopropylacrylamide in dilute aqueous solutions. *Int. J. Biol. Macromol.* **2000**, 27, 89–97, doi:10.1016/S0141-8130(99)00122-1.
  88. Rosensweig, R.E.E. Heating magnetic fluid with alternating magnetic field. *J. Magn. Magn. Mater.* **2002**, 252, 370–374, doi:10.1016/S0304-8853(02)00706-0.
  89. Skumiel; Łabowski the Heating Effect of the Biocompatible Ferrofluid in an Alternating Magnetic Field. *Mol. Quantum Acoust.* **2006**, 27, 233.
  90. Brazel, C.S. Expert Review Magnetothermally-responsive Nanomaterials: Combining Magnetic Nanostructures and Thermally-Sensitive Polymers for Triggered Drug Release. **2008**, doi:10.1007/s11095-008-9773-2.
  91. Lin, X.; Huang, R.; Ulbricht, M. Novel magneto-responsive membrane for remote control switchable molecular sieving. *J. Mater. Chem. B* **2015**, 4, 867–879, doi:10.1039/C5TB02368H.
  92. Odenbach, S. Microstructure and rheology of magnetic hybrid materials. *Arch. Appl. Mech.* **2016**, 86, 269–279, doi:10.1007/s00419-015-1092-6.

93. Alexander, A.; Ajazuddin; Khan, J.; Saraf, S.; Saraf, S. Polyethylene glycol (PEG)-Poly(N-isopropylacrylamide) (PNIPAAm) based thermosensitive injectable hydrogels for biomedical applications. *Eur. J. Pharm. Biopharm.* **2014**, *88*, 575–585, doi:10.1016/j.ejpb.2014.07.005.
94. Guan, Y.; Zhang, Y. PNIPAM microgels for biomedical applications: From dispersed particles to 3D assemblies. *Soft Matter* **2011**, *7*, 6375–6384, doi:10.1039/c0sm01541e.
95. Thorne, J.B.; Vine, G.J.; Snowden, M.J. Microgel applications and commercial considerations. *Colloid Polym. Sci.* **2011**, *289*, 625–646, doi:10.1007/s00396-010-2369-5.
96. Van Blaaderen, A.; Van Geest, J.; Vrij, A. Monodisperse colloidal silica spheres from tetraalkoxysilanes: Particle formation and growth mechanism. *J. Colloid Interface Sci.* **1992**, *154*, 481–501, doi:10.1016/0021-9797(92)90163-G.
97. Feng, J.; Mao, J.; Wen, X.; Tu, M. Ultrasonic-assisted in situ synthesis and characterization of superparamagnetic Fe<sub>3</sub>O<sub>4</sub> nanoparticles. *J. Alloys Compd.* **2011**, *509*, 9093–9097, doi:10.1016/j.jallcom.2011.06.053.
98. Li, G. yin; Jiang, Y. ren; Huang, K. long; Ding, P.; Chen, J. Preparation and properties of magnetic Fe<sub>3</sub>O<sub>4</sub>-chitosan nanoparticles. *J. Alloys Compd.* **2008**, *466*, 451–456, doi:10.1016/j.jallcom.2007.11.100.
99. Fruijtier-Pöloth, C. Safety assessment on polyethylene glycols (PEGs) and their derivatives as used in cosmetic products. *Toxicology* **2005**, *214*, 1–38, doi:10.1016/j.tox.2005.06.001.
100. Yag, C.; Graz, V.; Arruebo, M. Synthesis and stealthing study of bare and PEGylated silica micro- and nanoparticles as potential drug-delivery vectors. **2008**, *137*, 45–53, doi:10.1016/j.cej.2007.07.088.
101. Kloust, H.; Schmidtke, C.; Merkl, J.-P.; Feld, A.; Schotten, T.; Fittschen, U.E.A.; Gehring, M.; Ostermann, J.; Pö, E.; Weller, H. Poly(ethylene oxide) and Polystyrene Encapsulated Quantum Dots: Highly Fluorescent, Functionalizable, and Ultrastable in Aqueous Media. *J. Phys. Chem. C* **2013**, *117*, doi:10.1021/jp4045836.
102. Meenach, S. a; Shapiro, J.M.; Hilt, J.Z.; Anderson, K.W. Characterization of PEG-iron oxide hydrogel nanocomposites for dual hyperthermia and paclitaxel delivery. *J. Biomater. Sci. Polym. Ed.* **2013**, *24*, 1112–26, doi:10.1080/09205063.2012.741321.
103. Nappini, S.; Magnano, E.; Bondino, F.; Píř, I.; Barla, A.; Fantechi, E.; Pineider, F.; Sangregorio, C.; Vaccari, L.; Venturelli, L.; et al. Surface Charge and Coating of CoFe<sub>2</sub>O<sub>4</sub> Nanoparticles: Evidence of Preserved Magnetic and Electronic Properties. *J. Phys. Chem. C* **2015**, *119*, 25529–25541, doi:10.1021/acs.jpcc.5b04910.
104. Lamer, V.K.; Dinegar, R.H. Theory, Production and Mechanism of Formation of Monodispersed Hydrosols. *J. Am. Chem. Soc.* **1950**, *72*, 4847–4854, doi:10.1021/ja01167a001.



105. Rogach, A.L.; Talapin, D.V.; Shevchenko, E.V.; Kornowski, A.; Haase, M.; Weller, H. Organization of Matter on Different Size Scales: Monodisperse Nanocrystals and Their Superstructures. *Adv. Funct. Mater.* **2002**, *12*, 653–664, doi:10.1002/1616-3028(20021016)12:10<653::AID-ADFM653>3.0.CO;2-V.
106. Polte, J. Fundamental growth principles of colloidal metal nanoparticles - a new perspective. *CrystEngComm* **2015**, *17*, 6809–6830, doi:10.1039/c5ce01014d.
107. Byrappa, K.; Adschiri, T. Hydrothermal technology for nanotechnology. *Prog. Cryst. Growth Charact. Mater.* **2007**, *53*, 117–166, doi:10.1016/j.pcrysgrow.2007.04.001.
108. Suber, L.; Fiorani, D.; Imperatori, P.; Foglia, S.; Montone, A.; Zysler, R. Effects of thermal treatments on structural and magnetic properties of acicular  $\alpha$ -Fe<sub>2</sub>O<sub>3</sub> nanoparticles. *Nanostructured Mater.* **1999**, *11*, 797–803, doi:10.1016/S0965-9773(99)00369-4.
109. Mohapatra, M.; Rout, K.; Gupta, S.K.; Singh, P.; Anand, S.; Mishra, B.K. Facile synthesis of additive-assisted nano goethite powder and its application for fluoride remediation. *J. Nanoparticle Res.* **2010**, *12*, 681–686, doi:10.1007/s11051-009-9779-7.
110. Yang, H.; Lu, R.; Downs, R.T.; Costin, G. Goethite,  $\alpha$ -FeO(OH), from single-crystal data. *Acta Crystallogr. Sect. E Struct. Reports Online* **2006**, *62*, i250–i252, doi:10.1107/S1600536806047258.
111. Rădițoiu, V.; Diamandescu, L.; Cosmin Corobea, M.; Rădițoiu, A.; Popescu-Pogrión, N.; Andi Nicolae, C. A facile hydrothermal route for the synthesis of  $\alpha$ -FeOOH with controlled morphology. *J. Cryst. Growth* **2012**, *348*, 40–46, doi:10.1016/j.jcrysgro.2012.03.032.
112. Wang, J.; Peng, Z.; Huang, Y.; Chen, Q. Growth of magnetite nanorods along its easy-magnetization axis of [1 1 0]. *J. Cryst. Growth* **2004**, *263*, 616–619, doi:10.1016/j.jcrysgro.2003.11.102.
113. Davis, K.; Cole, B.; Ghelardini, M.; Powell, B.A.; Mefford, O.T. Quantitative Measurement of Ligand Exchange with Small-Molecule Ligands on Iron Oxide Nanoparticles via Radioanalytical Techniques. *Langmuir* **2016**, *32*, 13716–13727, doi:10.1021/acs.langmuir.6b03644.
114. Vereda, F.; de Vicente, J.; Hidalgo-Álvarez, R. Colloidal characterization of micron-sized rod-like magnetite particles. *Colloids Surfaces A Physicochem. Eng. Asp.* **2008**, *319*, 122–129, doi:10.1016/j.colsurfa.2007.06.055.
115. Podoliak, N.; Buchnev, O.; Bavykin, D. V.; Kulak, A.N.; Kaczmarek, M.; Sluckin, T.J. Magnetite nanorod thermotropic liquid crystal colloids: Synthesis, optics and theory. *J. Colloid Interface Sci.* **2012**, *386*, 158–166, doi:10.1016/j.jcis.2012.07.082.
116. Santoyo Salazar, J.; Perez, L.; De Abril, O.; Truong Phuoc, L.; Ihiawakrim, D.; Vazquez, M.; Greneche, J.M.; Begin-Colin, S.; Pourroy,

- G. Magnetic iron oxide nanoparticles in 10–40 nm range: Composition in terms of magnetite/maghemite ratio and effect on the magnetic properties. *Chem. Mater.* **2011**, *23*, 1379–1386, doi:10.1021/cm103188a.
117. Vereda, F.; Vicente, J. De; Morales, P.; Rull, F.; Hidalgo-a, R. Synthesis and Characterization of Single-Domain Monocrystalline Magnetite Particles by Oxidative Aging of  $\text{Fe}(\text{OH})_2$ . **2008**, 5843–5849.
118. Ahn, T.; Kim, J.H.; Yang, H.M.; Lee, J.W.; Kim, J.D. Formation pathways of magnetite nanoparticles by coprecipitation method. *J. Phys. Chem. C* **2012**, *116*, 6069–6076, doi:10.1021/jp211843g.
119. Xiao, D.; Lu, T.; Zeng, R.; Bi, Y. Preparation and highlighted applications of magnetic microparticles and nanoparticles: a review on recent advances. *Microchim. Acta* **2016**, *183*, 2655–2675, doi:10.1007/s00604-016-1928-y.
120. Thapa, D.; Palkar, V.R.; Kurup, M.B.; Malik, S.K. Properties of magnetite nanoparticles synthesized through a novel chemical route. *Mater. Lett.* **2004**, *58*, 2692–2694, doi:10.1016/j.matlet.2004.03.045.
121. Gnanaprakash, G.; Mahadevan, S.; Jayakumar, T.; Kalyanasundaram, P.; Philip, J.; Raj, B. Effect of initial pH and temperature of iron salt solutions on formation of magnetite nanoparticles. *Mater. Chem. Phys.* **2007**, *103*, 168–175, doi:10.1016/j.matchemphys.2007.02.011.
122. Gnanaprakash, G.; Philip, J.; Jayakumar, T.; Raj, B. Effect of digestion time and alkali addition rate on physical properties of magnetite nanoparticles. *J. Phys. Chem. B* **2007**, *111*, 7978–7986, doi:10.1021/jp071299b.
123. Sugimoto, T.; Matijević, E. Formation of uniform spherical magnetite particles by crystallization from ferrous hydroxide gels. *J. Colloid Interface Sci.* **1980**, *74*, 227–243, doi:10.1016/0021-9797(80)90187-3.
124. Wang, W.-W.; Zhu, Y.-J.; Ruan, M.-L. Microwave-assisted synthesis and magnetic property of magnetite and hematite nanoparticles. *J. Nanoparticle Res.* **2007**, *9*, 419–426, doi:10.1007/s11051-005-9051-8.
125. Dąbrowska, S.; Chudoba, T.; Wojnarowicz, J.; Łojkowski, W. Current trends in the development of microwave reactors for the synthesis of nanomaterials in laboratories and industries: A review. *Crystals* **2018**, *8*, 1–26, doi:10.3390/cryst8100379.
126. Sugimoto, T.; Muramatsu, A. Formation mechanism of monodispersed  $\alpha$ - $\text{Fe}_2\text{O}_3$  particles in dilute  $\text{FeCl}_3$  solutions. *J. Colloid Interface Sci.* **1996**, *184*, 626–638, doi:10.1006/jcis.1996.0660.
127. Patnaik, P. Handbook of inorganic chemicals. *Choice Rev. Online* **2003**, *40*, 40-6428-40-6428, doi:10.5860/CHOICE.40-6428.
128. Galasińska, E. *Approach to make pNipam accessible for x-rays scattering experiments*; **2013**;
129. Hu, Z.; Huang, G. A New Route to Crystalline Hydrogels, Guided by a Phase Diagram. *Angew. Chemie - Int. Ed.* **2003**, *42*, 4799–4802,

- doi:10.1002/anie.200351326.
130. Vitrobot | Cryo EM Sample Preparation | Thermo Fisher Scientific - DE Available online: <https://www.thermofisher.com/de/de/home/electron-microscopy/products/sample-preparation-equipment-em/vitrobot-system.html> (accessed on **8.5.2020**).
  131. Schneider, C.A.; Rasband, W.S.; Eliceiri, K.W. NIH Image to ImageJ: 25 years of image analysis. *Nat. Methods* **2012**, *9*, 671–675.
  132. Scherrer, P. Bestimmung der inneren Struktur und der Größe von Kolloidteilchen mittels Röntgenstrahlen. In *Kolloidchemie Ein Lehrbuch*; Springer Berlin Heidelberg: Berlin, Heidelberg, **1912**; Vol. 1918, pp. 387–409.
  133. Foner, S. Versatile and sensitive vibrating-sample magnetometer. *Rev. Sci. Instrum.* **1959**, *30*, 548–557, doi:10.1063/1.1716679.
  134. Schärtl, W. *Light scattering from polymer solutions and nanoparticle dispersions*; Springer, **2007**; ISBN 9783642091087.
  135. Mezger, T.G. *Das Rheologie Handbuch Für Anwender von Rotations- und Oszillations-Rheometern*; 3rd ed.; Vincentz Network, **2010**;
  136. Kraus, G.; Rollmann, K.W. The entanglement plateau in the dynamic modulus of rubbery styrene–diene block copolymers. Significance to pressure-sensitive adhesive formulations. *J. Appl. Polym. Sci.* **1977**, *21*, 3311–3318, doi:10.1002/app.1977.070211210.
  137. Modular Compact Rheometer: MCR 102/302/502 :: Anton-Paar.com Available online: <https://www.anton-paar.com/de-de/produkte/details/rheometer-mcr-102-302-502/> (accessed on **25.8.2020**).
  138. Feigin, L.A.; Svergun, D.I. *Structure Analysis by Small-Angle X-Ray and Neutron Scattering*; Springer US, **1987**;
  139. Yano, T.; Higaki, Y.; Tao, D.; Murakami, D.; Kobayashi, M.; Ohta, N.; Koike, J.I.; Horigome, M.; Masunaga, H.; Ogawa, H.; et al. Orientation of poly(vinyl alcohol) nanofiber and crystallites in non-woven electrospun nanofiber mats under uniaxial stretching. *Polym. (United Kingdom)* **2012**, *53*, 4702–4708, doi:10.1016/j.polymer.2012.07.067.
  140. Shpyrko, O.G. Synchrotron Radiation X-ray photon correlation spectroscopy. *J. Synchrotron Rad* **2014**, *21*, 1057–1064, doi:10.1107/S1600577514018232.
  141. Unified Data Sheet Available online: [https://photon-science.desy.de/facilities/petra\\_iii/beamlines/p10\\_coherence\\_application/s/unified\\_data\\_sheet\\_p10/index\\_eng.html](https://photon-science.desy.de/facilities/petra_iii/beamlines/p10_coherence_application/s/unified_data_sheet_p10/index_eng.html) (accessed on **15.5.2020**).
  142. Schavkan, A. *Dynamics of colloidal systems of magnetic nanoparticles under influence of magnetic fields investigated by XPCS*; **2017**;
  143. Haglund, B.O. Solubility studies of polyethylene glycols in ethanol and water. *Thermochim. Acta* **1987**, *114*, 97–102, doi:10.1016/0040-6031(87)80246-0.

144. Sugimoto, T.; Wang, Y.; Itoh, H.; Muramatsu, A. Systematic control of size, shape and internal structure of monodisperse  $\alpha$ -Fe<sub>2</sub>O<sub>3</sub> particles. *Colloids Surfaces A Physicochem. Eng. Asp.* **1998**, *134*, 265–279, doi:http://dx.doi.org/10.1016/S0927-7757(97)00103-9.
145. Daou, T.J.; Begin-Colin, S.; Grenèche, J.M.; Thomas, F.; Derory, A.; Bernhardt, P.; Legaré, P.; Pourroy, G. Phosphate adsorption properties of magnetite-based nanoparticles. *Chem. Mater.* **2007**, *19*, 4494–4505, doi:10.1021/cm071046v.
146. Matijević, E.; Sapiesszko, R.S.; Melville, J.B. Ferric hydrous oxide sols I. Monodispersed basic iron(III) sulfate particles. *J. Colloid Interface Sci.* **1975**, *50*, 567–581, doi:10.1016/0021-9797(75)90180-0.
147. Vereda, F.; de Vicente, J.; Morales, M. del P.; Rull, F.; Hidalgo-Álvarez, R. Synthesis and Characterization of Single-Domain Monocrystalline Magnetite Particles by Oxidative Aging of Fe(OH)<sub>2</sub>. *J. Phys. Chem. C* **2008**, *112*, 5843–5849, doi:10.1021/jp711990f.
148. Goya, G.F.; Berquó, T.S.; Fonseca, F.C.; Morales, M.P. Static and dynamic magnetic properties of spherical magnetite nanoparticles. *J. Appl. Phys.* **2003**, *94*, 3520–3528, doi:10.1063/1.1599959.
149. Chai, L.; Han, N.; Wei, L.; Wu, X.; Chen, Y. Hydrothermal synthesis of  $\beta$ -FeOOH with different morphologies using NaH<sub>2</sub>PO<sub>4</sub> as structural modifier. *J. Wuhan Univ. Technol. Sci. Ed.* **2012**, *27*, 662–664, doi:10.1007/s11595-012-0524-1.
150. Chitrakar, R.; Tezuka, S.; Sonoda, A.; Sakane, K.; Ooi, K.; Hirotsu, T. Phosphate adsorption on synthetic goethite and akaganeite. *J. Colloid Interface Sci.* **2006**, *298*, 602–608, doi:10.1016/j.jcis.2005.12.054.
151. Dar, M.I.; Shivashankar, S.A. Single crystalline magnetite, maghemite, and hematite nanoparticles with rich coercivity. *RSC Adv.* **2014**, *4*, 4105–4113, doi:10.1039/c3ra45457f.
152. Daou, T.J.; Grenèche, J.M.; Pourroy, G.; Buathong, S.; Derory, A.; Ulhaq-Bouillet, C.; Donnio, B.; Guillon, D.; Begin-Colin, S. Coupling agent effect on magnetic properties of functionalized magnetite-based nanoparticles. *Chem. Mater.* **2008**, *20*, 5869–5875, doi:10.1021/cm801405n.
153. Schwertmann, U.; Cornell, R.M. *Iron Oxides in the Laboratory*; Schwertmann, U., Cornell, R.M., Eds.; Wiley-VCH Verlag GmbH: Weinheim, Germany, **2000**; Vol. 56; ISBN 9783527613229.
154. Kosmulski, M. Isoelectric points and points of zero charge of metal (hydr)oxides: 50 years after Parks' review. *Adv. Colloid Interface Sci.* **2016**, *238*, 1–61, doi:10.1016/j.cis.2016.10.005.
155. Num, N.; Hinrichs, S.; Schroer, M.A.; Sheyfer, D.; Grübel, G.; Fischer, B. Tuning the Size of Thermoresponsive Poly(N-Isopropyl Acrylamide) Grafted Silica Microgels. *Gels* **2017**, *3*, 34, doi:10.3390/gels3030034.
156. Bonhome-Espinosa, A.B.; Campos, F.; Rodriguez, I.A.; Carriel, V.;

- Marins, J.A.; Zubarev, A.; Duran, J.D.G.; Lopez-Lopez, M.T. Effect of particle concentration on the microstructural and macromechanical properties of biocompatible magnetic hydrogels. *Soft Matter* **2017**, *13*, 2928–2941, doi:10.1039/c7sm00388a.
157. Hofmann, C.; Schönhoff, M. Do additives shift the LCST of poly (N-isopropylacrylamide) by solvent quality changes or by direct interactions? *Colloid Polym. Sci.* **2009**, *287*, 1369–1376, doi:10.1007/s00396-009-2103-3.
158. Wu, X.; Pelton, R.H.; Hamielec, A.E.; Woods, D.R.; McPhee, W. The kinetics of poly(N-isopropylacrylamide) microgel latex formation. *Colloid Polym. Sci.* **1994**, *272*, 467–477, doi:10.1007/BF00659460.
159. Graessley, W.W. The entanglement concept in polymer rheology. In *The Entanglement Concept in Polymer Rheology*; Springer-Verlag: Berlin/Heidelberg, **1974**; Vol. 16, pp. 1–179.
160. Fischer, B.; Abetz, V. Determination of thermodynamic and structural quantities of polymers by scattering techniques. *Pure Appl. Chem.* **2018**, *90*, 955–968, doi:10.1515/pac-2017-1101.
161. Wagner, J.; Märkert, C.; Fischer, B.; Müller, L. Direction dependent diffusion of aligned magnetic rods by means of X-ray photon correlation spectroscopy. *Phys. Rev. Lett.* **2013**, *110*, 1–5, doi:10.1103/PhysRevLett.110.048301.
162. LU91003I2 - Resovist - Google Patents Available online: <https://patents.google.com/patent/LU91003I2/ko> (accessed on **27.5.2020**).
163. Valencia, P.M.; Farokhzad, O.C.; Karnik, R.; Langer, R. Microfluidic technologies for accelerating the clinical translation of nanoparticles. *Nat. Nanotechnol.* **2012**, *7*, 623–629, doi:10.1038/nnano.2012.168.
164. Ahmed, E.M. Hydrogel: Preparation , characterization , and applications : A review. *J. Adv. Res.* **2015**, *6*, 105–121, doi:10.1016/j.jare.2013.07.006.
165. Hernandez, J. Synthèse de nanoparticules d'oxydes de fer et d'aluminium pour l'étude de l'adsorption d'entités inorganiques polycondensées Conséquences sur la stabilité des dispersions, Paris 6, **1998**.
166. GESTIS-Stoffdatenbank Available online: <http://gestis.itrust.de/> (accessed on **25.5.2020**).

## 9 Danksagung

An dieser Stelle möchte ich allen Danken die mich auf dem Weg meiner Dissertation und davor begleitet und unterstützt haben.

Als erstes kommt dabei natürlich meine Betreuerin Birgit Hankiewicz in den Sinn. Sie unterstützte mich bereits zu Zeiten meines Masters durch das organisieren eines HiWi-Jobs der mich dem Thema der magnetischen Nanopartikel näher brachte und mich in den SPP1681 einführte. Dieser Job war es dann auch nach dem Bachelor der mich im Ak-Abetz festgenagelt hat. Danach folgte die Masterarbeit bei der ich ebenfalls von dir betreut wurde und während der du es mir ermöglichtest die Konferenz in Ekaterinburg zu besuchen, die mich denke ich der Wissenschaft sehr viel näher gebracht hat, wenn auch nicht unbedingt dem Land Russland. Das Ende der Masterarbeit war dann ungewöhnlich stressig, da ich das Proceeding fertig schreiben musste und mich für ein Stipendium beworben habe, wofür ich dir denke ich ebenfalls dankbar sein sollte. Im Nachhinein war das Stipendium eine gute Sache, obschon es auf dem Weg meist mit mehr Arbeit und weniger Bezahlung verbunden war.

Vor allem möchte ich mich bei dir für die Jahre der Betreuung bedanken, während denen du immer ein offenes Ohr für mich hattest, auch wenn du eigentlich mit ganz anderen Dingen beschäftigt warst, wie zum Beispiel Kinder kriegen. Ich habe mich zu keinem Zeitpunkt schlecht betreut gefühlt, sondern habe im Gegenteil die Freiheit genossen meine Forschung in eigene Bahnen zu lenken. Auch über nicht die Arbeit betreffende Dinge konnte man sich immer gut unterhalten, was ebenfalls ein nicht zu unterschätzender Aspekt der Betreuung ist. Ich bedanke mich von ganzem Herzen!

Als zweites ist es sicherlich angebracht der zweiten Person zu danken, die diese Arbeit in ihrer Vollständigkeit liest (mich ausgeschlossen). Vielen Dank Dr. Mascotto, dass sie sich die Zeit nehmen meine Arbeit zu begutachten. Wir hatten während meiner Zeit an der Uni nicht allzu viele Überschneidungspunkte, weshalb ich nicht allzu viel berichten habe, aber ich möchte mich trotzdem herzlich für die Arbeit bedanken!

Als nächstes möchte ich dem Leiter des Arbeitskreises, meinem Chef Prof. Dr. Volker Abetz danken. Vielen Dank Volker, dafür dass du immer für einen guten Witz zu haben bist und dafür dass du unser Schiff mehr oder weniger unbeschadet durch die Untiefen der Akademie gesteuert hast. Du warst immer da wenn mal ein Machtwort gesprochen werden musste und schnell zur Stelle wenn

es dringend wurde. Auch für deine wissenschaftliche und persönliche Integrität möchte ich an dieser Stelle bedanken, ich werde nie vergessen wie schnell du bereit warst mein mageres Stipendiatengehalt aufzustocken um mich fair gegenüber den Kollegen zu behandeln. Deinen Einsatz für die Bedrohten und Verfolgten dieser Welt finde ich immer wieder beeindruckend, bleib genau so wie du bist! Vielleicht ein bisschen weniger Arbeit, dann bleibst du uns noch länger Erhalten.

An dieser Stelle möchte ich mich bei Prof. Dr. Carmen Herrman und Prof. Dr. Horst Weller bedanken. Ich hoffe wenn sie an dieser Stelle meiner Dissertation angekommen sind haben sie einen ersten Eindruck meiner Dissertation gewinnen können und wir werden eine entspannte Disputation zusammen haben. Vielen Dank für ihre Zeit.

Einen großen Anteil an meiner Dissertation trägt auch mein Kollege und Freund der Niklas. Vielen dank für all die Reisen in die entlegensten Ecken Deutschlands die du gemeinsam mit mir durchgestanden hast. Wir ham uns zwar schon auch die schlimmsten Dreckslöcher zum Übernachten ausgesucht, aber ein paar Perlen waren auch dabei. Es war immer angenehm mit dir zu Reisen und weitab des Fachlichen zu diskutieren. Auch während der vielen, vielen, vielen Mensabesuche war deine Meinung zum täglichen Essen stets gefragt und deine Diskussionen mit Tilman werden mir stets mit schmerzen in Erinnerung bleiben. Du warst die letzte Person von der ich erwartet hätte, dass sie an der Uni bleibt aber Überraschungen gibt's immer. Ich wünsche dir super viel Spaß mit all deinen neuen Untergebenen und dass du deinen westlichen Werten treu bleibst!

Immer für eine fachliche Frage oder auch jede Partie Dart zu haben war Felix. Ich danke dir für dein umfangreiches Wissen in allen Lebenslagen, von der Küche bis zu Lebensweisheiten. Ich danke dir dafür, dass du meine Dartskills immer ins rechte Licht gerückt hast, durch Demütigung. Ich danke dir für die Jahre als bester Bürokollege und werde dich auf jeden Fall vermissen wo auch immer es mich hin verschlägt. Ich wage es nicht mir vorzustellen wer nach dir der nächste Goldjunge wird, aber da muss jemand in große Fußstapfen treten. Ganz viel Spaß in Geesthacht, pass auf dass du dich da nich festsetzt und Volkers Nachfolge antrittst.

Ich komme zur besten Bürokollegin: Iklima. Ich muss mich sehr Lieb bedanken für die schöne Zeit die wir zusammen hatten. Die Zeit die wir damit verbracht haben die doppel Zwei zu finishen wird für immer als eine der besten Zeitverschwendungen meines Lebens in die Annalen eingehen. Mit freunden erinnere ich mich an die Zeit in der du deine Praktikanten durch pure Freundlichkeit dazu gebracht hast bis weit über die normale Arbeitszeit hinaus zu arbeiten. Ich weiß ganz genau dass wir nochmal irgendwann dazu kommen

werden wieder miteinander zu zocken und auch das nächste Spiel nach Sekiro easy zu bewältigen. Lass dich nicht vom grausamen Unialltag kleinkriegen und bewahre deine Liebe seit!

Auch dem Herrn Tilman möchte ich danken, dafür dass er noch so oft in WC3 auf die Fresse kriegen kann und das Spiel trotzdem feiert. Auch danke ich dir für deine entrüsteten Ausbrüche ab und zu (Ihr könnt nich erzählen, dass ihr noch nie im ... wart!). Ich hoffe du wirst klarkommen wenn keine Senioren mehr da sind und wünsche dir alleits hohe Motivation bei der Arbeit.

Maggie möchte ich natürlich danken, zum einen fürs Messen von vielen XRD-Proben, aber auch für dein sonniges Gemüt. Natürlich auch für die vielen Kuchen und anderen Leckereien, die du immer wieder mitgebracht hast, die haben mir immer den Tag versüßt.

Philipp möchte ich dafür danken, dass er mich quasi zurück aufs Board gebracht hat und mir quasi so den Einstieg ins Kite-geschäft erleichterte. Du bist wahrscheinlich der nächste Kandidat für den Goldjungenplatz im AK Abetz, also viel Spaß weiterhin bei der Arbeit. Vielen Dank auch dafür dass du uns in der Corona-Zeit immer Mittags mit Essen versorgt hast, wenn wir mal wieder was von außerhalb des Dunstkreises der Uni brauchten. We will watch your career with great interest!

Vielen Dank auch an Sascha, zum einen für die Arbeit die du für mich als Praktikant geleistet hast aber auch für die kurze Zeit die ich dich im Arbeitskreis als Master und Doktorand erleben durfte. Du kannst einem zwar schon ganz gut das Ohr abkauen aber dennoch sind die Gespräche meist unterhaltsam. Ich hoffe wir schaffens nochmal auf deinen Campingplatz.

Jingcong, du bist wahrscheinlich der netteste und beste Chinese den ich je getroffen habe, und ich war immerhin für 2 Wochen mal in China. Dir möchte ich dafür danken, dass du unseren Arbeitskreis kulturell bereicherst und für den Tee den du zu unserer Sammlung beigesteuert hast. Ich hoffe du findest auch mal zum entspannteren Teil des Doktorandenlebens.

Merlina möchte ich für ihr Organisationstalent danken, ohne dass wir bei vielen Feiern sicherlich schlechter da gestanden hätten. Vielen Dank für deine Bodenständige Art und lass dich von der Uni nicht verrückt machen!

Auch unsere ehemaligen Mitstreiter werde ich nie vergessen. Vielen dank Elisabeth als Stimme der Moral und der Berliner Luft! Du hast unser Mensateam immer sehr bereichert, auch als einzige Frau warst du nie ein zügelnder Einfluss auf den Hahnenkorb. Auch vielen Dank dafür dass du die treibende Kraft hinter den Anstrengungen bist die Truppe auch nach der Uni nicht zu weit auseinander Driften zu lassen.



Steffen dem ersten Goldjungen möchte ich vor allem für seinen trockenen Humor danken. Mit deiner Detailtreue hast du den Grundstein für solides wissenschaftliches Arbeiten im Arbeitskreis gelegt, von dieser Einstellung profitieren wir auch heute noch alle. Bleib auch als großverdienender FDP-Wähler immer aufm Teppich und hör auf deine Freundin.

Auch Elaine möchte ich für die schöne Zeit danken, vor allem für die wilde Feierei. Sehr Schade dass du es nicht ganz über die Zielgerade geschafft hast, aber vielleicht wird das eines Tages ja doch noch.

Alex möchte ich für die nette Aufnahme in den Arbeitskreis danken, als du das erste Mal gefragt hast wann ich denn nach meiner Bachelorarbeit mal wieder im Ak auftauche, da wusste ich schon fast wo meine Zukunft liegen würde.

Maryam möchte ich für die nette Betreuung meiner Bachelorarbeit und für die Gewöhnung an anständige Arbeitszeiten (ab 8) danken. Ich bin gespannt ob du für deinen Postdoc auch irgendwann mal den Doc part nachholen wirst.

Den lieben Studenten die bei mir ein Praktikum absolvierten möchte ich natürlich auch danken, vor allem für das Vertrauen in meine Lehrfähigkeiten. Vielen Dank nochmal an Sascha, an Cristina, viele Grüße an die Family, an Gustav, meinen ersten, an Eike, an Christopher und an Hanna.

Hierbei nimmt Larissa eine spezielle Rolle ein, da sie eine Bachelorarbeit bei mir absolvierte und uns danach als Hiwi erhalten bleibt. Vielen Dank für die wertvolle Laborarbeit und für die Zeit die du bei uns verbringst. Ich denke dass dich ein ähnliches Schicksal wie viele Praktikanten im Ak Abetz erwarten wird: Du bleibst für deine gesamte Unizeit bei uns!

Von den Festangestellten möchte ich vor allem Andreas danken für die viele Hilfe bei meinen SAXS Messungen. Vielen Dank auch dafür dass du mich weiterhin bei SAXS betreffenden Sachen im Auge hast, sei es jetzt beim Primer oder auch die Stelle in Hannover.

Martin danke ich für den handwerklichen Einsatz für den Arbeitskreis und für die schnelle Hilfe bei kleinen Alltagsproblemen. Vielen Dank auch für die Entsorgung!

Vielen Dank auch an Andreas Kornowski für die Gespräche übers TEM. Ich habe sehr viel gelernt und bin ziemlich sicher, dass ich ohne deine Hilfe keine ordentliche Diffraktion gemessen hätte.

Almut Bark möchte ich für die vielen XRD-Messungen danken und für das Verständnis wenn ich die Probe dann doch mal wieder versaut oder vergessen hatte.

Zu guter letzt möchte ich noch meiner Familie und meinen Freunden danken. Meiner Mutter Meta und meinem Vater Tjard für die konstante Unterstützung

und dafür dass ihr mich auf diesen Weg geführt und ihn mir ermöglicht habt. Mein Bruder Simon hatte jetzt vielleicht nicht direkt einen Anteil aber ich möchte ihm trotzdem dafür danken dass er da ist.

Alina, du bist das Beste was mir je passiert ist und ich möchte mich ganz doll für deine Unterstützung und Liebe bedanken.

Vielen Dank!

## Declaration of Academic Integrity

Hereby I confirm that I wrote the present work independently and that it has not been submitted in any form for another degree at any university or other institute. Information derived from the published and unpublished work of others has been acknowledged in the text and a list of references is given in the bibliography.

-----  
-----

Place, Date, Signature

## Eidesstattliche Erklärung

Hiermit versichere ich an Eides statt, die vorliegende Dissertation selbst verfasst und keine anderen als die angegebenen Hilfsmittel benutzt zu haben. Die eingereichte schriftliche Fassung entspricht der auf dem elektronischen Speichermedium. Ich versichere, dass diese Dissertation nicht in einem früheren Promotionsverfahren eingereicht wurde.

Datum, Unterschrift